AFRL-VS-HA-TR-2006-1110

# The Development of a Stratospheric Real-Time Turbulence Modeling System


Yuh-Lang Lin
Michael L. Kaplan
Chad J. Ringley
David R. Vollmer
Paul S. Suffern
Zachary G. Brown
Michael T. Kiefer

North Carolina State University
Dept. of Marine, Earth & Atmospheric Sciences
Campus Box 8208
Raleigh, NC 27695


Scientific Report No. 2

7 July 2006

APPROVED FOR PUBLIC RELEASE; DISTRIBUTION UNLIMITED.


AIR FORCE RESEARCH LABORATORY
Space Vehicles Directorate
29 Randolph Road
AIR FORCE MATERIEL COMMAND
Hanscom AFB, MA 01731-3010

## NOTICES

Using Government drawings, specifications, or other data included in this document for any purpose other than Government procurement does not in any way obligate the U.S. Government. The fact that the Government formulated or supplied the drawings, specifications, or other data does not license the holder or any other person or corporation; or convey any rights or permission to manufacture, use, or sell any patented invention that may relate to them.

Qualified requestors may obtain copies of this report from the Defense Technical Information Center (DTIC) (http://www.dtic.mil). Other requests for this document shall be referred to AFRL/VSBYM, 29 Randolph Road, Hanscom AFB, MA 01731-3010.

AFRL-VS-HA-TR-2006-1110 HAS BEEN REVIEWED AND IS APPROVED FOR PUBLICATION IN ACCORDANCE WITH ASSIGNED DISTRIBUTION STATEMENT.

| //signed// | //signed// |
|---|---|
| DOUGLAS C. HAHN<br>Contract Manager | ROBERT BELAND, Chief<br>Battlespace Surveillance Innovation Center |

This report is published in the interest of scientific and technical information exchange, and its publication does not constitute the Government's approval or disapproval of its ideas or findings.

# REPORT DOCUMENTATION PAGE

*Form Approved*
*OMB No. 0704-0188*

Public reporting burden for this collection of information is estimated to average 1 hour per response, including the time for reviewing instructions, searching existing data sources, gathering and maintaining the data needed, and completing and reviewing this collection of information. Send comments regarding this burden estimate or any other aspect of this collection of information, including suggestions for reducing this burden to Department of Defense, Washington Headquarters Services, Directorate for Information Operations and Reports (0704-0188), 1215 Jefferson Davis Highway, Suite 1204, Arlington, VA 22202-4302. Respondents should be aware that notwithstanding any other provision of law, no person shall be subject to any penalty for failing to comply with a collection of information if it does not display a currently valid OMB control number. **PLEASE DO NOT RETURN YOUR FORM TO THE ABOVE ADDRESS.**

**1. REPORT DATE** *(DD-MM-YYYY)*
07-07-2006

**2. REPORT TYPE**
Scientific Report No. 2

**3. DATES COVERED** *(From - To)*
06-07-2005 - 06-06-2006

**4. TITLE AND SUBTITLE**
The Development of a Stratospheric Real-Time Turbulence Modeling System

**5a. CONTRACT NUMBER**
FA8718-04-C-0011

**5b. GRANT NUMBER**
N/A

**5c. PROGRAM ELEMENT NUMBER**
62601F

**6. AUTHOR(S)**
Yuh-Lang Lin, Michael L. Kaplan, Chad J. Ringley, David R. Vollmer, Paul S. Suffern, Zachary G. Brown and Michael T. Kiefer

**5d. PROJECT NUMBER**
1010

**5e. TASK NUMBER**
OT

**5f. WORK UNIT NUMBER**
A1

**7. PERFORMING ORGANIZATION NAME(S) AND ADDRESS(ES)**

Dept of Marine, Earth & Atmospheric Sciences
Campus Box 8208
North Carolina State University
Raleigh, North Carolina 27695

**8. PERFORMING ORGANIZATION REPORT NUMBER**

**9. SPONSORING / MONITORING AGENCY NAME(S) AND ADDRESS(ES)**
Air Force Research Laboratory
29 Randolph Road
Hanscom AFB MA 01731-3010

**10. SPONSOR/MONITOR'S ACRONYM(S)**
AFRL/VSBYA

**11. SPONSOR/MONITOR'S REPORT NUMBER(S)**
AFRL-VS-HATR-2006-1110

**12. DISTRIBUTION / AVAILABILITY STATEMENT**

Approved for public release; distribution unlimited.

**13. SUPPLEMENTARY NOTES**

**14. ABSTRACT**

The research project focused on the development of an automated numerical prediction system for stratospheric turbulence. This involved modifying and testing a stratospheric mesoscale numerical model with observed initial data from several case studies. A sequence of events was simulated that likely organized environments favorable for stratospheric turbulence. This sequence involved the development of large amplitude hydrostatic gravity waves that in turn modified the lower stratospheric environment making it favorable for wave breaking and significant eddy dissipation. An automatic grid nesting location system was tested that exploited three different dynamical indices, which would be indicators of the potential for stratospheric turbulence, i.e., the NCSU1 index, vertical variation of the Scorer parameter as well as the eddy dissipation rate derived from the complete turbulence kinetic energy equation. The automatic grid nesting scheme was utilized for several case studies wherein large amplitude gravity waves were simulated.

**15. SUBJECT TERMS**
Turbulence prediction system, Gravity-wave breaking, Dynamic indices

| 16. SECURITY CLASSIFICATION OF: | | | 17. LIMITATION OF ABSTRACT | 18. NUMBER OF PAGES | 19a. NAME OF RESPONSIBLE PERSON |
|---|---|---|---|---|---|
| a. REPORT | b. ABSTRACT | c. THIS PAGE | | | Douglas C. Hahn |
| UNCLASSIFIED | UNCLASSIFIED | UNCLASSIFIED | SAR | 88 | 19b. TELEPHONE NUMBER *(include area code)* 781-377-2878 |

## CONTENTS


| | |
|---|---|
| 1. Summary | 1 |
| 2. Introduction | 1 |
| 3. Methods, Assumptions and Procedures | 2 |
| 4. Results and Discussions | 4 |
| 5. Conclusions | 25 |
| 6. Recommendations | 26 |
| References | 27 |
| Appendix A | 29 |
| Appendix B | 35 |
| Appendix C | 49 |
| Appendix D | 67 |

## FIGURES

1. Synoptic scale wind vector analysis at (a) 200 hPa and (b) 100 hPa valid at 1200 UTC 9 December 1992 6

2. 18-km NHMASS simulated 200-hPa winds ($ms^{-1}$), heights (dam) and velocity divergence ($s^{-1}$ x $10^{-5}$) valid at a) 0600 UTC, b) 1000 UTC, and c) 1500 UTC 9 December 1992 7

3. 18-km NHMASS simulated 50-hPa winds ($ms^{-1}$), heights (dam) and velocity divergence ($s^{-1}$ x $10^{-5}$) valid at a) 0600 UTC, b) 1000 UTC and c) 1200 UTC 9 December 1992. 9

4. 18-km NHMASS simulated vertical cross sections of potential temperature (K) and velocity divergence ($s^{-1}$ x $10^{-5}$) valid at a) 0600 UTC and b) 1000 UTC 9 December 1992. 12

5. 18-km NHMASS simulated 50-hPa NCSU 1 and 2 indices valid at 0600 UTC 9 December 1992 13

6. 6-km NHMASS simulated a) 200-hPa winds (m/s), heights (dam) and velocity divergence ($s^{-1}$ x $10^{-5}$) and b) vertical cross section of potential temperature (K) and velocity divergence ($s^{-1}$ x $10^{-5}$) valid at 1000 UTC 9 December 1992. 14

7. a) Observed sounding at Denver, Colorado, valid at 1200 UTC 9 December 1992. Observed potential temperature (K) at b) 200 hPa, c) 150 hPa and d) 100 hPa valid at 1200 UTC 9 December 1992. 15

8. 6-km NHMASS simulated a) 50-hPa winds ($ms^{-1}$), heights (dam) and velocity divergence ($s^{-1}$ x $10^{-5}$) and b) 50-hPa NCSU 1 and 2 indices valid at 1000 UTC 9 December 1992. 17

9. 2-km NHMASS simulated vertical cross section of potential temperature (K) and velocity divergence ($s^{-1}$ x $10^{-5}$) valid at 1430 UTC 9 December 2002. 18

10. 2-km NHMASS simulated vertical cross section of potential temperature (K) and wind velocity ($ms^{-1}$) valid at 1430 UTC 9 December 2002. 18

11. 2-km NHMASS simulated 200-hPa winds ($ms^{-1}$), heights (dam) and velocity divergence ($s^{-1}$ x $10^{-5}$) valid at 1430 UTC 9 December 2002. 19

12. 2-km NHMASS simulated vertical cross section of potential temperature (K) and circulation vectors ($ms^{-1}$)valid at 1430 UTC 9 December 1992. 20

13. NHMASS simulated Scorer parameter gradient in the vertical centered at 200-hPa and 200-hPa Scorer parameter ($m^2$) valid for the a) 2-km simulation valid at 1430 UTC

and b) 667-m simulation valid at 1509 UTC 9 December 1992. Star marks location of the aircraft accident. 21

14. 222-m NHMASS simulated vertical cross section of Brunt-Väisälä frequency squared ($s^{-2}$), Richardson number, circulation vectors and potential temperature valid at 1507 UTC 9 December 1992. 22

15. 222-m NHMASS simulated explicit flux of turbulence kinetic energy ($m^3s^{-3}$ at and valid at a) 11250 m and 1500 UTC, b) 11,500 m and 1507 UTC and c) 11,750 m and 1507 UTC 9 December 1992. 23

16. 222-m NHMASS simulated vertical cross section of X-space vorticity ($s^{-1}$ x $10^{-4}$) valid at 1507 UTC 9 December 1992. 24

17. 71-m NHMASS simulated 275 hPa vertical motion ($cms^{-1}$) valid at 1507 UTC 9 December 1992. 25

## 1. SUMMARY

A mesoscale numerical modeling system is adapted for use into the lower stratosphere. The model and an automated grid nesting scheme continued to be tested with observed initial data. The purpose of the model and the new nesting scheme is to improve the prediction of regions in which possible severe aviation turbulence occurs within the lower stratosphere. Simulation results show a strong link in the process of stratospheric turbulence to terrain-induced large amplitude gravity waves that eventually affect the lower stratosphere. The automated grid nesting scheme employs dynamical parameters that are consistent with a 3-stage multi-scale process resulting in turbulence generation. The grid nesting scheme continued to be tested to determine its potential utility.

## 2. INTRODUCTION

The operational forecasting of tropospheric turbulence has been ongoing for several years. Many indices are generated daily from operational numerical weather prediction models. The National Weather Service (NWS) has employed the Ellrod Index (Ellrod and Knapp 1992), the NOAA Forecasting Systems Laboratory has employed indices developed by Marroquin (1998) based on turbulence kinetic energy and eddy dissipation rate, and the Research Applications Program of the National Center for Atmospheric Research employs the Graphical Turbulence Guidance index as part of the suite of products from the NWS RUC II model (Sharman et al. 2006). These systems are designed for use in the troposphere and they are not strongly coupled to the model, i.e., indices are simply calculated from model-generated dependent variables and any grid nesting algorithms are independent of the case study and ongoing simulated fields, which the models produce.

The processes that create turbulence in the stratosphere are likely coupled to the troposphere as energy regularly is exchanged by vertically propagating internal gravity waves between the two atmospheric regions. This vertical coupling is greatly facilitated during moist convection or the development of large amplitude mountain waves as these local circulations are capable of modifying their immediate environment thus resulting in 3-dimensional fluxes of kinetic energy. The magnitude of the vertical flux of kinetic energy is, therefore, a function of the kinematic and thermodynamic fields that evolve in response to terrain-induced or moist convective motions, i.e., the perturbed static stability and vertical wind shear environments surrounding dry or moist convection. These features generate buoyancy and the mechanical dissipation of turbulence kinetic energy as evaluated from the turbulence kinetic energy equation, e.g., Stull (1988). Simulating stratospheric turbulence is an extraordinarily demanding problem because of this vertical coupling problem as well as the fine scale and transient nature of turbulence itself. Therefore, developing an automated system for the operational prediction of lower stratospheric turbulence potential will require at least three fundamental advances in mesoscale numerical weather prediction: 1) a model with significant vertical resolution spanning the mid-upper troposphere and lower stratosphere in order to resolve the vertical coupling, 2) a model with a "smart" grid nesting scheme that can focus on the regions of high turbulence potential based on scale-dependent dynamical indices that can

adapt to the favorable turbulence forcing processes that vary in space and time from one case study to another, and 3) a model which exploits as much of the observed data as possible in its initial conditions and lateral boundary conditions to improve the accuracy of its simulation. We continued to modify a numerical modeling system to improve the automated prediction of lower stratospheric regions of turbulence potential in which we incorporate all three of these improvements. During year 2, the focus was on testing the autonesting scheme with three additional case studies, two of which were recommended by the Air Force Research Laboratory (AFRL) contract monitor, i.e., a well-studied extreme turbulence case study over Colorado on 9 December 1992 (Clark et al. 2000), a case study over France on 23-24 November 2004, and one over Hawaii on 12-13 December 2002. All three had corroborative asynoptic observations of extreme terrain-induced turbulence. All three of the case studies represented large amplitude terrain-induced gravity wave case studies. At least three key stages of a multi-scale turbulence generation process are defined in the research.

## 3. METHODS, ASSUMPTIONS AND PROCEDURES

The first research task involved the continued testing of the Non-Hydrostatic Mesoscale Atmospheric Simulation System (NHMASS) model version 6.4 (Table 1) (e.g., Kaplan et al. 2000) on the three new case studies by validating against large scale synoptic and asynoptic observations. Validation indicated reasonable model simulation of large scale stratospheric winds, temperatures as well as clouds and precipitation. This modeling system represents a stratospheric modeling system, i.e., STRATONHMASS employing an extended model lid to 10 mb, increased number of vertical levels to 90 and a modified preprocessor to ingest observational data in the lower stratosphere, i.e., up to ~10 mb or ~30 km. This resulted in an average vertical thickness of model layers of ~300 m with a non-uniform vertical focus of resolution within the lower stratosphere.

The second research task involved testing the three new case studies as well as the previously-simulated 4 case studies during year 1 with the continuously modified and updated autonesting code. The autonest code development was accompanied by the analyses of model-generated dynamical processes that resulted in the focusing of high frequency wave energy in the lower stratosphere. The coarse mesh 18-km numerical simulations were one-way nested to 6-km, 2-km, 667-m, 222-m and 71-m horizontal resolution. The improved autonest code employed the NCSU1 index (e.g., Kaplan et al. 2004, 2006) when nesting from 18 to 6 km, 6 to 2 km and 2 km to 667 m.. This was coded to nest in a region and time based on the 50-mb NCSU1 threshold values. A great deal of effort was expended to develop thresholds for this index based on the results of all seven research case studies. The autonest code was being employed to nest based on the NCSU1 index at all grid resolution simulations ≥2 km and then employed the Scorer Parameter variation in the vertical below 2-km horizontal resolution and subsequently was nested based on threshold values of eddy dissipation rate from the complete turbulence kinetic energy equation at grid resolutions below 222 m. These equations are listed below.

Table 1. STRATONHMASS (Version 6.4)

| **Initialization** |
|---|
| • 3-D multivariate OI procedure used to blend a first guess fields (e.g. previous MASS simulation, NCEP model output, archived Reanalysis data) with observations from a variety of sensing systems (e.g., surface, rawinsonde)<br>• Global databases of terrain height, land cover/land use, vegetation index, sea surface temperature, soil texture, snow cover, soil moisture, subsurface temperature, and sea ice |
| **Numerical Techniques** |
| • Option of hydrostatic or non-hydrostatic primitive equations in terrain-following ($\sigma_p$) vertical coordinate with $4^{th}$-order accurate finite differencing<br>• MPDATA positive definite advection scheme<br>• Option of one-way or two-way interactive nesting, with arbitrary coarse/fine grid spacing ratio and unrestricted number of nested domains for one-way nesting |
| **Boundary Layer/ Surface Physics** |
| • 1.5 order Turbulence Kinetic Energy (TKE) parameterization with surface layer based on similarity theory formulation<br>• Surface energy budget with option of isothermal or non-isothermal soil-vegetation canopy formulations and heterogeneous subgrid scale areas<br>• Surface hydrology includes budget equations for three moisture reservoirs (cover layer, shallow and deep soil layers) and snow cover which incorporates the effects of accumulation, settling, melting and sublimation |
| **Moisture Physics** |
| • Option of diagnostic or three prognostic schemes with varying levels of sophistication. Prognostic equations for cloud water, cloud ice, rain water, snow and hail using a bulk microphysics parameterization<br>• Option of Kuo-type cumulus parameterization with moist downdraft physics, Fritsch-Chappell scheme, Kain-Fritsch scheme or Grell scheme |
| **Radiation** |
| • Longwave and shortwave radiation parameterized in surface energy budget and in the free atmosphere. Interaction with atmospheric water vapor, liquid/frozen water, and parameterized sub-grid clouds |

$$\text{NCSU1 Index} = \left[\vec{U} \bullet \nabla \vec{U}\right] \frac{|\nabla \zeta|}{|Ri|} \tag{1}$$

$$\text{Scorer Parameter} = \frac{N^2}{U^2} - \frac{U_{zz}}{U} \tag{2}$$

$$\text{EDR} = \frac{-\bar{u}\frac{\partial \bar{e}}{\partial x} - \bar{v}\frac{\partial \bar{e}}{\partial y} - \bar{w}\frac{\partial \bar{e}}{\partial z} + \frac{g}{\bar{\theta}_v}\overline{(w'\theta_v')}}{-\overline{(u'w')}\frac{\partial \bar{u}}{\partial z} - \frac{\partial}{\partial z}\overline{(w'e)} - \frac{1}{\bar{\rho}}\frac{\partial}{\partial z}\overline{(w'p')} - \frac{\partial \bar{e}}{\partial t}} \tag{3}$$

Task 3 involved continued testing of the code that will be used to improve the initial asynoptic remotely-sensed data to be employed in the model's initial conditions. This will focus on relative humidity data derived from infrared cloud top temperatures. Task 4 involved modifying a version of the turbulence kinetic energy equation for use in the autonesting scheme so that the most comprehensive representation of the eddy dissipation rate can be calculated. This involved adding the advective terms as well as testing the calculation of all terms with a more explicit representation of turbulence fluxes from the simulated dependent variables as opposed to that derived from the turbulence kinetic energy planetary boundary layer formulation employed in the model in an effort to make the equation complete as is described in Appendix A.

Task 5 involved diagnosing the dynamical/synoptic processes involved in organizing severe convective and terrain-induced turbulence. A 3-stage paradigm was developed based the on research involving the 3 new case studies simulated this year. Finally, task 6 involved several required Air Force Research Laboratory reports, 4 conference preprints and 2 journal articles, which were prepared or were in the process of being prepared by the end of year 2 in an effort to document the research.

## 4. Results and Discussions

As noted in Appendices A and B, the paradigm developed to modify and implement successive generations of the autonest code is based on simulated dynamical adjustment processes in the lower stratosphere and upper troposphere . The 3 new terrain-induced turbulence case studies, i.e., 9 December 1992, 12-13 December 2002, and 23-24 November 2004, which were simulated this year, were used to test the autonest code. A paradigm was tested during the second year of the contract in which we compared our autonesting indices to dynamical processes that organized the generation of turbulence kinetic energy during the 9 December 1992 terrain-induced gravity wave event over Colorado (e.g., Clark et al. 2000), the 23-24 November 2004 terrain-induced turbulence case study over France and the 12-13 December 2002 terrain-induced turbulence case over Hawaii. These case studies highlight the processes that lead to terrain-induced turbulence. The autonest code was tested and compared to a multi-stage paradigm for the process leading to severe terrain-induced turbulence. ***Autonesting indices were tested so that they would become large in magnitude when a dynamical***

***sequence of events occurred resulting in simulated conditions favorable for terrain-induced turbulence consistent with this paradigm.***

We will discuss this paradigm employing the 9 December 1992 case study in which extreme terrain-induced turbulence damaged an aircraft crossing the Colorado Rocky Mountains just southwest of Denver and just below the tropopause, i.e., at ~39.6N and ~105.6W at ~1510 UTC 9 December 1992 (Clark et al. 2000). Since proof of extreme aviation turbulence existed near the tropopause, we are assuming that severe turbulence occurred within the stratosphere as well. The paradigm has 3 stages. ***Stage I involves the mountain wave genesis and its subsequent interaction with jet/front systems propagating over the Front Range of the Colorado Rocky Mountains. Stage II develops when a favorable environment for shearing instability is created by the stability and wind shear profiles accompanying the 3-dimensional mesoscale frontal circulations, which developed during stage I. Finally, stage III is the result of shear instability- induced flow-aligned gravity waves, flow-parallel rotors as well as downbursts and dissipation of turbulence kinetic energy as wave-induced convergence phases with unique density profiles in the vertical causing local regions of strong sinking motions and extreme eddy dissipation rates.***

During stage I, the NCSU1 index is most useful as a predictor of turbulence potential when employed at 18-km – 2-km horizontal resolutions in the lower-middle stratosphere. The index becomes strong when velocity convergence increases in proximity to strong gradients of relative vorticity as well as low Richardson number values. In order to establish large values of the index, one typically observes significant 3-dimensional mass and momentum adjustments to a local buoyancy perturbation. The more inhomogeneous the environment is surrounding a mass perturbation due to a local buoyancy source, the more likely that mass perturbation will be to modify the environment. Hence, jet shear zones accompanying frontal systems are ideal candidates for regions where the local buoyancy source can grow upscale and feedback to the larger scale circulations, i.e., the local and total time tendencies of velocity divergence and convergence grow upscale. The buoyancy perturbation in this case, as is typical of most terrain-induced waves, is the isentropic overturning and adiabatic compression on the lee side of the Colorado Rocky Mountain Front Range, which creates a large amplitude mountain wave that *subsequently interacts with the background jet streaks in the lower stratosphere.*

It is important to indicate prior to describing the stage I adjustments that in this case study there are 3 key jet/front systems that are affecting the Colorado Front Range at 1200 UTC 9 December, i.e., ~ 3 hours before the extreme aviation turbulence accident. One of these was a polar jet streak (Figures 1a and 2) propagating from the northwest to the southeast across the Front Range primarily between 200 and 300 hPa with its core centered over central Nevada. A second subtropical jet/front system could also be seen extending up towards the layer between 200 and 100 hPa from the west with its stratospheric core located over Utah (Figure 1b). Additionally, a weak stratospheric jet/wind max is located to the southwest of the accident location at 50 hPa (Figure 3). The accident location of ~39.6N and 105.6W was imbedded within the left exit region of the lowest polar jet/front system, the left exit region of the middle subtropical jet/front system and the exit region of the weak upper-level 50-hPa wind max. As can be seen in

a)

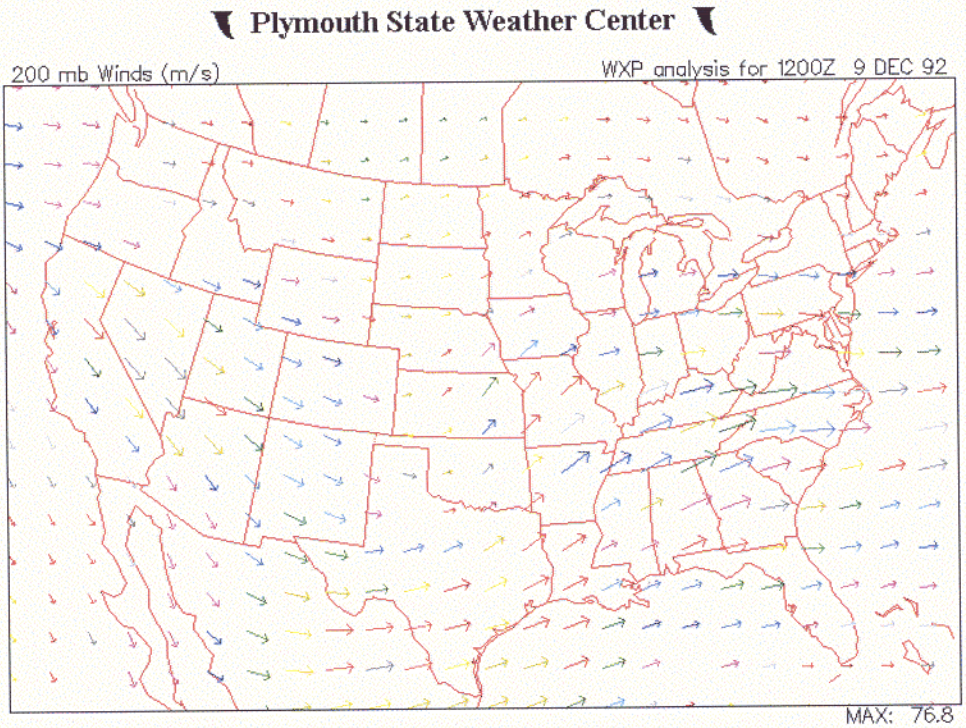


b)

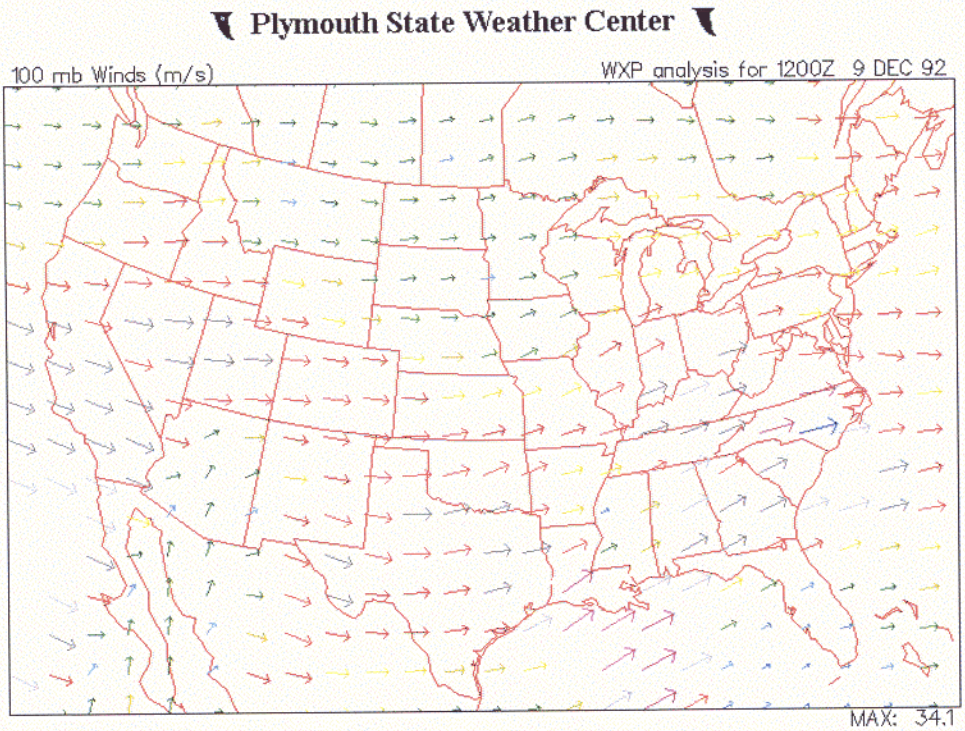


Figure 1. Synoptic scale wind vector analysis at (a) 200 hPa and (b) 100 hPa valid at 1200 UTC 9 December 1992.

a)

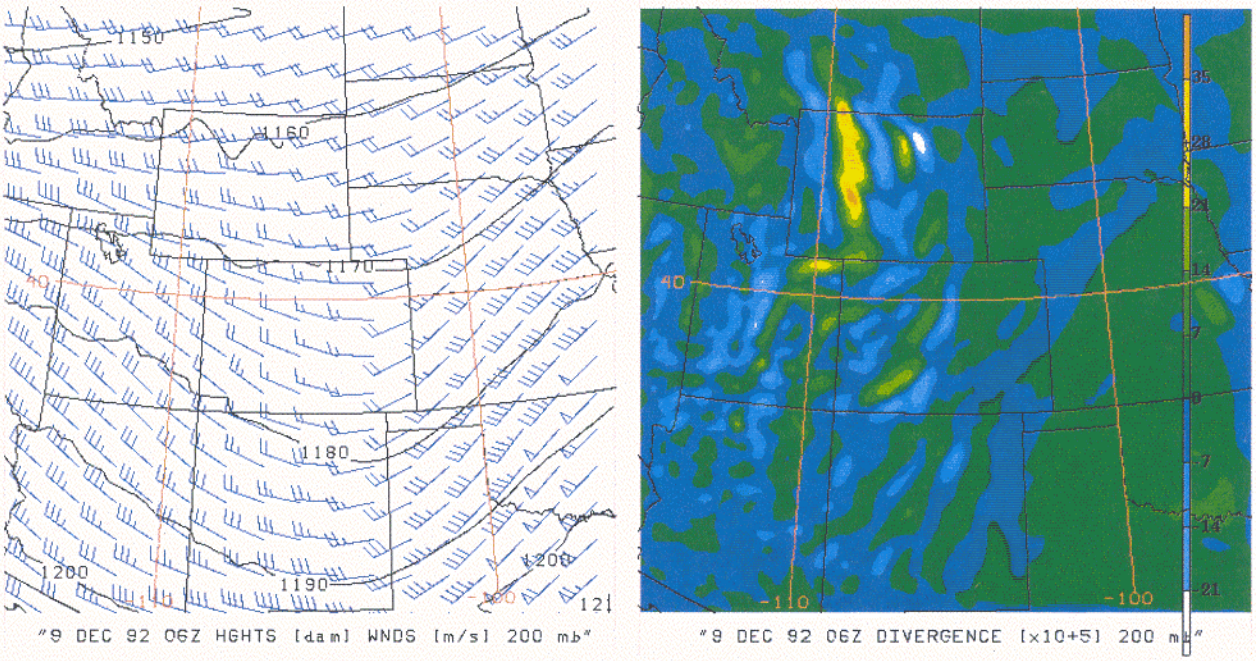


b)

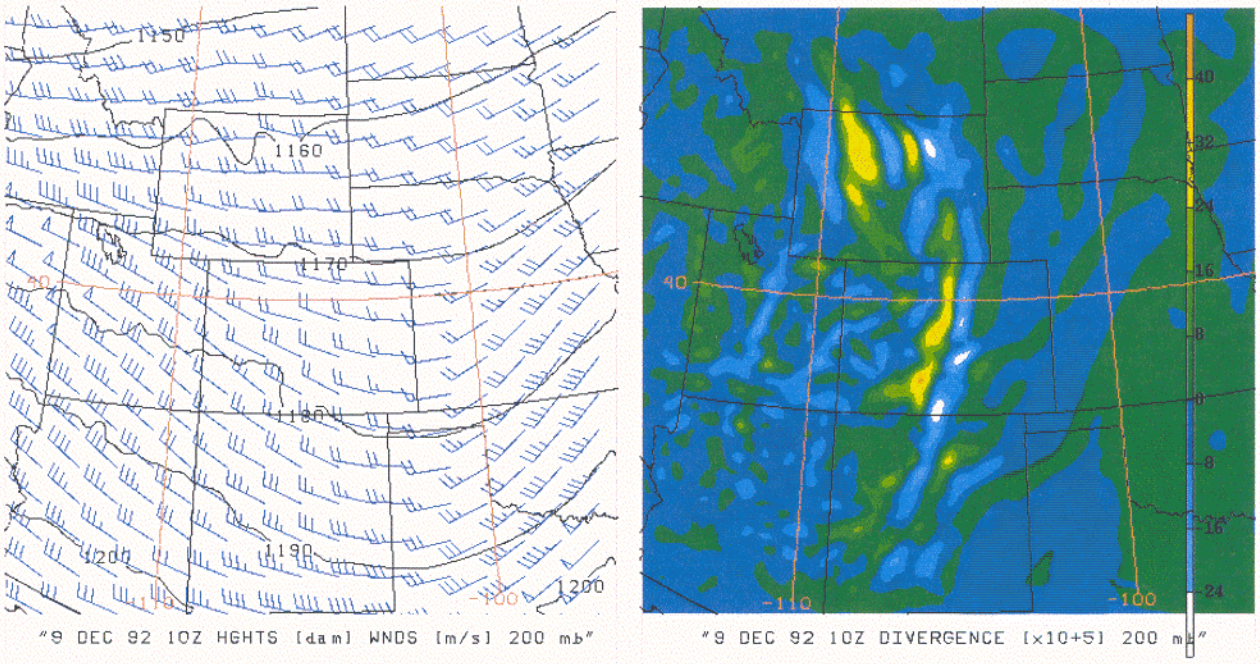


Figure. 2. 18-km NHMASS simulated 200-hPa winds ($ms^{-1}$), heights (dam) and velocity divergence ($s^{-1}$ x $10^{-5}$) valid at a) 0600 UTC and b) 1000 UTC.

(c)

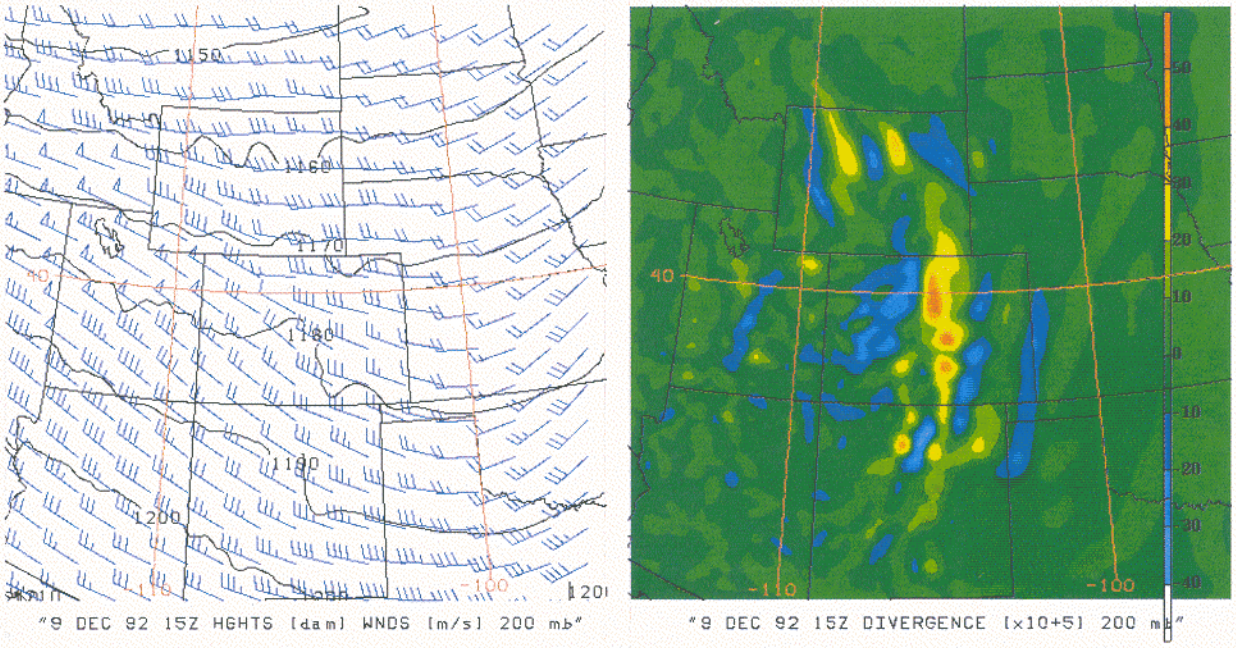


Figure 2 (cont.). 18-km NHMASS simulated 200-hPa winds ($ms^{-1}$), heights (dam) and velocity divergence ($s^{-1}$ x $10^{-5}$) valid at c) 1500 UTC 9 December 1992.

Figure 2, during stage I, as the diffluent left exit region of the polar jet stream at 200 hPa propagates over the Colorado Front Range early in the 18-km (coarse resolution) simulation, a developing deep thickness/thermal ridge acts to create a height perturbation coincident with mountain wave formation near 105W. This high pressure ridge aloft caused by the buoyancy perturbation, evident to the tropopause and well into the stratosphere, decelerates the flow west of the Front Range and accelerates the flow east of the Front Range as the ribbon of increasing upstream northwesterly winds propagates southeastwards. This process results in an intensifying velocity divergence pattern at this level operating on the polar jet's left exit region, i.e., the buoyancy perturbation acts to modify the jet causing velocity divergence to develop behind the accelerating flow east of the Front Range and within the decelerating flow just west of the Front Range. Thus the terrain-induced height and buoyancy perturbation acts to intensify the divergence within a region of the jet already favorable for velocity divergence generation, which by 1500 UTC exceeds 5 x $10^{-4}$ $s^{-1}$ directly over the accident location.

At a slightly earlier time, as can be seen in Figure 3, the 50-hPa fields indicate a more confluent flow in the right exit region of a weak wind maximum that results in the development of an opposite signed convergence maximum nearly directly over the 200-hPa divergence maximum. These mass adjustments result from the interaction of a sloping mountain wave pressure perturbation with differing background flows in the stratosphere. They are important because of their subsequent effect on the vertical wind shear and vertical variation of static stability resulting from the vertical variation of mass flux divergence between the lower stratosphere and the tropopause. They produce a growing negatively-tilted convergence zone between 50 and 100 hPa relative to a

growing negatively-tilted divergence zone between 150 and 250 hPa. Sinking motions aloft and rising motions near the tropopause, in response to the convergence/divergence profile in the vertical, result in the vertical convergence of the isentropic surfaces near the tropopause between 250 hPa and 150 hPa, i. e., the region between ~330 and 380 K as can be seen during the 0600 – 1000-UTC period in Figure 4. The vertically varying vertical circulations/motions are caused by the sloping mountain wave interaction with the various diverse wind maxima aloft. This causes a response in the mass flux divergence profile in the vertical resulting in the modification of the separation of the isentropes through convergence and divergence of potential temperature in the vertical. This strengthens the inversion near 200 hPa and weakens it below resulting in regions of reduced and increased static stability in the vertical.

The NCSU1 turbulence forecast index at 0600 UTC tends to become very large and exceeds the empirically-determined nesting maximum at this time very close to the location of the aircraft accident when it is forced by the stratospheric convergence of anticyclonic vertical vorticity by the 50-hPa west-southwesterly jet/front system. This convergence of anticyclonic vertical vorticity results in a descending circulation at and below 50 hPa. The descending circulation forces the isentropes to be compressed downwards towards the lower stratospheric and upper tropospheric ascending mountain wave circulations. The 18-km NCSU1 index can be seen depicted in Figure 5 within a region of values exceeding an empirically determined threshold from the southern Colorado Front Range northward to the accident location near 40N. This 0600-UTC incipient convergence of anticyclonic vorticity in the stratosphere represents the time of nesting to the 6-km scale of simulation.

a)

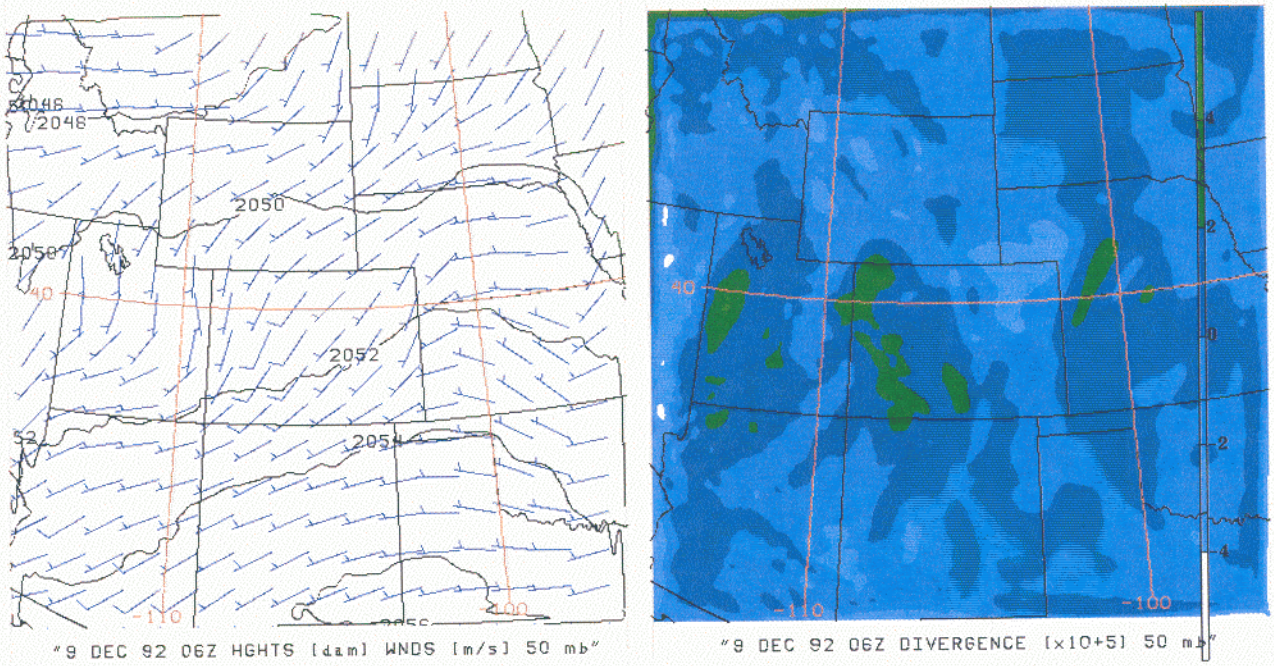


Figure 3. 18-km NHMASS simulated 50-hPa winds ($ms^{-1}$), heights (dam) and velocity divergence ($s^{-1}$ x $10^{-5}$) valid at a) 0600 UTC.

b)

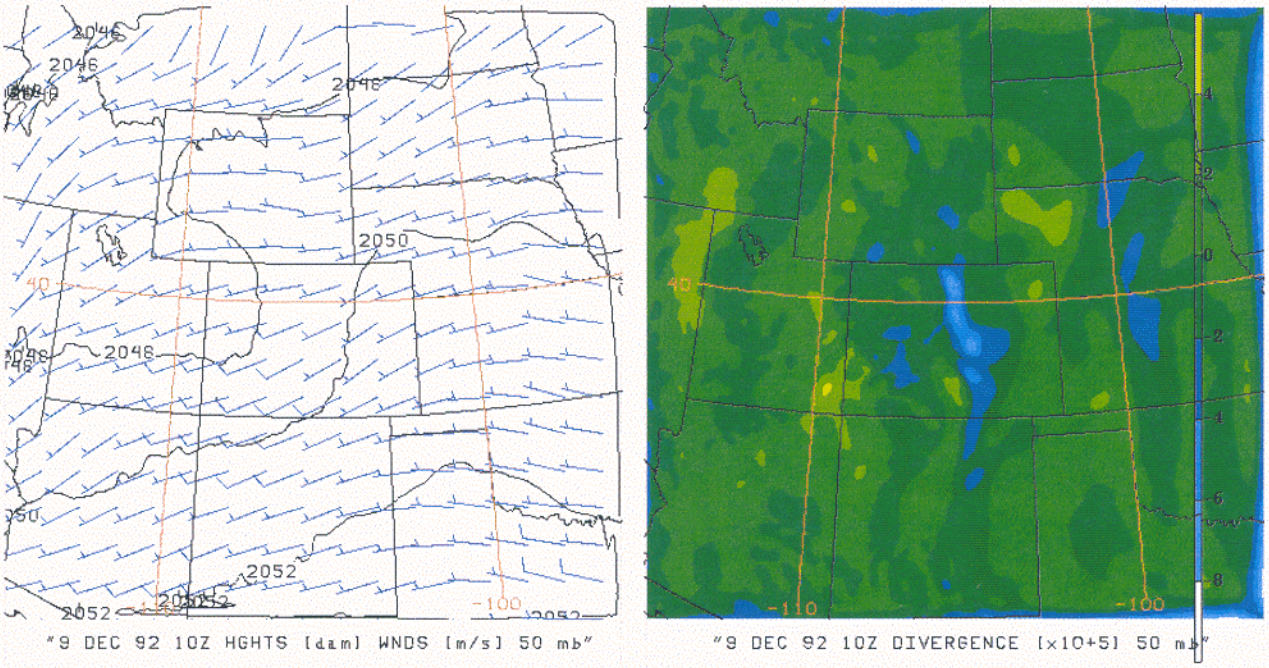


c)

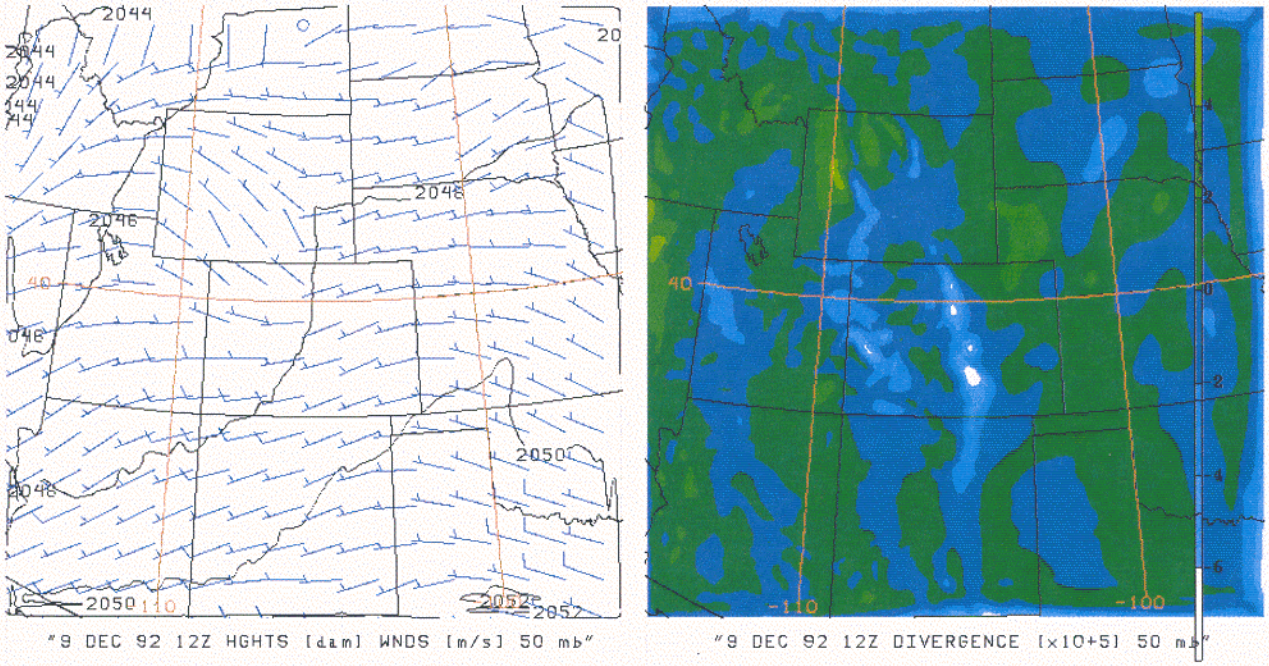


Figure 3 (cont.). 18-km NHMASS simulated 50-hPa winds ($ms^{-1}$), heights (dam) and velocity divergence ($s^{-1}$ x $10^{-5}$) valid at b) 1000 UTC and c) 1200 UTC 9 December 1992.

By 1000 UTC in Figure 6, one can see that in the 6-km simulation, the vertical variation of mass convergence has established an intense vertical front between ~330 and 380 K with the most vertically compressed isentropes near 200 hPa or ~338K. This level is becoming increasingly sandwiched in between the slowly rising maximum of horizontal velocity divergence at 200 hPa and sinking maximum of horizontal velocity convergence at and below 50 hPa, as can be seen from the 6 km simulated maxima in Figure 6. Figure 7 shows the observed rawinsonde at Denver, CO (DEN) at 1200 UTC, in which a very strong inversion has formed nearly exactly were the model vertical variation of divergence maximizes or just above 200 hPa, i.e., close to 40N and 338 K. This is also a region of transition from the polar jet exit region to the subtropical jet exit region between 200 and 150 hPa and is still within a region of strong convergence of anticyclonic vertical vorticity at 50 hPa. The temperature field oscillates from cold to warm to cold over a very shallow layer near 200 hPa in this sounding indicative of vertical frontogenesis consistent with Figure 6. The horizontal potential temperature analyses between 200 hPa and 100 hPa at 1200 UTC, also depicted in Figure 7, confirm the complex horizontal structure of the simulated vertically varying front from western to eastern Colorado. The static stability would reflect, consistent with Figures 9-12, differing slopes of the isentropes as one passes from west of the Front Range to east of the Front Range as cold and warm air pools vary in the vertical across Colorado, hence the likelihood of preferred regions of low Richardson number and differing vertical buoyancy profiles in the vertical. Figure 8 depicts the NCSU1 index maxima near 40N, which triggers the nest to 2 km at 1000 UTC.

Stage II becomes particularly evident in the 2-km simulations just before 1430 UTC. The progression of the 200-hPa polar jet closer to the accident location has strengthened and deepened the horizontal velocity divergence as well as the shearing and stretching deformations. These kinematical adjustments accompany the polar jet exit region as it is modified by the buoyancy perturbation of the adiabatic heating caused by flow over the mountains, in concert with the downward-building velocity convergence maximum below 100 hPa. This has intensified the vertical front resulting from the convergent (above) and divergent (below) forcing of the jet streams by the mass adjustment to the terrain-induced buoyancy perturbation. In response to the growing horizontal stretching and shearing deformation at 200 hPa associated with the flow-aligned accelerating and decelerating polar jet exit region, the horizontal velocity divergence becomes even stronger. This acts to enhance the extreme stable layer depicted in Figures 6 and 7 near 200 hPa and 338 K. This is the result of the reduced distance between the horizontal velocity divergence maximum and convergence maximum at ~250 and 125 hPa, respectively, thus causing a further strengthening of the inversion above 200 hPa by the convergence of potential temperature and the overturning of the 338-K isentrope at ~210 hPa near the horizontal location of the accident (Figure 8). The overturning is caused by the vertical variation of the vertical advection of potential temperature as well as the horizontal (flow-aligned) deformation of potential temperature near the accident location. This local 338-K isentropic overturning and flow-aligned perturbation occurs right where the vertical and horizontal flow-aligned fronts become juxtaposed on the immediate leeside of the Front Range close to the accident location. The vertical front caused by the vertical variation of vertical thermal advection and the horizontal front caused by the deformation of potential temperature are the product of the

a)

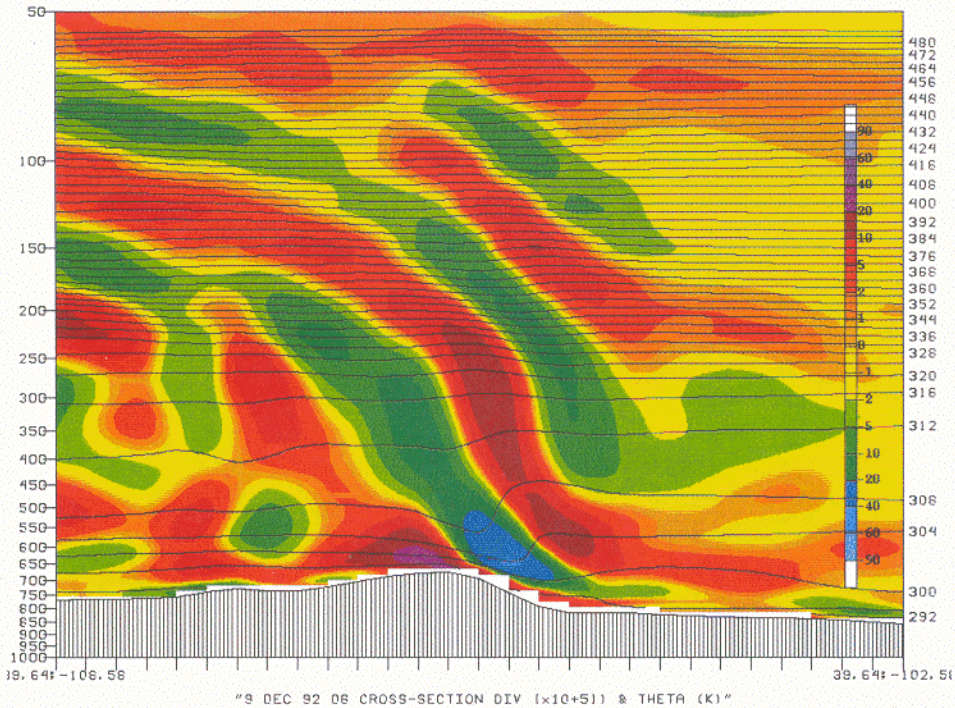


b)

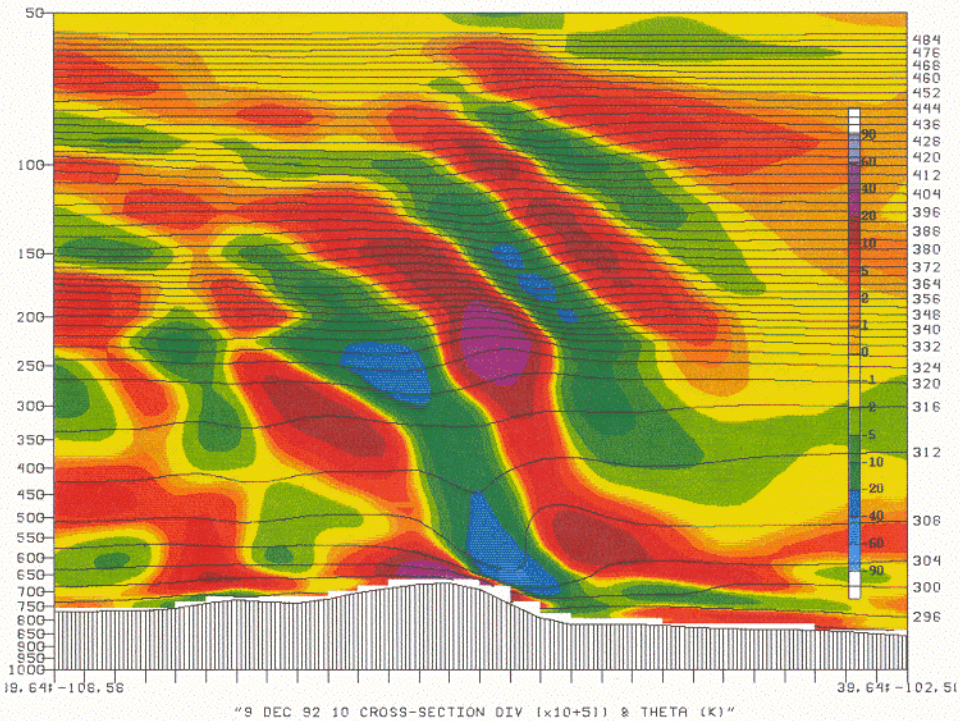


Figure 4. 18-km NHMASS simulated vertical cross sections of potential temperature (K) and velocity divergence ($s^{-1}$ x $10^{-5}$) valid at a) 0600 UTC and b) 1000 UTC 9 December 1992.

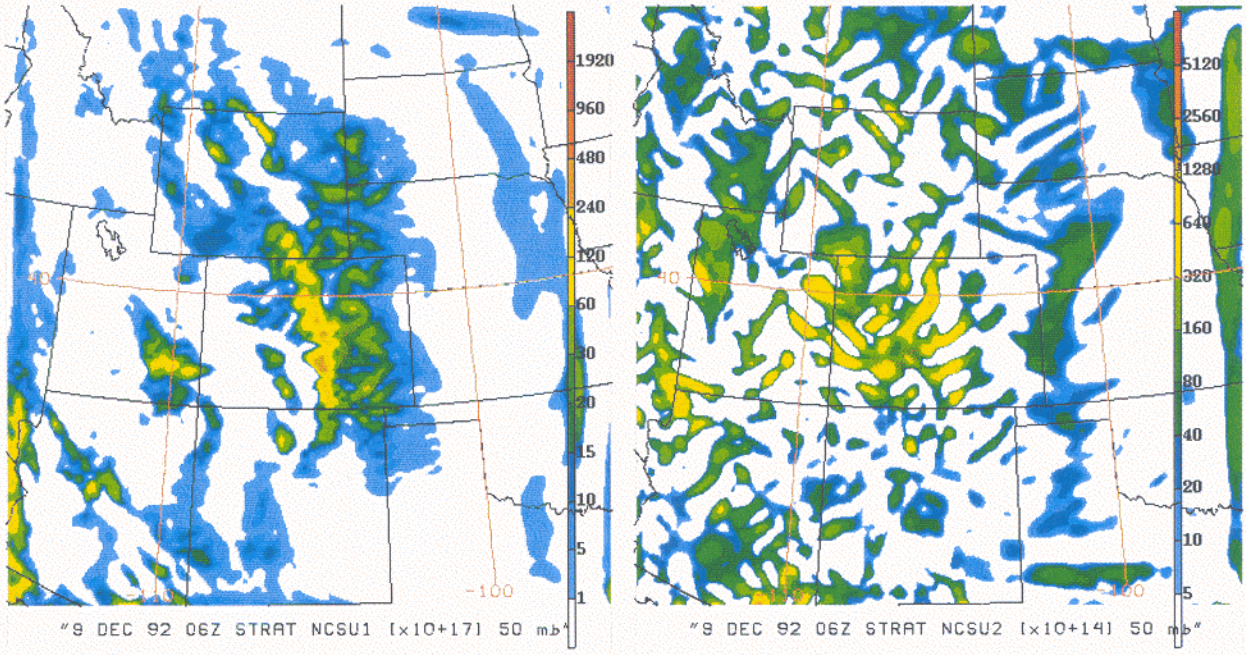


Figure 5. 18-km NHMASS simulated 50-hPa NCSU 1 and 2 indices valid at 0600 UTC 9 December 1992.

buoyancy forcing acting on the juxtaposed propagating polar jet exit/subtropical jet and weak stratospheric jet's exit regions. This focused isentropic perturbation causes the Richardson number to begin to drop in response to reduced static stability and increased vertical wind shear, and ultimately controls where the shear-induced flow-aligned gravity waves near banner-induced flow-parallel vortices strengthen and become juxtaposed in the finer scale simulations. This occurs in concert with the propagation of the polar jet exit region below 200 hPa over the accident location (Figure 9) and its subsequent deceleration and anticyclonic turning resulting in horizontal deformation (Figure 10). This increased turning yields deformation which accentuates the vertical and flow-aligned fronts. The subsequent reduction in static stability, Brunt-Väisälä frequency and Richardson number in the layer between 200 and 210 hPa is the result of the 3-dimensional frontogenesis over the leeside of the Front Range. It is accompanied by increased ascent below the divergence maximum in proximity to upstream descent and increased horizontal rotation along the x-axis parallel to the westerly flow extending down to nearly 300 hPa (Figure 11). The 3-dimensional perturbation of the 338 K isentropic surface caused by the 3-dimensional frontogenesis decreases the static stability in the layer between 200 and 210 hPa. A west-east vertical cross-section depicting this isentropic deformation and the associated circulation is shown in Figure 12.

This region of increasing velocity divergence and decreased static stability below 200 hPa and increased static stability above 200 hPa is consistent with the development of a nonuniform profile of Scorer parameter (equation 2) with respect to height. This thermal profile is totally consistent with the observed DEN sounding and potential temperature gradients in 3-dimensional space in Figure 7 in which cold air below 200 hPa is closely juxtaposed with relatively warm air at 200 hPa and then cold air above that near the Front Range. Hence, during stage II, the model nesting from 667 m to 222 m is

a)

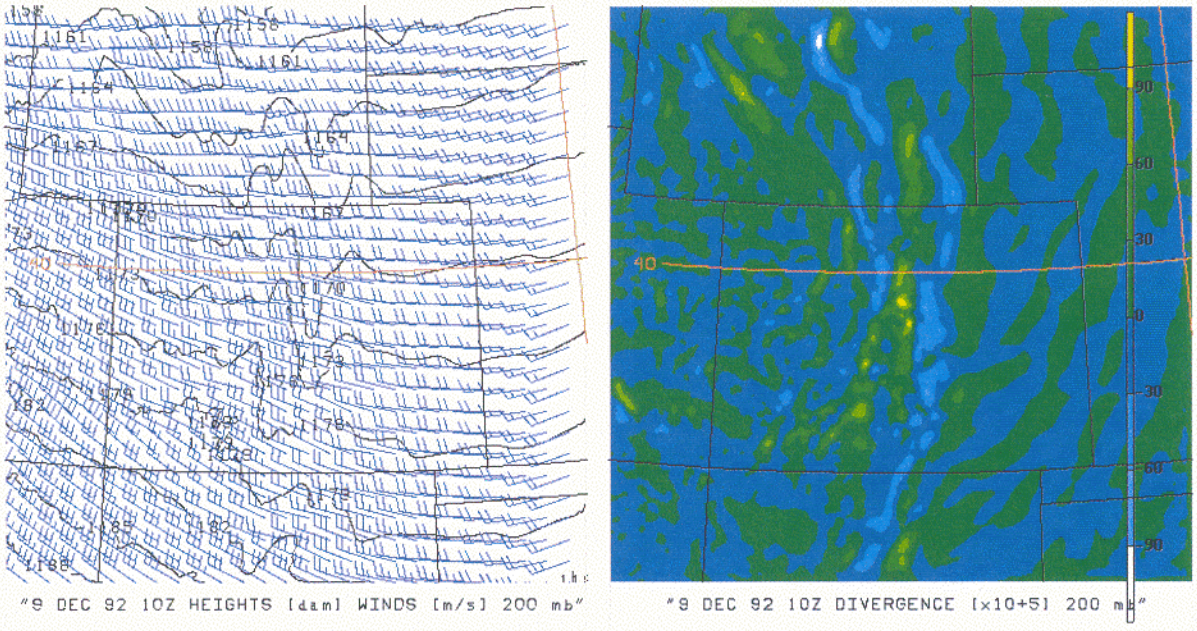


b)

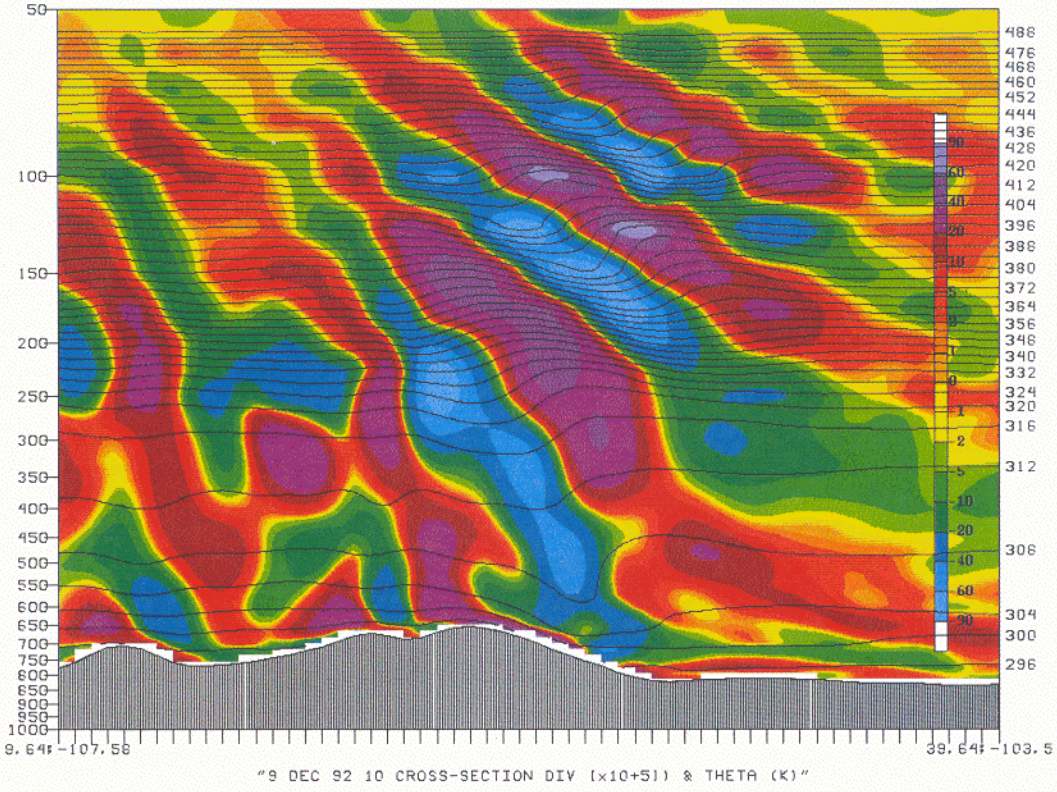


Figure 6. 6-km NHMASS simulated a) 200-hPa winds (m/s), heights (dam) and velocity divergence ($s^{-1}$ x $10^{-5}$) and b) vertical cross section of potential temperature (K) and velocity divergence ($s^{-1}$ x $10^{-5}$) valid at 1000 UTC 9 December 1992.

a)

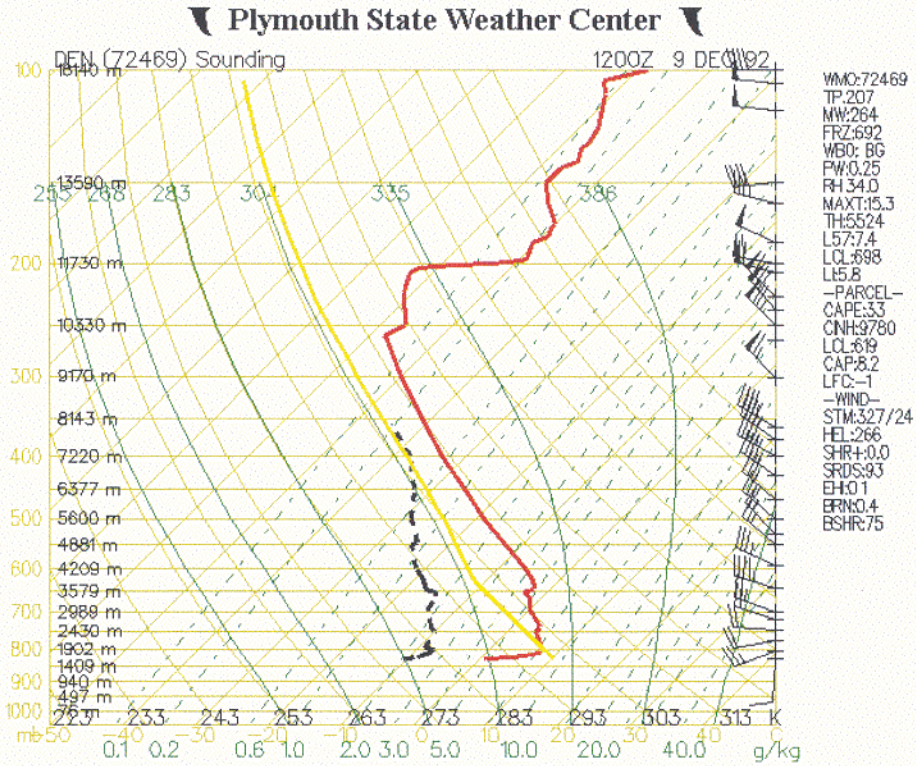


b)

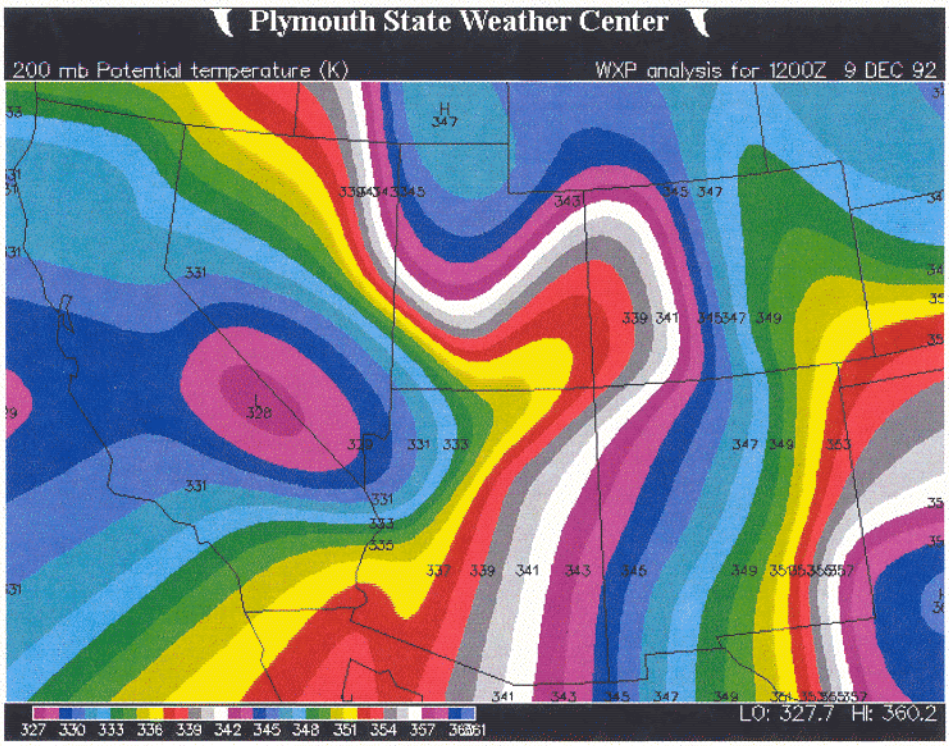


Figure 7. a) Observed sounding at Denver, Colorado, valid at 1200 UTC 9 December 1992. and b) observed potential temperature (K) at 200 hPa.

c)

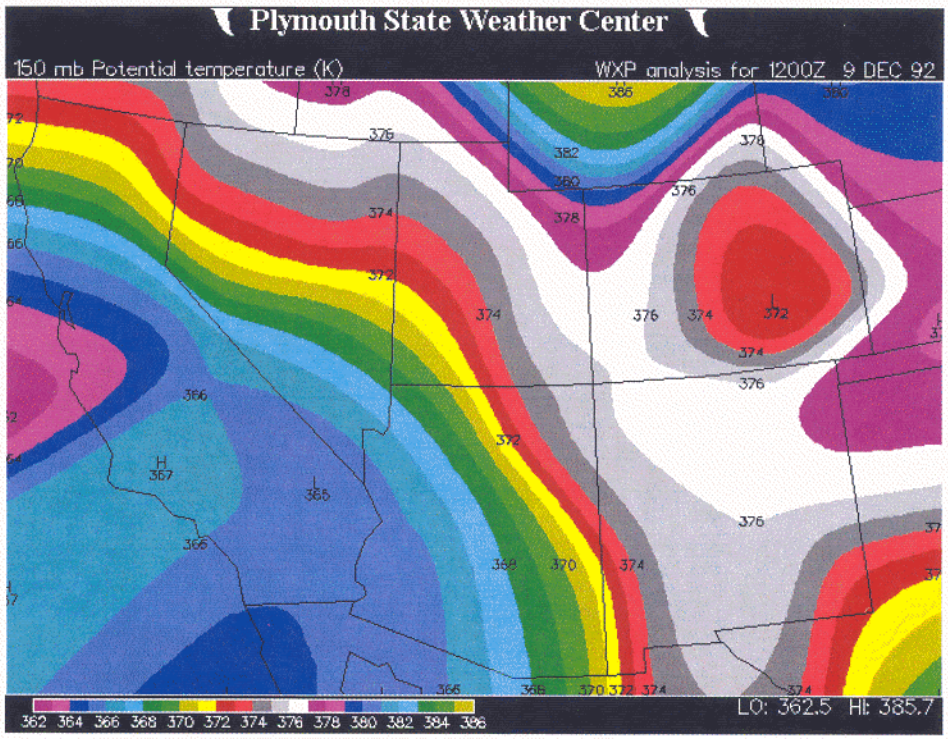


d)

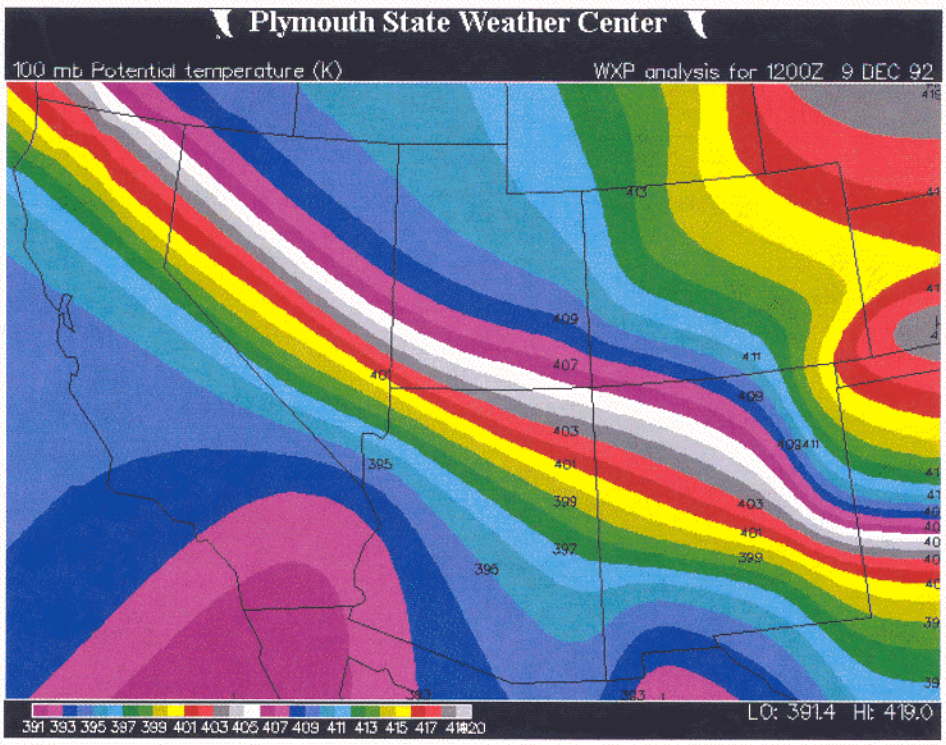


Figure 7.(cont.). Observed potential temperature (K) at c) 150 hPa and d) 100 hPa valid at 1200 UTC 9 December 1992.

a)

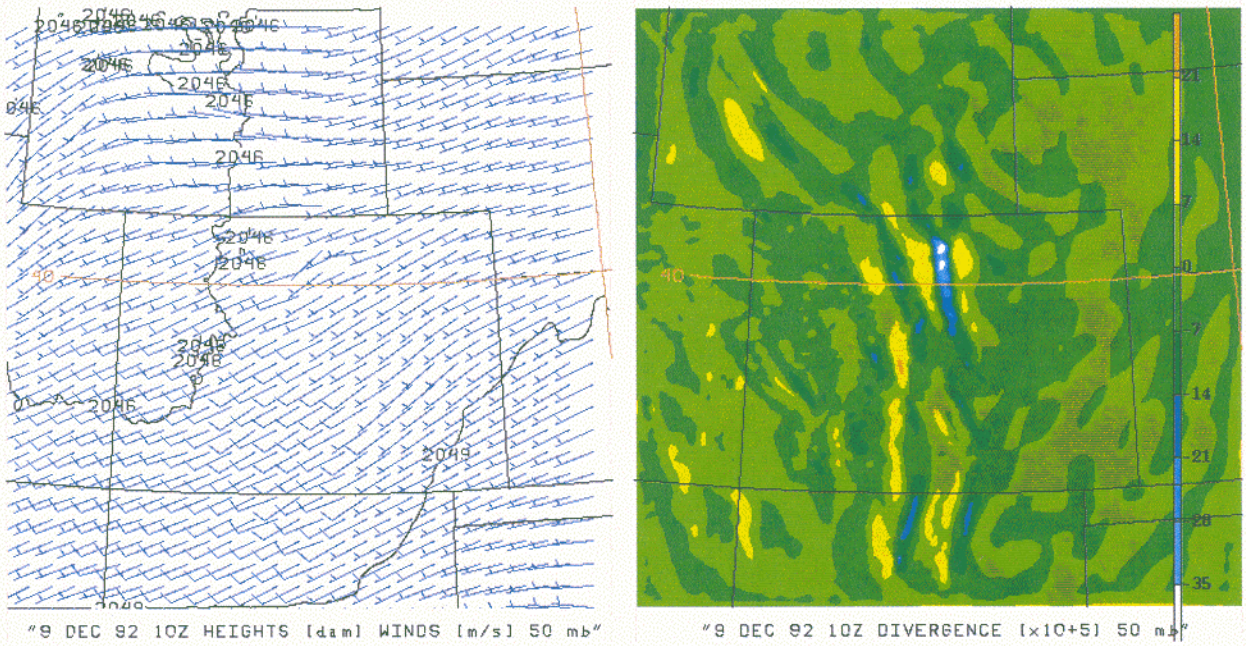


b)

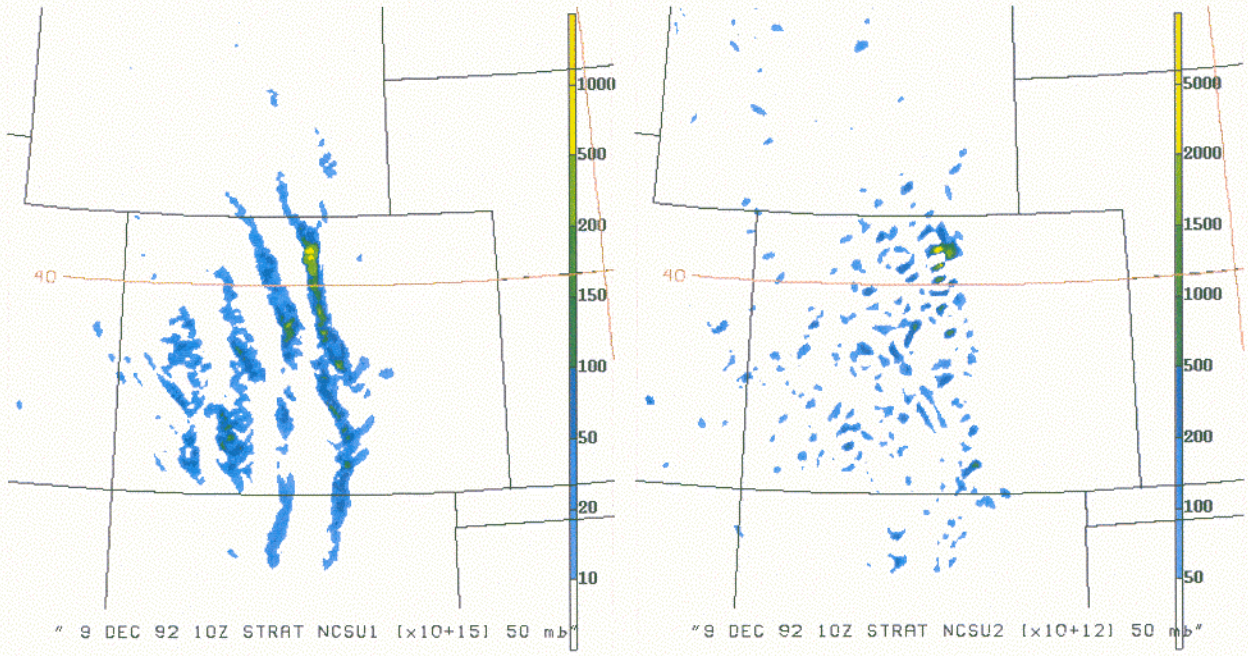


Figure 8. 6-km NHMASS simulated a) 50-hPa winds ($ms^{-1}$), heights (dam) and velocity divergence ($s^{-1}$ x $10^{-5}$) and b) 50-hPa NCSU 1 and 2 indices valid at 1000 UTC 9 December 1992.

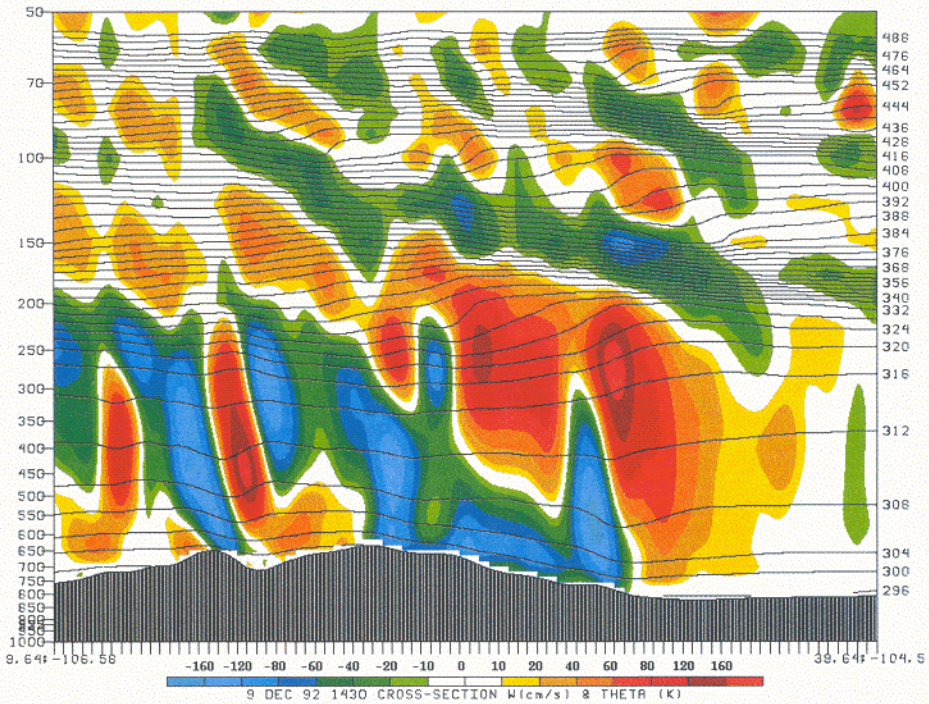


Figure 9. 2-km NHMASS simulated vertical cross section of potential temperature (K) and velocity divergence ($s^{-1}$ x $10^{-5}$) valid at 1430 UTC 9 December 2002.

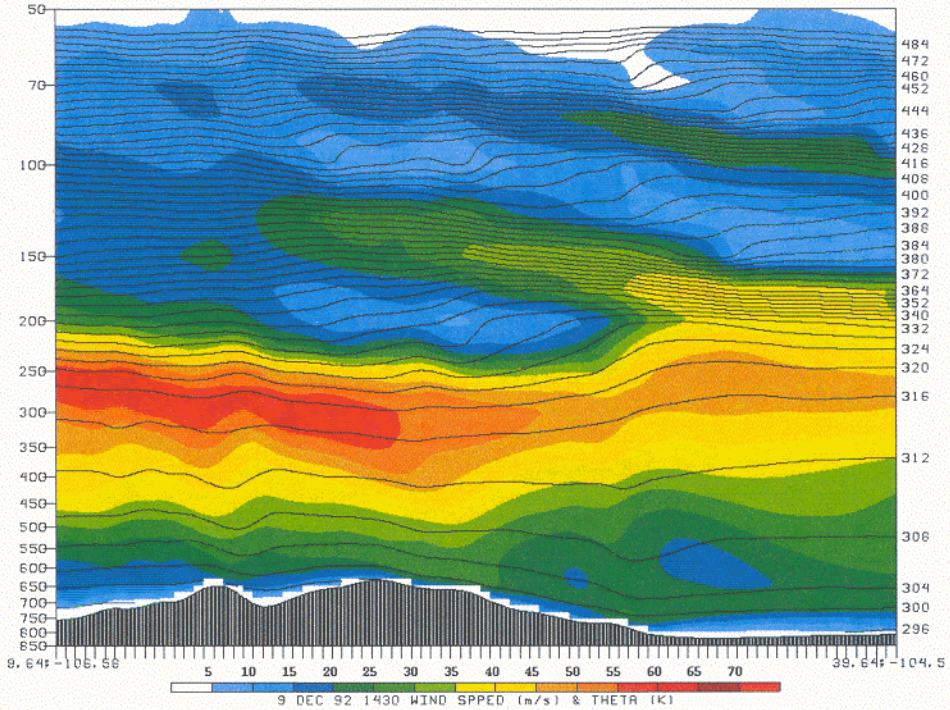


Figure 10. 2-km NHMASS simulated vertical cross section of potential temperature (K) and wind velocity ($ms^{-1}$) valid at 1430 UTC 9 December 2002.

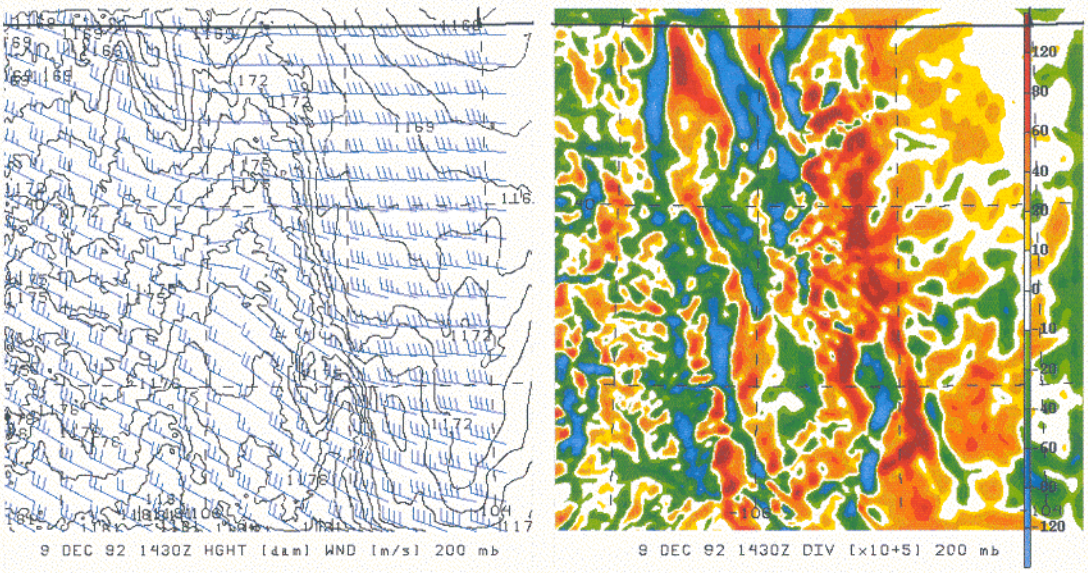


Figure 11. 2-km NHMASS simulated 200-hPa winds ($ms^{-1}$), heights (dam) and velocity divergence ($s^{-1}$ x $10^{-5}$) valid at 1430 UTC 9 December 2002.

driven by this type of frontogenetical feature signaling a region of possible gravity wave genesis and breaking due to shearing instability where the Scorer parameter varies substantially in the vertical (Figures 13a and b). Wave critical layer formation and reduced Richardson numbers are favored in this region as can be inferred from the left side of Figure 14 near 200 hPa. This occurs upstream from the accident location (note star in Figure 13) thus forcing the nested grid to be shifted slightly northwest of the accident.

Stage III is established when the shear and instability near 200 hPa in the region of strong Scorer parameter variation in the vertical creates shear-induced gravity waves and vortices that can increase the turbulence kinetic energy resulting in increased eddy dissipation rates accompanying wave overturning. A preferred location would be in the lightly shaded areas in Figure 14 where the Richardson number is below critical values.

The juxtaposition of velocity convergence on the western side of this wave generation zone (Figures 9 and 11) with the perturbed 338-K isentrope is a preferred region for a strong shaft of descending air just a few kilometers to the west of and upstream of the accident denoted by a star in Figure 14 at 1507 UTC. The strong descent is the result of a significant vertical increase in velocity convergence near the vertical variation of lapse rate from increasingly stable to increasingly unstable air. Hence, subsiding air is descending into a progressively more negatively buoyant environment as a cool air parcel encounters and is sinking into a much warmer air below the cold layer. This shaft of descent is occurring within a region of strong Scorer parameter variation (at ~11,500 m) with respect to height as well as being within advective range of the accident location only a few kilometers downstream and about 1750 m below.

The 667-m autonesting has located the 222-m grid just upstream from the accident at 1430 UTC. In order to nest down to near Large Eddy Simulation (LES) scales of motion, i.e., 71 m, from the 222-m simulation, it is necessary to diagnose how

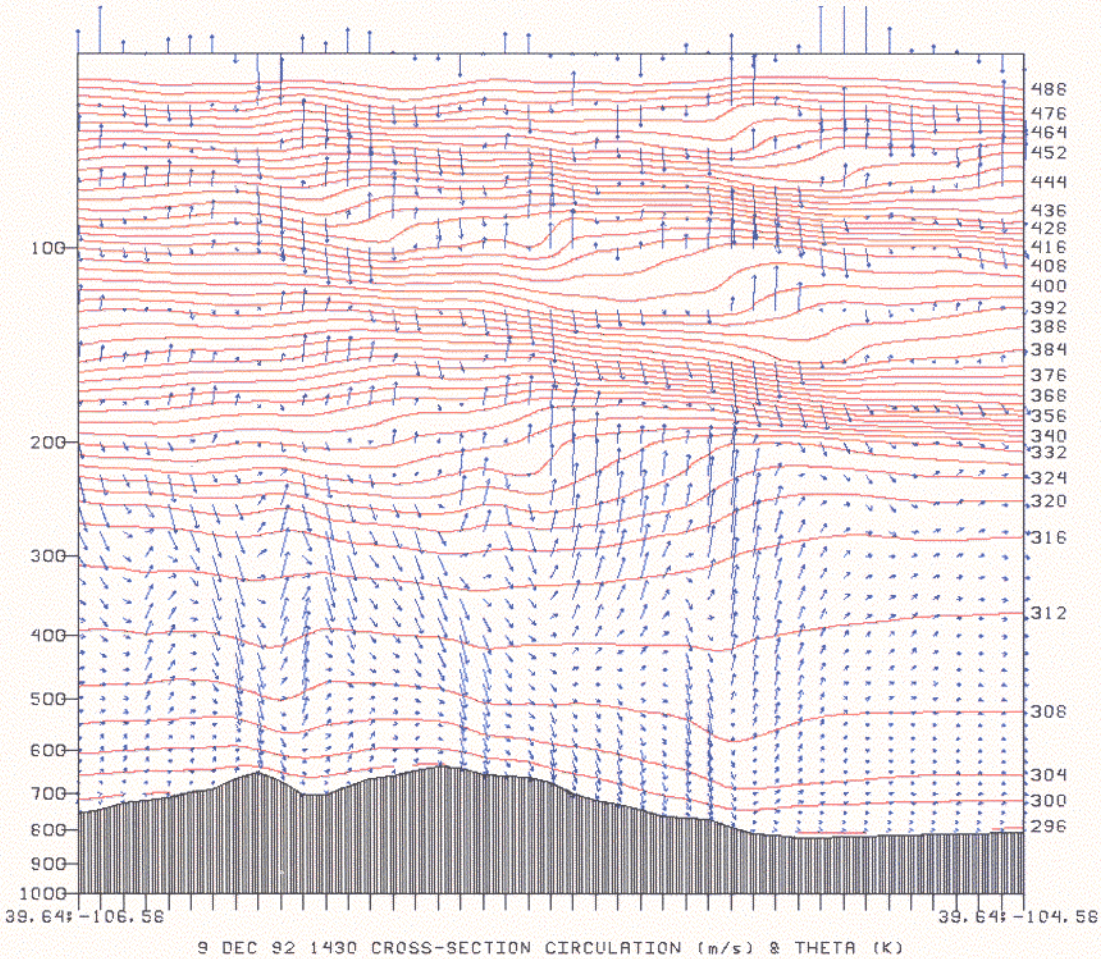


Figure 12. 2-km NHMASS simulated vertical cross section of potential temperature (K) and circulation vectors ($ms^{-1}$) valid at 1430 UTC 9 December 1992.

turbulence kinetic energy and eddy dissipation can be employed to select the time and location of the finest scale grid. Interestingly, strong fluxes of turbulence kinetic energy due to the nonuniform 3-dimensional advection and turbulent transports of turbulence kinetic energy (not shown) become significant in the 222-m simulation just downstream from the Scorer parameter gradient maximum in that simulation which is closely aligned with the descending shaft of momentum depicted on the left side of Figure 14. The descending momentum shaft is established by the mass adjustments and thermal adjustments accompanying the 3-dimensional frontogenetical circulations. The calculation of explicit turbulence kinetic energy fluxes depicted in Figure 15 at 1500 UTC from the 222-m simulation indicates that the explicit fluxes in the critical layer are very large just downstream from the Scorer parameter variation and downward shaft of momentum and subsequently select the region for the 71-m nest because of their correlation with eddy dissipation rate maxima. This occurs as the downward fluxes penetrate the layer of mechanical generation of turbulence kinetic energy close to the accident location (not shown).

a)

b)

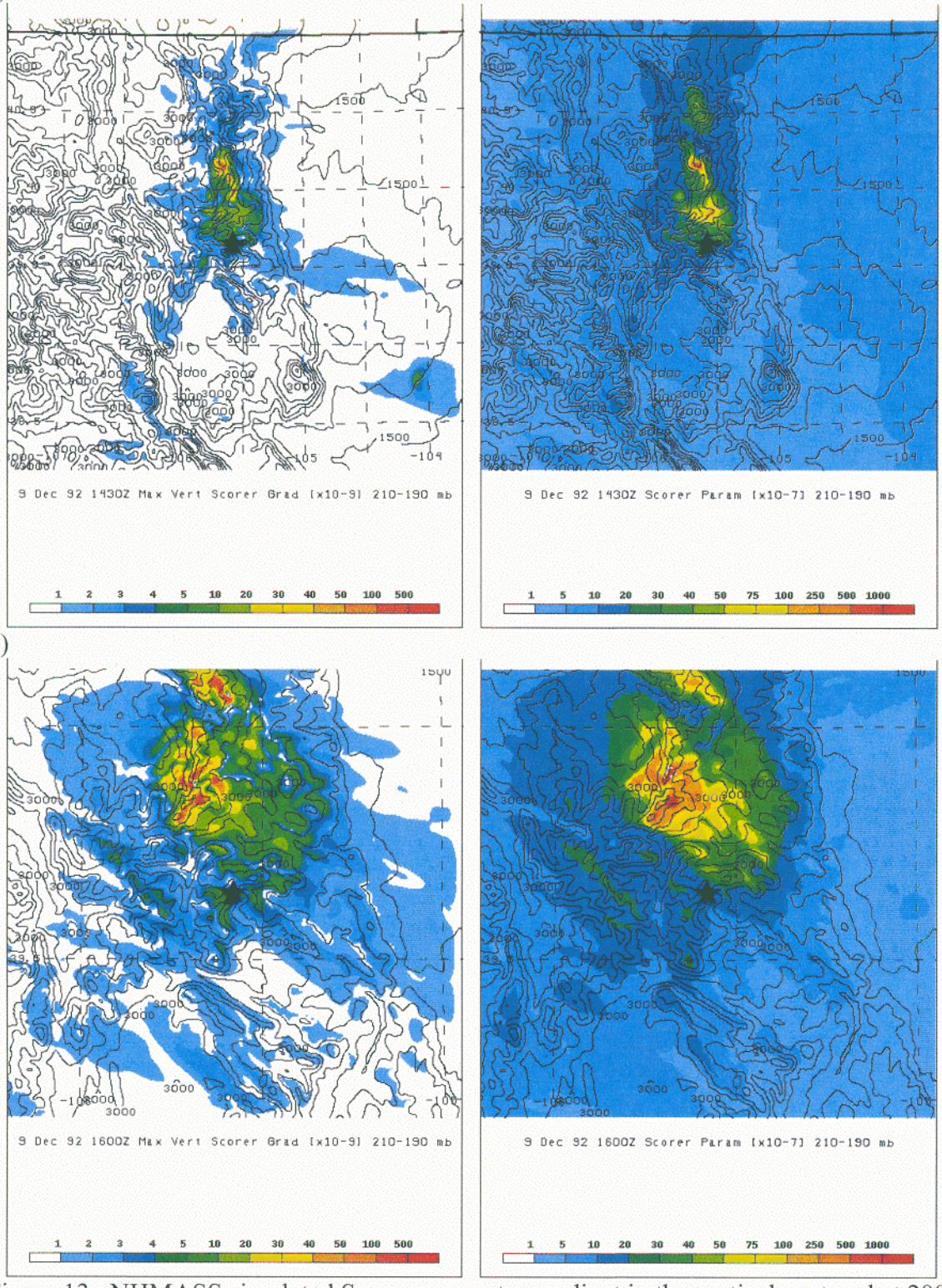


Figure 13. NHMASS simulated Scorer parameter gradient in the vertical centered at 200-hPa and 200-hPa Scorer parameter ($m^2$) valid for the a) 2-km simulation valid at 1430 UTC and b) 667-m simulation valid at 1509 UTC 9 December 1992. Star marks location of the aircraft accident.

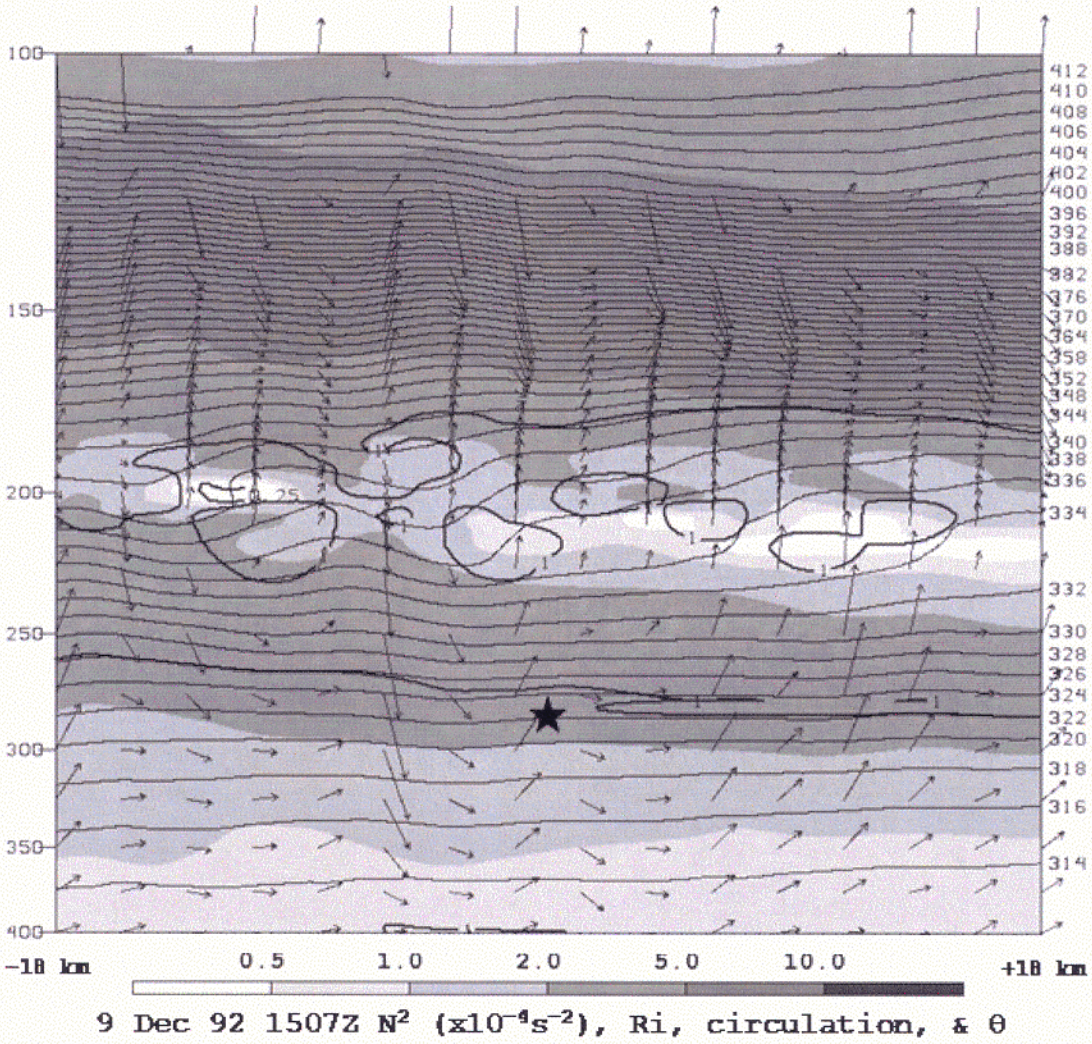


Figure 14. 222-m NHMASS simulated vertical cross section of Brunt-Väisälä frequency squared ($s^{-2}$), Richardson number, circulation vectors and potential temperature valid at 1507 UTC 9 December 1992.

Within this nest, at 1507 UTC, one can see in Figures 14, 16, and 17 that the descending shaft of momentum at 275 hPa, the accident pressure level, approaches 10 m/s in magnitude closely juxtaposed to both flow-aligned shear-induced gravity waves propagating through a layer of flow parallel anticyclonic horizontal vorticity, which is vertically juxtaposed with flow parallel positive horizontal vorticity just below. Hence, the eddy dissipation process and accident space/time location contain juxtaposed horizontally propagating gravity waves towards the east-southeast as well as ample horizontal vortex tube forcing thus indicating the possibility that this interaction between a descending shaft of momentum and horizontal vortex tubes may have caused the turbulence that affected the aircraft in question. This conclusion was also hypothesized by Clark et al. (2000).

a)

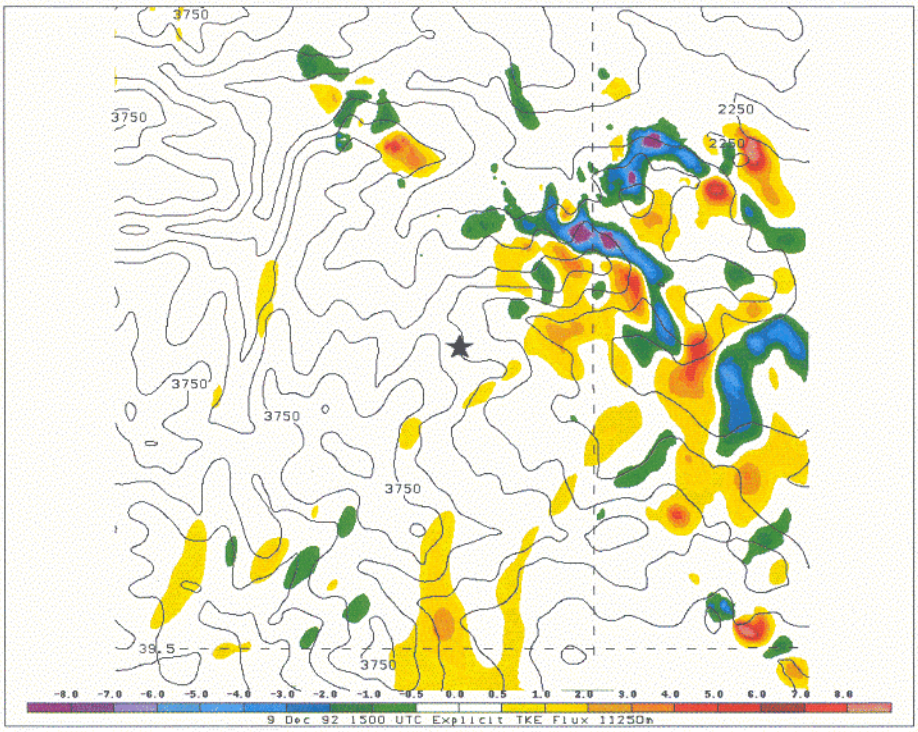


b)

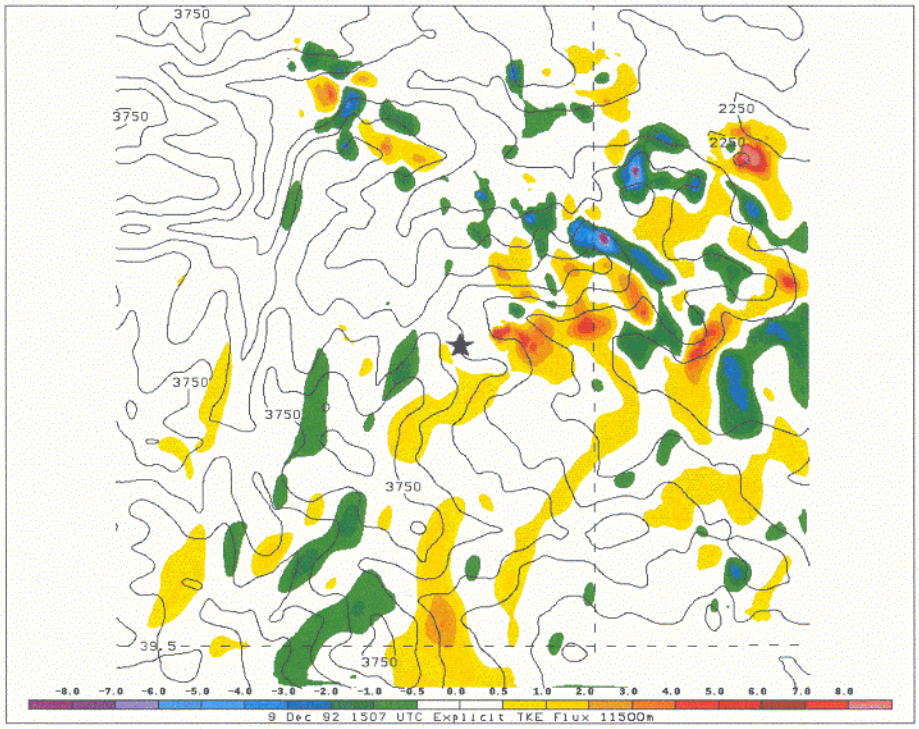


Figure 15. 222-m NHMASS simulated explicit flux of turbulence kinetic energy ($m^3s^{-3}$) valid at a) 11250 m and 1500 UTC and b) 11,500 m and 1507 UTC 9 December 1992.

c)

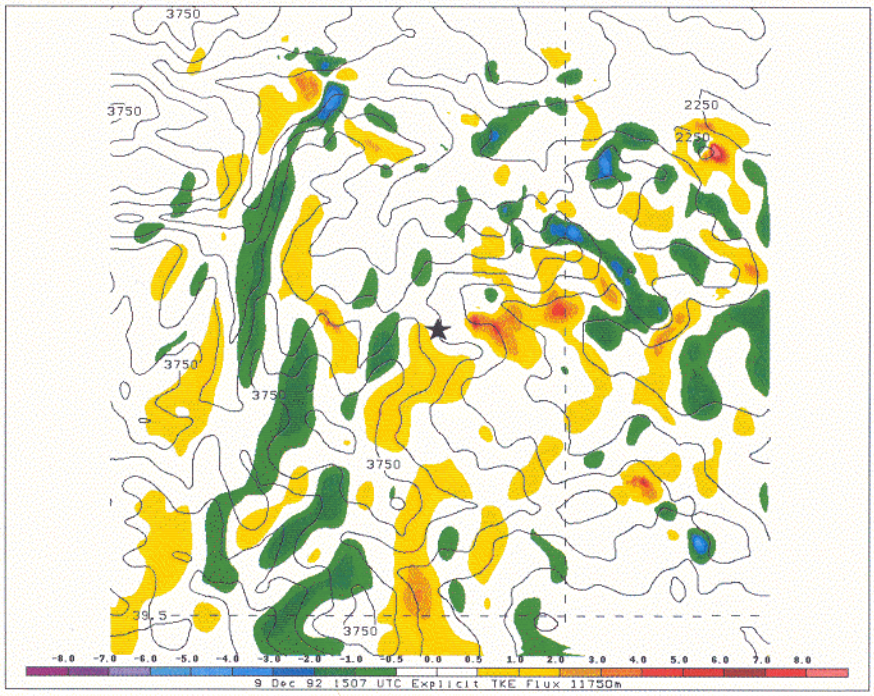


15 (cont.). 222-m NHMASS simulated explicit flux of turbulence kinetic energy ($m^3s^{-3}$) valid at c) 11,750 m and 1507 UTC 9 December 1992.

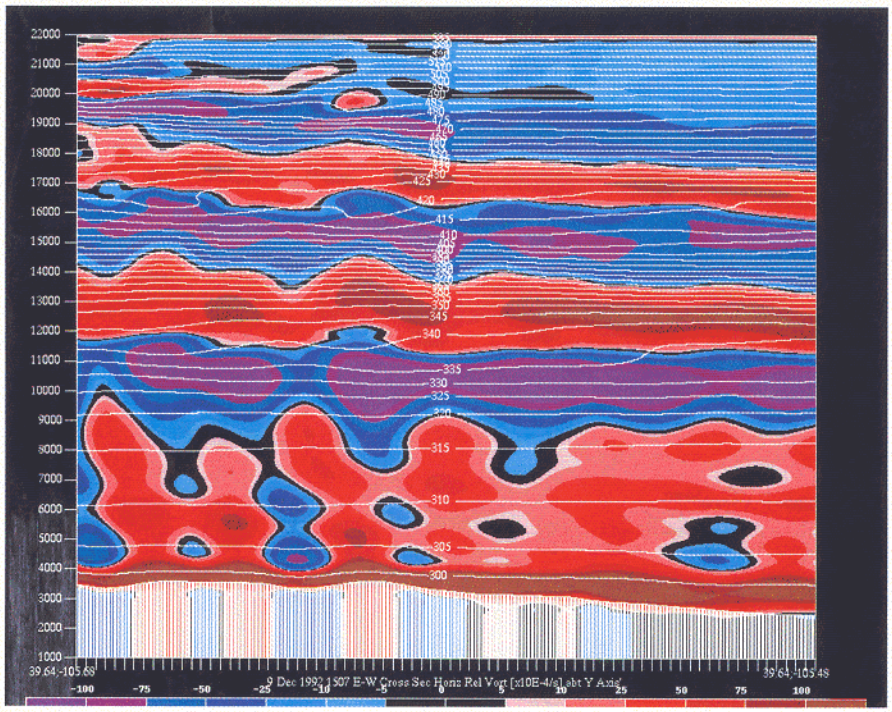


Figure 16. 222-m NHMASS simulated vertical cross section of X-space vorticity ($s^{-1}$ x $10^{-4}$) valid at 1507 UTC 9 December 1992.

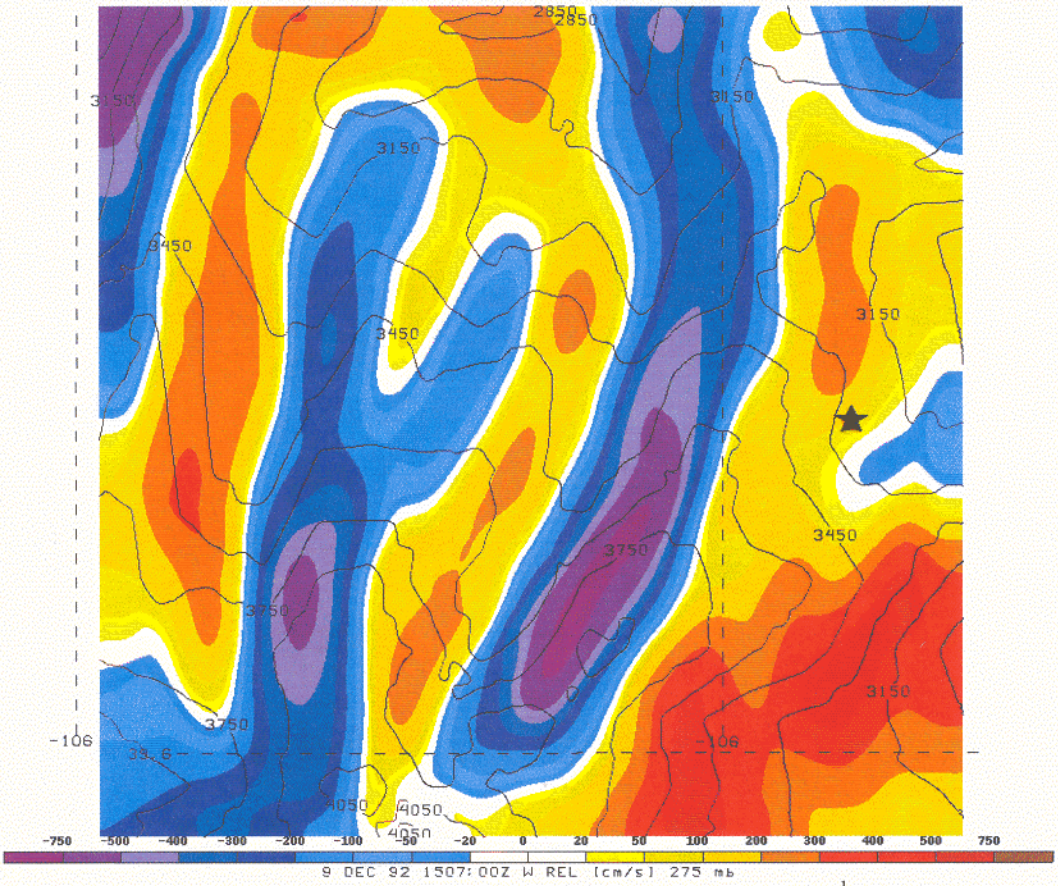


Figure 17. 71-m NHMASS simulated 275-hPa vertical motion ($cms^{-1}$) valid at 1507 UTC 9 December 1992.

## 5. CONCLUSIONS

The second year of research showed continued major progress towards the development of a stratospheric real-time turbulence modeling system. During this period, the stratospheric NHMASS model continued to be tested on 3 new terrain-induced turbulence research case studies. Results of the simulated fields were satisfactory when validated against conventional and asynoptic observations. The autonest algorithm was reformulated and tested on these 3 new research case studies.

***The algorithm was modified based on a 3-stage paradigm of intense wave turbulence generation. During stage I, a buoyancy perturbation due to a local heating source such as adiabatic warming during cross-mountain flow or latent heat release in moist convection produces a localized mass perturbation that extends from the troposphere deep into the stratosphere. The mass perturbation then acts to perturb the horizontal gradient of wind, which is already substantial accompanying multiple vertically stacked jet exit/entrance region/frontal features in the troposphere and stratosphere, i.e., the polar jet, subtropical jet and weaker midstratospheric jet/front systems. The magnitude of this adjustment process is substantially enhanced by the upward increase of the convergence of anticyclonic relative vertical vorticity accompanying stratospheric jet/frontal systems. The interaction yields vertically***

***sloping and vertically varying mass flux divergence/convergence fields that produce vertically varying vertical circulations. They vary in magnitude in time as the numerous vertically stacked jet streaks propagate through the region experiencing local mass and buoyancy perturbations accompanying local heating sources. Typically, convergence of mass in the stratosphere and divergence of mass in the troposphere facilitates the downward building of the severe turbulence environment. Orthogonal to these vertically stacked circulations are mesoscale PV banners caused by the nonuniform drag of the buoyancy perturbation on the horizontal flow fields. As these vertically stacked circulations intensify, they organize stage II.***

***During stage II, the vertically varying vertical circulations create vertical fronts where the static stability gradients in the vertical become even more inhomogeneous. This inhomogeniety creates regions of complex vertical gradients of the Scorer parameter associated with regions where the Brunt-Väisälä frequency, vertical wind shear, and Richardson number support subcriticality and shearing instability near wave critical layers. This induces local shear gravity waves to form aligned with the flow resulting in stage III.***

***During stage III, the amplifying flow-aligned gravity waves further modify the buoyancy fields resulting in preferred regions where sinking motions due to wave momentum fluxes become correlated with negative buoyancy gradients, i.e., convergence of mass occurs within a transitional layer that has relatively unstable air on top of relatively stable air. In this region, a descending shaft of momentum due to convergence is accelerated by the negative buoyancy resulting in subsequent interactions with the horizontal vorticity created by the PV banners. The downward flux of horizontal vorticity by this process is coincident with the local flux of turbulence kinetic energy into the polar jet wind maximum that forces eddies to achieve very rapid dissipation in the form of turbulent rotors that can become a serious obstacle to aviation safety as they cascade down to the characteristic scale of an aircraft and its response function.***

Synthesizing this into an automated nesting index from the synoptic to the turbulence scales of atmospheric motion is very difficult, but success has been achieved by employing a sequence of indices, i.e., the NCSU1 index, vertical gradient of Scorer parameter, and eddy dissipation rate. Finding thresholds and criteria associated with these indices is very difficult given the diversity of atmospheric flow regimes.

The ability of the model to simulate fine -cale terrain-induced and convective features including gravity wave phenomena as well as the autonest to direct the model grid nests to finer scales in regions of likely turbulence-organizing circulations indicates the potential for its use in predicting turbulence-generating regions. However, validation of the modeling system lags its development and testing due to the lack of stratospheric turbulence observations.

## 6. RECOMMENDATIONS

There is a continuing need for information concerning observed turbulence reports in the lower stratosphere in the existing simulated and future simulated case studies to validate the modified and evolving modeling system.

## REFERENCES


Clark, T. L., W. D. Hall, R. M. Kerr, D. Middleton, L. Radke, F. M. Ralph, P. J. Nieman, and D. Levinson, 2000: Origins of aircraft-damaging clear air turbulence during the 1992 Colorado downslope windstorm: numerical simulations and comparisons with observations. J. Atmos. Sci., 57, 1105-1131.

Ellrod, G. P., and Knapp, D. I., 1992: An objective clear air turbulence forecasting technique: Verification and operational use. Wea. Forecasting, 7, 150-165.

Kaplan, M. L., S. E. Koch, Y.-L. Lin, R. P. Weglarz, and R. A. Rozumalski, 1997: Numerical simulations of a gravity wave event over CCOPE. Part I: The role of geostrophic adjustment in mesoscale jetlet formation. Mon. Wea. Rev., 125, 1185-1211.

Kaplan, M. L., Y.-L. Lin, J. J. Charney, K. D. Pfeiffer, D. B. Ensley, D. S. DeCroix, and R. P. Weglarz, 2000: A Terminal Area PBL Prediction System at Dallas-Fort Worth and its application in simulating diurnal PBL jets. Bull. Amer. Meteor. Soc., 81, 2179-2204.

Kaplan, M. L., K. M. Lux, J. D. Cetola, A. W. Huffman, A. J. Riordan, S. W. Slusser, Y.-L. Lin, J. J. Charney, and K. T. Waight, 2004: Characterizing the severe turbulence environments associated with commercial aviation accidents. A Real-Time Turbulence Model (RTTM) designed for the operational prediction of hazardous aviation turbulence environments. NASA/CR-2004-213025.

Kaplan, M. L., J. J. Charney, K. T. Waight III, K. M. Lux, J. D. Cetola, A. W. Huffman, A. J. Riordan, S. D. Slusser, M. T. Kiefer, P. S. Suffern, and Y.-L. Lin, 2006: Characterzing the severe turbulence environments associated with commercial avaiation accidents. A Real-Time Turbulence Model (RTTM) designed for the operational prediction of hazardous aviation turbulence environments. In press, Meteor. Atmos. Phys.

Marroquin, A., 1998: An advanced algorithm to diagnose atmospheric turbulence using numerical model output. Preprints, 16th AMS Conference on Weather Analysis and Forecasting, 11-16 January, 79-81.

Sharman, R., C. Tibaldi, G. Wiener, and J. Wolff, 2006: An integrated approach to mid- and upper-level turbulence forecasting. Wea. Forecasting, 21, 268-287.

Stull, Roland B., 1988: *An Introduction to Boundary Layer Meteorology*. Kluwer Academic Press: 639 pp.

## Appendix A

# NUMERICAL INVESTIGATIONS OF THE EVOLUTION OF MOUNTAIN-INDUCED TURBULENCE ALONG THE COLORADO ROCKIES ON 9 DECEMBER 1992

David R. Vollmer[1], Yuh-Lang Lin[1], and Michael L Kaplan[2]
[1]North Carolina State University, Raleigh, North Carolina
[2]Desert Research Institute, Reno, Nevada

## 1. INTRODUCTION

On December 9, 1992, a broad area of turbulence associated with orographically forced gravity waves occurred along the Rocky Mountains from Wyoming and Utah south through New Mexico and extended from near the surface into the lower stratosphere. Pilot reports of turbulence were widespread and numerous throughout the day. At 1507 UTC, a DC-8 cargo aircraft encountered extreme turbulence which severed a section of wing and one of its engines while it was attempting to cross the Front Range just west of Denver (Ralph et al. 1997).

## 2. BACKGROUND AND METHODOLOGY

This case was studied by Clark et al. (2000), who used numerical simulations and observations to analyze the event in the vicinity of the aircraft incident. Clark et al. proposed several possible mechanisms for the turbulence which caused the aircraft accident, including Holmboe instability and jet imbalance.

The present study uses the stratospheric Non-Hydrostatic Mesoscale Analysis Simulation System (NHMASS) Version 6.4 developed by MESO, Inc. Initialization data were obtained from the Global Reanalysis dataset. The model was run at grid lengths of 18 km, 6 km, 2 km, 667 m, 222 m, and 71 m. The model used 90 vertical (sigma) levels with an emphasis on the lower stratosphere. The larger two grid lengths used Kain-Fritsch cumulus parameterization and all runs used a two-dimensional Turbulence Kinetic Energy (TKE) planetary boundary layer (PBL) scheme. Runs from 18 km to 222 m were centered on the aircraft accident location (39.64 N 105.58 W), and the 71 m run was centered slightly west to capture the finer upstream structure.

## 3. MODEL RESULTS

Two major synoptic features were present that day which served to set the stage for the extreme turbulence observed. Most prominent was a jet streak propagating into the region from the northwest (Fig. 1) and an upper-level front supporting it. At the larger scale, two major wave modes were found in the vertical velocity and divergence fields along the lee of the Colorado Rockies: a standing hydraulic jump and a downstream propagating wave which was likely associated with the jet-front system. Cross-sections (along AB as denoted in Fig. 1) at grid spacing as coarse as 2 km showed steep isentropes and vertical velocities in the hydraulic jump in excess of 1.5 $ms^{-1}$ (Fig.

2). Energy from the gravity wave associated with the hydraulic jump was shown to penetrate the lower stratosphere. The hydraulic jump was the most obvious of the terrain-induced disturbances, but gravity waves were found to occur on much finer scales as well. Potential vorticity (PV) banners were found to occur on the lee side of the mountains behind the upper-level front (Fig. 3), extending almost completely across the state of Colorado by the end of the period. The maximum wave activity generally occurred in the left exit region of the jet streak entering the area from the northwest and in association with the upper-level front.

At finer scales, gravity waves were found to have been generated both from the terrain and from indirect circulations associated with the jet streak. Model output from runs with grid lengths of 2km and less clearly showed smaller gravity waves which were generated in an unstable layer between the polar and subtropical jets. This layer was characterized by relatively lower Brunt-Väisäla frequency squared ($< 10^{-4}$ $s^{-2}$) and Richardson number ($< 1$), as well as steep isentropes. It is in this layer that we hypothesize the turbulent energy which caused the aircraft accident originated.

## 4. ANALYSIS

We hypothesize that there was a downward cascade of energy from higher to lower scale vortices which interacted to account for the abundant turbulence and mountain wave activity seen on 9 December 1992. The first feature was the thermally-indirect circulation associated with the exit region of the jet streak and the upper-level front as indicated by the synoptic-scale isentropic gradient. A meso-$\gamma$ scale flow-aligned frontal boundary was found to exist in the potential temperature fields at finer model resolution. This frontogenesis was caused by the perturbation of the jet streak by the orography in a similar way to that found by Kaplan and Karyampudi (1992). Flow-aligned vortices and gravity waves were found to exist and were likely generated both by terrain and by interactions between finer jet structures. Lastly, cross-flow vortices were found at the smallest grid-length, whose exact structure and energy budgets remain unknown due to limitations in model resolution. Relative vorticity fields at 71 m grid spacing showed both a flow-aligned and a cross-flow structure at the level of the aircraft accident, indicative of these two circulation regimes (Fig. 4).

A possible mechanism for the turbulent energy which led to the aircraft incident is examined. At 222 m and 71 m, the model generated areas of near-zero $N^2$ coinciding with those of $Ri<.25$ at roughly 200 hPa (Fig. 5), both values traditionally associated with static and shear instabilities (Lin 2007). Here the isentropic deformation from both the larger-scale circulation and the terrain-induced meso-front coincided, leading to flow-aligned gravity waves. The flow circulation was structured such that wave energy from this unstable layer could have been reflected downward and advected downstream, toward the location of the aircraft incident (at approximately 278 hPa in the 222 m simulation). An examination of vertical flux of horizontal momentum ($\overline{u'w'}$) showed flux convergence in the vicinity of and near the time of the aircraft accident. In addition, a wave-induced critical level may have developed in the unstable layer, as indicated by isentrope overturning, which could have served to overreflect wave energy propagating upward from the surface terrain, a process described by Smyth and Peltier (1989). These overturned isentropes indicate possible wave-breaking. Anticyclonic flow-parallel

vorticity found in this area may have been indicative of vortex tube formation which could have also been driven downward toward the accident location by the flow-aligned gravity wave circulations.

## 5. CONCLUSIONS

Numerical simulations of this mountain wave case indicated that turbulence can be generated through the interaction between an approaching jet streak and gravity waves generated by rough topography. When the juxtaposition of these features is optimized, the resultant gravity waves and wave-breaking can create extreme turbulence of a magnitude capable of causing structural damage or failure to an aircraft as happened on 9 December 1992.

## 6. ACKNOWLEDGEMENTS

This research is funded by Air Force grant FA8718-04-C-0011. Special thanks go to Ken Waight of MESO, Inc., for extensive modeling support and for the initialization data. The authors would also like to thank Chad Ringley for exploring the turbulent flux fields from this case, and Zachary Brown and Paul Suffern for their invaluable input and support.

## 7. REFERENCES

Clark, T. L., W. D. Hall, R. M. Kerr, D. Middleton, L. Radke, F. M. Ralph, P. J. Neiman, and D. Levinson, 2000: Origins of aircraft-damaging clear-air turbulence during the 1992 Colorado downslope windstorm: numerical simulations and comparison with observations. *J. Atmos. Sci.*, **57**, 1105-1131.

Kaplan, M. L. and V. M. Karyampudi, 1992. Meso-beta scale numerical simulations of terrain-drag induced along-stream circulations. Part I: Midtropospheric Frontogenesis. *Meteorol. Atmos. Phys.*, **49,** 133-156.

Lin, Y.-L., 2007: *Mesoscale Dynamics*, Cambridge University Press.

Ralph, F. M., P. J. Neiman, and D. Levinson, 1997: Lidar observations of a breaking mountain wave associated with extreme turbulence. *Geophys. Res. Lett.*, **24,** 663-666.

Smyth W. D. and W. R. Peltier, 1989. The transition between Kelvin-Helmholtz and Holmboe instability: an investigation of the overreflection hypothesis. *J. Atmos. Sci.*, **46,** 3698-3720.

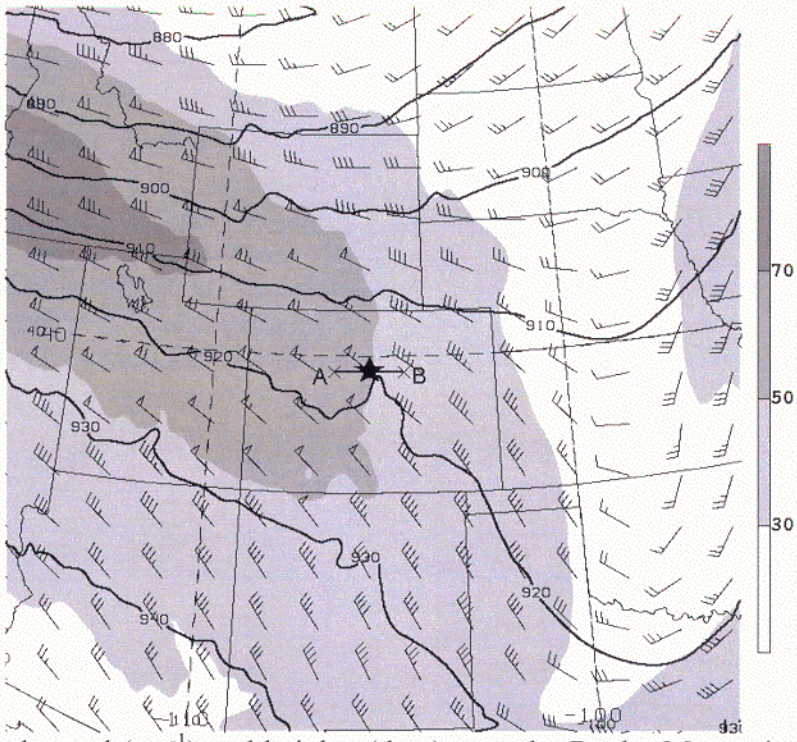


Figure 1: Wind speed ($ms^{-1}$) and heights (dam) over the Rocky Mountains at 1500 UTC 9 December 1992, from 18 km NHMASS model output. Aircraft accident location denoted by star.

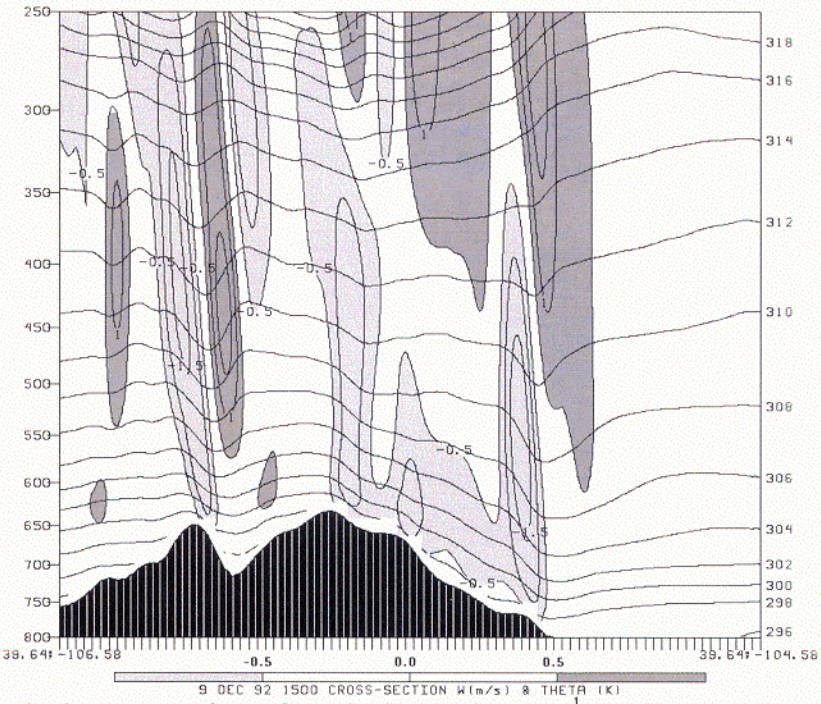


Figure 2: Vertical cross-section of vertical velocity ($ms^{-1}$) and potential temperature (K) through the accident location at 1500 UTC 9 December 1992 from 2 km NHMASS model output. Vertical scale is pressure in hPa. The cross-section is denoted as AB in Fig. 1.

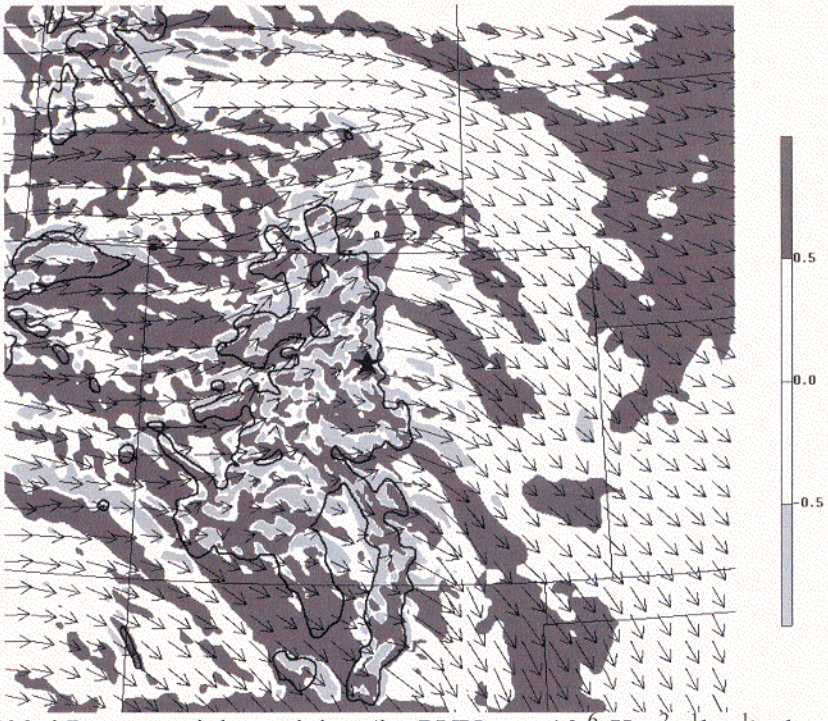


Figure 3: 700 hPa potential vorticity (in PVU, or $10^{-6}$ $Km^2s^{-1}kg^{-1}$), horizontal wind vectors (length proportional to speed in $ms^{-1}$), and 2500 m terrain contour for 1500 UTC 9 December 1992, from 6 km NHMASS model output. Aircraft accident location denoted by star.

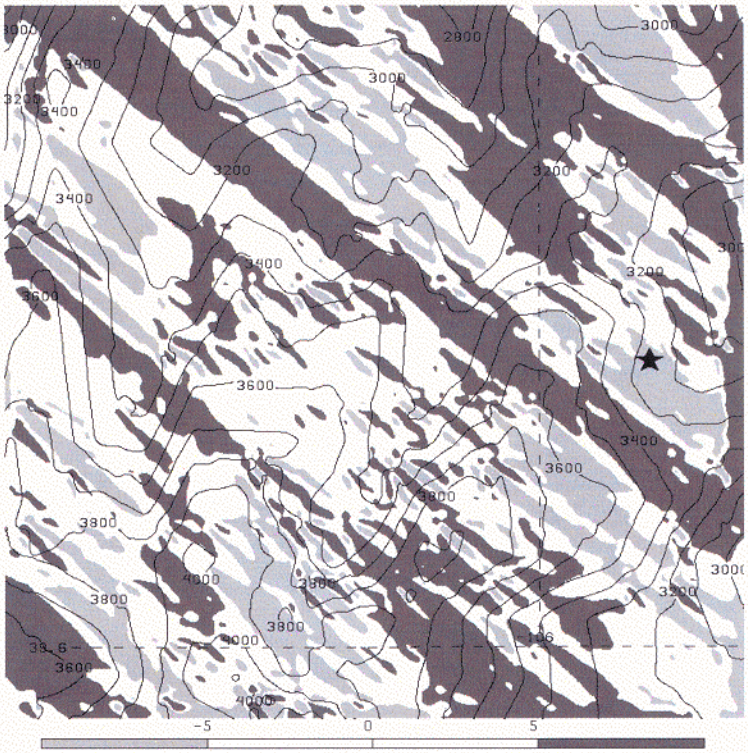


Figure 4: 275 hPa relative vorticity ($\times 10^{-4}$ $s^{-1}$) and terrain contours (100 m interval) for 1507 UTC 9 December 1992 from 71 m NHMASS model output. Aircraft accident location denoted by star.

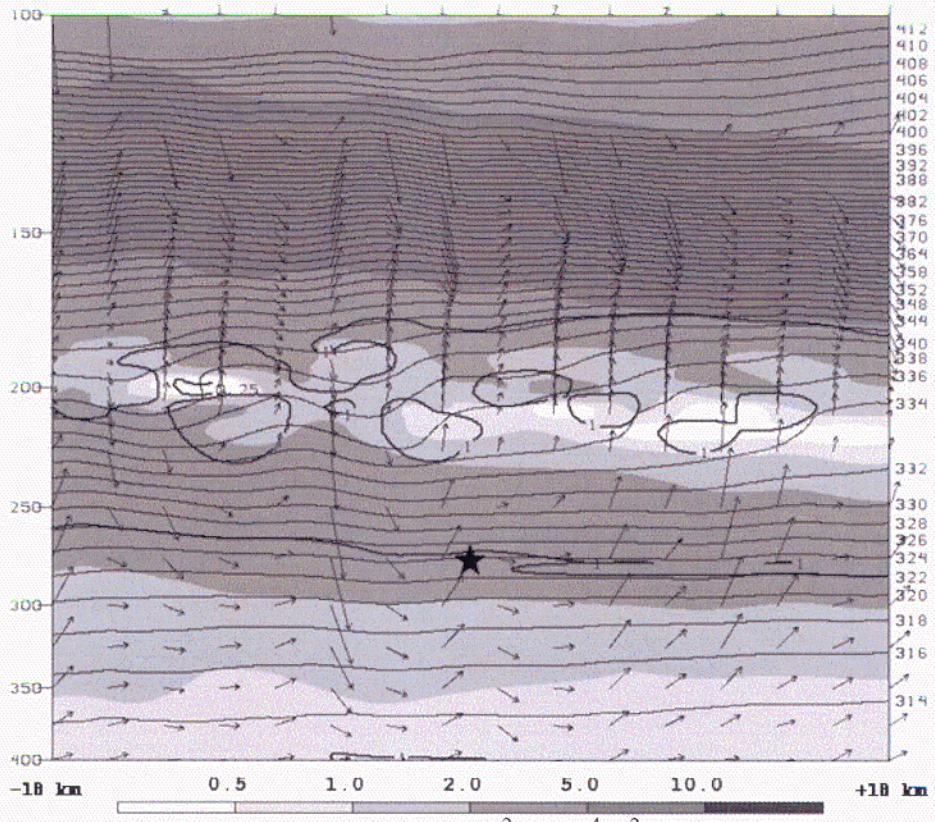


Figure 5: Vertical east-west cross-section of $N^2$ ($\times 10^{-4}$ $s^{-2}$, shading), Richardson number, x-P circulation ($ms^{-1}$), and potential temperature (K) at 1507 UTC 9 December 1992 from 222 m NHMASS model output. Vertical scale is pressure in hPa. Accident location is denoted by star.

## Appendix B

# AN INVESTIGATION OF TURBULENT PROCESSES IN THE LOWER STRATOSPHERE

Chad J. Ringley, Yuh-Lang Lin, P.S. Suffern
North Carolina State University, Raleigh, NC

Michael L. Kaplan
Desert Research Institute, Reno, NV

## 1. INTRODUCTION

The turbulent kinetic energy (TKE) tendency equation is widely applied to quantify turbulent tendency and eddy dissipation rate (EDR) within the planetary boundary layer (PBL). Due to the complexity that arises from Reynolds averaging, various approximation parameters, as described by Yamada and Mellor (1975) and Stull (1988), are often used to approximate the TKE tendency equation for idealized, measured, or simulated data. The application of the TKE tendency equation as a closed, solvable system is most common within the PBL, where friction and surface heating drive turbulent motion.

Though the strongest turbulent motions are, on average, confined to the PBL, turbulence is experienced at vertical levels well above the lowest 2 kilometers. Many previous authors have examined the effects of both convectively and orgraphically-induced gravity waves on turbulence well into the stratosphere. Lane et al. (2003) found a regime of turbulence just above the initial overshooting top associated with deep convection. In addition, Lane et al. (2003) described the gravity wave breakdown that occurred as high as 3 kilometers above the tropopause as another regime of turbulent motion. Both convectively and orgraphically-induced gravity waves are able to propagate well into the stratosphere due to the presence of high static stability and can reach heights that may threaten high-altitude flying aircraft. Lilly and Lester (1974) used observational data from aircraft to reveal sporadically-turbulent gravity waves generated by terrain over southern Colorado that reached heights of up to 17 kilometers. Leutbecher and Volkert (2000) performed a numerical simulation of an aircraft-related turbulence incident linked to orgraphically-induced gravity waves with heights up to 20 kilometers.

The breaking of a vertically propagating gravity wave would introduce the greatest threat to high-altitude flying aircraft, such as spy planes. Because there exists no prescribed limitation on where the TKE tendency equation is used, high vertical and horizontal resolution model simulations with high output frequency can be used to quantify individual terms within the TKE tendency equation with 1.5-degree closure at any level within the atmosphere. The purpose of this study is to apply the TKE tendency equation using a series of Reynolds averaging techniques in order to approximate TKE tendency associated with a vertically propagating gravity wave in the lower and middle stratosphere. By calculating each term in the TKE tendency equation explicitly, the study will help provide insight on the important physical processes related to turbulence

generation due to wave breaking.

## 2. METHODOLOGY

From Stull (1988), the TKE tendency equation can be written as:

$$\frac{\partial \bar{e}}{\partial t} = -\bar{u}\frac{\partial \bar{e}}{\partial x} - \bar{v}\frac{\partial \bar{e}}{\partial y} - \bar{w}\frac{\partial \bar{e}}{\partial z} + \frac{g}{\bar{\theta}_v}\overline{(w'\theta_v')} - \overline{(u'w')}\frac{\partial \bar{u}}{\partial z} - \frac{\partial}{\partial z}(\overline{w'e}) - \frac{1}{\bar{\rho}}\frac{\partial}{\partial z}(\overline{w'p'}) - \varepsilon \quad (1)$$

The form of the TKE tendency equation given in (1) does not require horizontal homogeneity as prescribed by Stull (1988). The terms on the right hand side of (1) are hereafter characterized by the definitions proposed by Stull (1988) and are as follows: the first three terms are the horizontal and vertical advection of TKE by the mean wind, the fourth term is buoyant production, the fifth term is mechanical shear, the sixth term is turbulent transport, the seventh term is pressure perturbations, and the eighth term is TKE dissipation or EDR. The form is very similar to the TKE tendency equation used in Kiefer (2005) with the addition of the horizontal advection terms.

The dependent variables on the right hand side of (1) are all known from the output of a numerical model simulation. A simple Reynolds averaging technique is used, represented by:

$$\Omega' = \Omega - \bar{\Omega} \quad (2)$$

where $\Omega$ represents any of the dependent variables (u,v,w, etc.) directly output from the model at each time step. The period over which the Reynolds averaging is performed will be varied in order to find the best structural representation of the vertically propagating gravity wave. Vertical and horizontal derivatives are calculated using a 2$^{nd}$-order centered finite difference scheme obtained from the model grids within the simulations. A series of programs and scripts were added to the normal model post-processing routine in order to perform the Reynolds averaging calculations and calculate each term independently.

## 3. MODEL SIMULATIONS

On 12 December 2002, a large amplitude surface gravity wave initiated deep moist convection over Eastern Texas and Western Louisiana. Figure 1 shows the surface gravity wave signature from a microbarogram in Palestine, TX. The "wave of depression" corresponds to 6-millibar pressure fall in a two-hour period near 2230 UTC 12 December 2002. A complete synoptic and mesoscale discussion of the parameters leading to the development of the event can be found in Suffern et al. (2005).

The convection generated due to the surface gravity wave became the subject of several high-resolution model simulations using the Non-Hydrostatic Stratospheric Mesoscale Atmospheric Simulation System, hereafter *Strato-NHMASS*. Figure 2 shows the model domain configurations for the Strato-NHMASS simulations over Eastern Texas and Western Louisiana. In order to better resolve the scales of motion required to accurately diagnose TKE tendency, several extremely high-resolution simulations were performed over a small portion of eastern Jasper and western Newton counties in

southeastern Texas. The Strato-NHMASS simulations used a one-way nesting algorithm, starting with an 18-kilometer (km) simulation initialized with NCEP reanalysis data (1°x1°) resolution. Model simulations with horizontal resolutions of 6 km, 2 km, 667 meters, 222 meters, and 71 meters were performed using the one-way nesting algorithm (Fig. 2). All simulations were run using a 162x162 grid, the Kain-Fritch convective parameterization scheme and Lin et al. (1983) microphysics package. The model was run with a TKE PBL option, and the TKE from the model is used in the calculations represented in (1).

The horizontal and vertical grid structures must be of comparable resolution in order to capture the wave in full detail. For this reason, the TKE and EDR calculations are only applied to the 222-meter and 71-meter simulations in the study. The Strato-NHMASS model is run with 90-$\sigma$ levels extending up to 10 millibars. Data from $\sigma$-levels above the 300-millibar level were interpolated into height coordinates with a 250-meter vertical resolution, closely matching the horizontal grid dimensions. The TKE calculations are then performed from the 300-millibar (around 9 kilometer) to 10-millibar (around 21 kilometer) levels.

In addition to the different horizontal resolutions used for the 12 December 2002 case, different Reynolds averaging periods were used. First, the entire duration of the model simulation was averaged, and perturbations were derived from this 1-segment averaged model run simulations. The model output was also averaged in four equally spaced temporal segments (hereafter, 4-segment), which allows for higher frequency modes to be captured when compared to the 1-segment TKE budget.

## 4. RESULTS

### 4.1 12 December 2002 Strato-NHMASS 222-meter Simulation, 1-Segment Budget

The 222-meter simulation was initialized at 2209 UTC 12 December 2002 using the data from the 667-meter simulation. The convection generated by the surface-based gravity wave (shown in Figure 3) was already present in the initial conditions within the first guess field of the 222-meter run. The model time step was 0.07 seconds, and data was output every 54 seconds during the 35 minute, 6 second simulation. As described in Section 3, the entire 35 minute, 6 second model run was averaged, and perturbations calculated using (2). Figure 4 shows a four-panel plot of the u-prime field using the 1-segment averaging technique. In the perturbation fields, the vertically propagating gravity wave is seen amplifying until reaching the 16-18 km level (Fig. 4c) and breaking shortly thereafter (Fig. 4d), between 20 and 25 minutes into the simulation (valid 2230-2236 UTC 12 December 2002). Though not shown in this manuscript, perturbation values from the v and w wind fields also showed a similar wave structure. In addition to the kinematic perturbation field, investigation of the thermodynamic perturbation field (virtual potential temperature) also showed a distinct wave signature. Figure 5 shows a four-panel plot of the $\theta$-v field using the 1-segment averaging technique. Perturbations with a range from –20 to 20 Kelvin (Fig. 5c) suggest that the buoyant production/destruction of TKE play a significance role with the vertically propagating stratospheric wave.

Linear gravity wave theory suggests that the critical level, the level in which the

stratospheric wave would break, would be found where the forward speed of the propagating gravity wave is equal to the local flow speed. Graphical analysis suggests that a forward speed of U = 16 meters per second would roughly correspond to a critical level lying between 16-18 km between 2230-2236 UTC. A power spectrum analysis will be required to find the exact location of the critical level at the time of the wave break, but it is theorized that the critical level will fall within the 16.5-18 km range, consistent with the findings of Lane et al. (2003).

Once the perturbations and time averages were calculated, each individual term in (1) was calculated for the 1-segment averaged data. The first three terms on the right hand side of (1), representing the horizontal and vertical advection of TKE by the mean wind (not shown), was small in comparison to the buoyant production and mechanical shear terms in (1). The most likely explanation for the negligible TKE profile contributions from the advection terms is from the Reynolds averaging technique. High frequency shifts in momentum may have been averaged out, and short-lived TKE gradients may also have been averaged out. This issue will be revisited with the 4-segment TKE budget presented in Section 4.2.

The two most important term contributions to the overall TKE tendency were the buoyant production and mechanical shear. Figure 6a is the 1-segment TKE budget average for the buoyancy production term, the fourth term in (1). A distinct couplet in the buoyancy term is located between the 16-17 km level, very close to the same geographical location in the cross-section showing the breaking stratospheric wave (Fig. 4c). Figure 6b is the 1-segment TKE budget average for mechanical shear, the fifth term in (1). As with Fig. 6a, a distinct couplet in contribution from mechanical shear is found in the 16-17 km level. Contributions from the other terms in (1) (not shown) were not of the same order of magnitude as the buoyancy and mechanical shear term.

### 4.2 12 December 2002 Strato-NHMASS 222-meter Simulation, 4-Segment Budget

To further enhance the Reynolds averaging skill in more accurately resolving temporal features within the event, the averaging time was split into four separate, equally sorted time periods. With model output available every 54 seconds, four separate averaging time periods were used, each lasting 9 minutes each. The time structure of the averaging means that 10 model output times were averaged for each dependent variable, allowing for a fairly representative depiction of the wave during each segment. The patterns depicted in the 4-segment budget perturbation fields show the same wave structure (as in Fig. 4 and Fig, 5) but exhibit a slightly higher-frequency signal than the 1-segment budget. As with the 1-segment budget in Section 4.1, the buoyancy production and mechanical shear terms were dominant in the TKE contribution.

However, the higher frequency temporal averaging did improve the contribution signal from a number of other terms. Figures 7 and 8 show four-panel plots of TKE profile contribution from w-advection (Fig. 7) and buoyancy production (Fig. 8). Other term contributions are not shown due to space limits. Each term shows a similar vertical structure mimicking the vertical wave structure shown in Fig. 4. The highest values of TKE contribution come in the final two averaging periods between 2227-2245 UTC 12 September 2002, after the stratospheric wave has broken. Most of the terms also show a distinct couplet in TKE creation/destruction between the 16-18 km layer, consistent with

the 1-segment averaging shown in Section 4.1. The higher frequency temporal signature given by the 4-segment averaging technique shows promise in depicting the structure of vertically propagating gravity waves through both perturbation and term fields, and locating areas of TKE creation/destruction well into the stratosphere.

### 4.3. 12 December 2002 Strato-NHMASS 71-meter Simulation

The 222-meter simulation discussed in Sections 4.1 and 4.2 was then used to initialize the Strato-NHMASS model to run at a 71-meter vertical resolution, as shown in the domain map in Fig. 1. Using the same methodology outlined previously, the 71-meter simulation was subjected to both Reynolds averaging techniques (1-segment and 4-segment). The 1-segment TKE budget uses an entire model simulation time of 13.5 minutes. The 4-segment TKE budget uses four equally spaced averaging periods that are 2.5 minutes long with model output that was available every 30 seconds.

Unlike the 222-meter simulation, the TKE profile contribution from the first three advective terms was as large as the buoyant production and mechanical shear terms. Figure 9 shows a three-panel plot of TKE contribution from u-mean, v-mean, and w-mean advection terms in (1) for the 71-meter simulation. As with the 222-m 1-segment TKE budget, the same vertical level (16-18 km) and geographical location in the cross-section are identified, but with much higher values. Further analysis of the horizontal and vertical TKE gradients (not shown) identified stronger TKE gradients as the main factor, consistent with the higher model resolution. Figure 10 shows a three-panel plot of TKE contribution from buoyant production, mechanical shear, and turbulent transport. Though contributions from the mechanical shear and turbulent transport terms are not as pronounced as the advection or buoyant production terms, the plots show a higher-frequency signature consistent with smaller waves and perturbations in the 71-meter simulation, and again correspond to the same three-dimensional location discussed in Sections 4.1 and 4.2.

The 4-segment TKE budget graphics for the 71-meter simulation are to be completed for the presentation, but are not shown here. The 4-segment 71-meter simulation had similar quantitative values and vertical structure comparable with the 1-segment results, but with a higher temporal frequency signature, and is consistent with the findings for the 222-meter simulations discussed in Section 4.2.

## 5. CONCLUSIONS AND FUTURE WORK

A Reynolds averaging approach to the TKE tendency equation is applied to a convectively induced vertically propagating gravity wave in the lower and middle stratosphere. Each term in the TKE tendency equation is calculated explicitly for two high-resolution model runs (222-meter and 71-meter) using different averaging techniques and a vertical resolution of 250-meters. The Strato-NHMASS model, with 90 vertical levels and a model lid at 10 millibars, is used to simulate the stratospheric waves. The case used to investigate the formulation is the 12 December 2002 large amplitude gravity wave case described in detail by Suffern et al. (2005).

The two different averaging techniques (1-segment and 4-segment) are done for a 35 minute, 6 second run at a horizontal resolution of 222-meters for the 12 December

2002 case. The perturbation field associated revealed the level of wave-breaking to be between the 16-18 kilometer level 20 minutes into the simulation. Graphical interpretation of the data also suggests that this level and time period is likely also the region of the critical level. The stratospheric wave broke in under the same conditions and in the same manner consistent with the idealized simulations of Lane et al. (2003), though a power spectrum analysis is needed to verify this quantitatively.

The 1-segment 222-meter TKE budget identified the geographical location in three-dimensional space of the breaking wave in the stratosphere through the TKE term contributions; specifically the buoyancy production and mechanical shear terms. The results suggest that buoyancy production and mechanical shear production of turbulence are the most important contributor to TKE profiles on a 35-minute time scale, and are highest in the region of stratospheric wave breaking (or the critical level). The 4-segment 222-meter TKE budget had a much higher temporal frequency than with the 1-segment budget, consistent with the shorter averaging times. As was with the 1-segment budget, the buoyancy production and mechanical shear terms provided the greatest contribution.

The 222-meter simulation was used to initialize another Strato-NHMASS run for the 12 December 2002 case. A horizontal resolution of 71-meters was used to simulate a very small area over Easter Jasper and Western Newton County in southeast Texas. The model run was subjected to both the 1-segment and 4-segment TKE budget approach. The 1-segment TKE budget revealed non-negligible TKE contributions from the advection terms and a much stronger TKE signal in general. Investigation of the TKE gradients within the 71-meter simulation showed much stronger gradients, implying that the model grid resolution is an important factor in determining term contributions. For a very small temporal and spatial scale, the authors hypothesize that contributions from the advection terms in the TKE tendency equation are non-negligible, and must be taken into consideration depending on the scale of the event. Though not shown in the manuscript, EDR profiles have been computed for a few simulations, and will be incorporated into an automated nesting algorithm that will use the EDR values calculated from the TKE tendency equation rather than from the parameterizations built in to the model.

The convectively induced vertically propagating gravity wave from the 12 December 2002 shows turbulence characteristics similar to classical orgraphically-induced gravity waves that have been studied in great detail. Because the time scales in the model simulations are short, the convective updraft is, for all practical purposes, quasi-stationary. The possibility exists that one can treat the updraft as a quasi-stationary, diabatic "mountain," with the same wave generation and turbulence profiles as that of a true orographic feature. Future study includes an identical analysis for a vertically propagating gravity wave induced by a true mountain and comparison to other modes of convection.

## 6. ACKNOWLEDGMENTS

This research was supported under U.S. Air Force contract FA8718-04-C-0011. The main author wishes to thank Dr. Michael Brennan, Michael Kiefer, Zachary Brown and Chris Hill for their helpful input, and Nicole Haglund and Emily Lunde for helpful manuscript suggestions.

## 7. REFERENCES


Kiefer, M.T., 2005: The Impact of Superimposed Synoptic to Meso-Gamma Scale Motions on Extreme Snowfall over western Maryland and northeast West Virginia during the 2003 President's Day winter storm. MS thesis, Dept. of Marine, Earth, and Atmospheric Sciences, North Carolina State University, 204 pp.

Lane, Todd P., Sharman, Robert D., Clark, Terry L., Hsu, Hsiao-Ming, 2003: An Investigation of Turbulence Generation Mechanisms above Deep Convection. *J. Atmos. Sci.,* 60, 1297-1321.

Leutbecher, Martin and Hans Volkert. 2000: The Propagation of Mountain Waves into the Stratosphere: Quantitative Evaluation of Three-Dimensional Simulations. *J. Atmos. Sci.*: 57, 3090–3108.

Lilly, D.K. and Peter F. Lester. 1974: Waves and Turbulence in the Stratosphere. *J. Atmos. Sci.*: 31, 800–812.

Stull, Roland B., 1988: *An Introduction to Boundary Layer Meteorology*. Kluwer Academic Press: 639 pp.

Suffern, P.S., 2005: Numerical Simulations of Vertically Propagating Gravity Waves in the Stratosphere Above a Hydrostatic Large Amplitude Surface Gravity Wave on December 12th, 2002. *11th Conference on Mesoscale Processes,* Albuquerque, NM, Amer. Meteor. Soc., TBD.

Yamada, Tetsuji and George Mellor. 1975: A Simulation of the Wangara Atmospheric Boundary Layer Data. *J. Atmos. Sci.*, 32, 2309–2329.

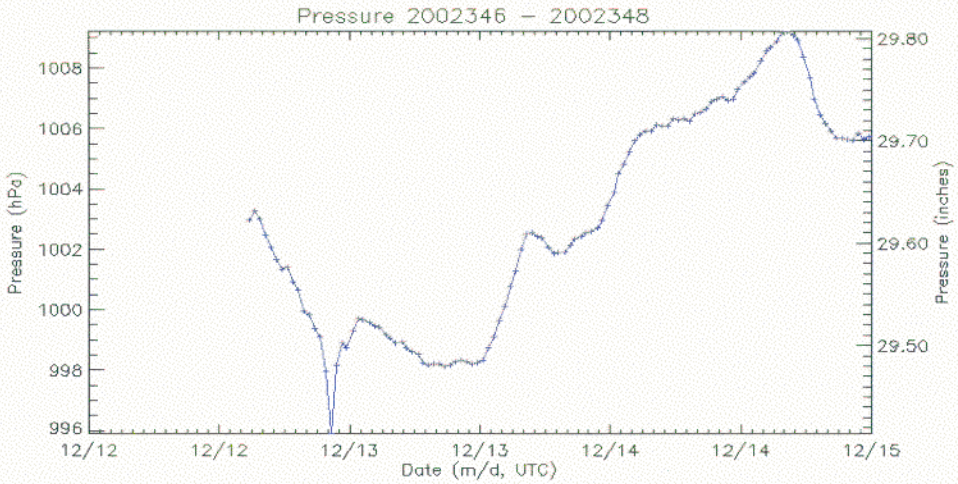


Figure 1. GPS mean sea level pressure (mb) from Palestine, Texas valid from 12/0100 UTC – 15/0000 UTC December 2002.

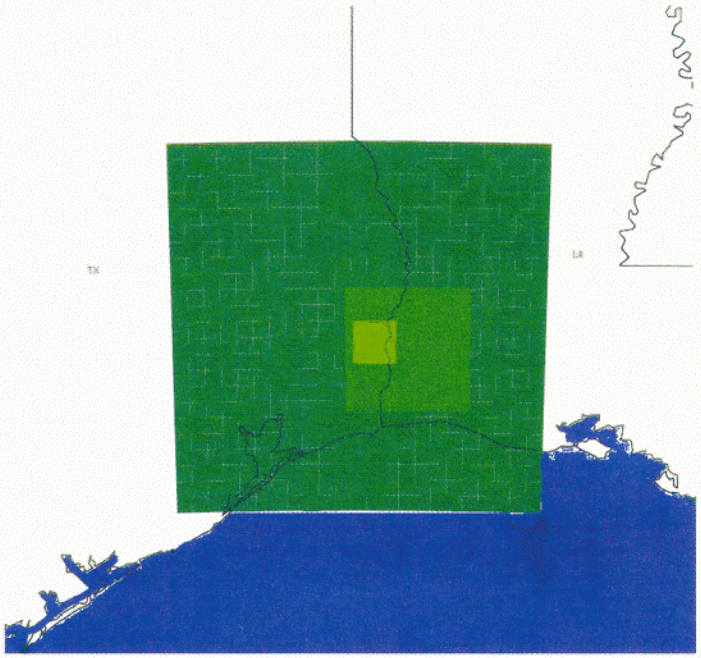

Figure 2. Domain locations for 6kn, 2 km, 667m, 222m, and 71m 12 December 2002 Strato-NHMASS Simulations.

Figure 3. 222m Strato NH-MASS Sea level pressure (white contours) and surface winds (green barbs) valid ~2230 UTC 12 December 2002.

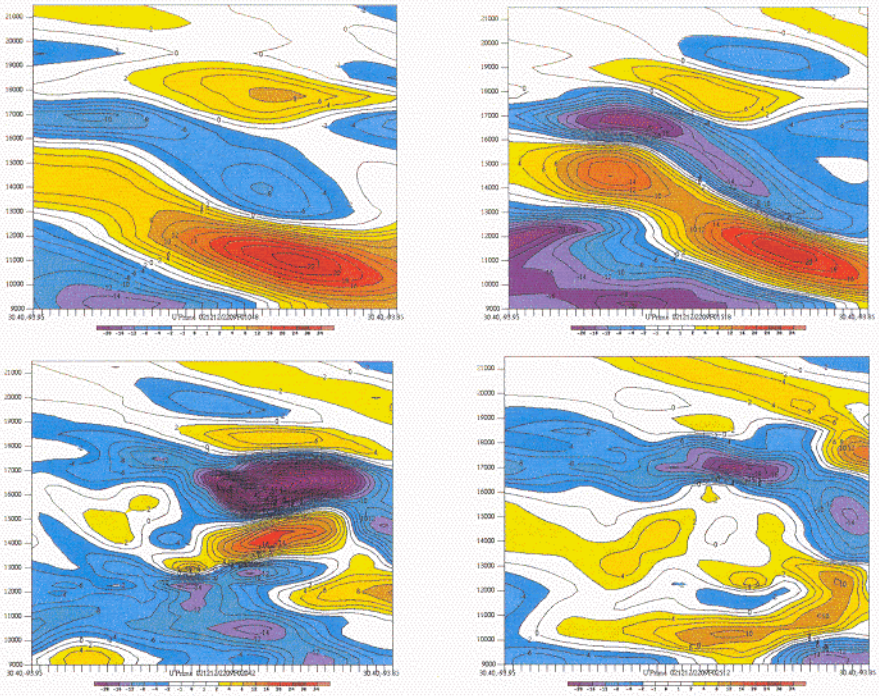

Figure 4. Strato-NHMASS 222m 12 December 2002 U-prime perturbation field at approximately (a) 2219 UTC (b) 2224 UTC (c) 2229 UTC (d) 2234 UTC. Perturbation flow is color filled and contoured in knots.

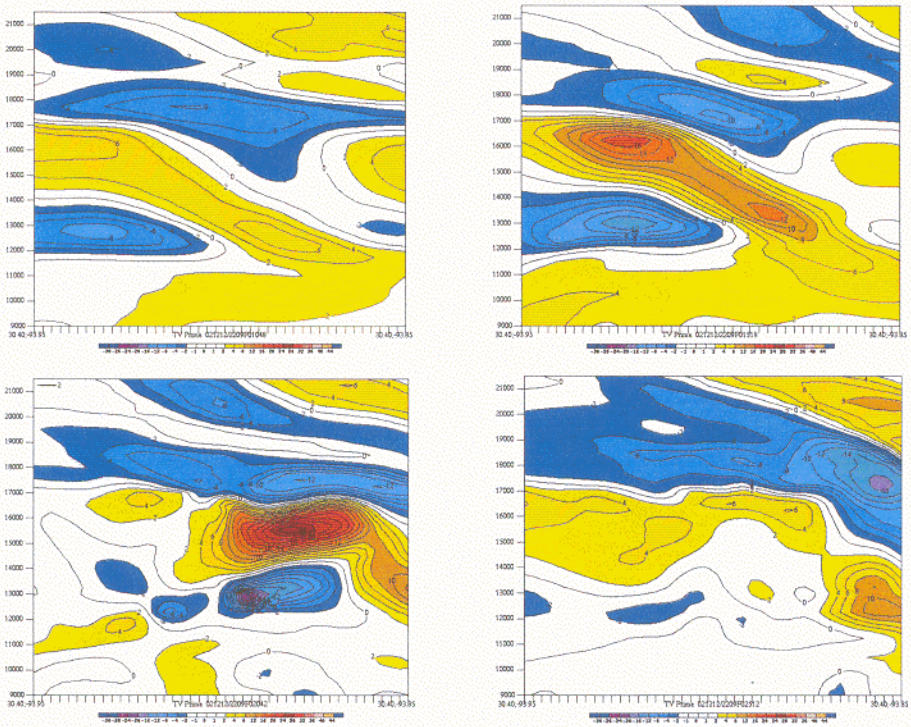

Figure 5. Strato-NHMASS 222m 12 December 2002 virtual potential temperature perturbation field at approximately (a) 2219 UTC (b) 2224 UTC (c) 2229 UTC (d) 2234 UTC. Perturbation flow is color filled and contoured in Kelvin.

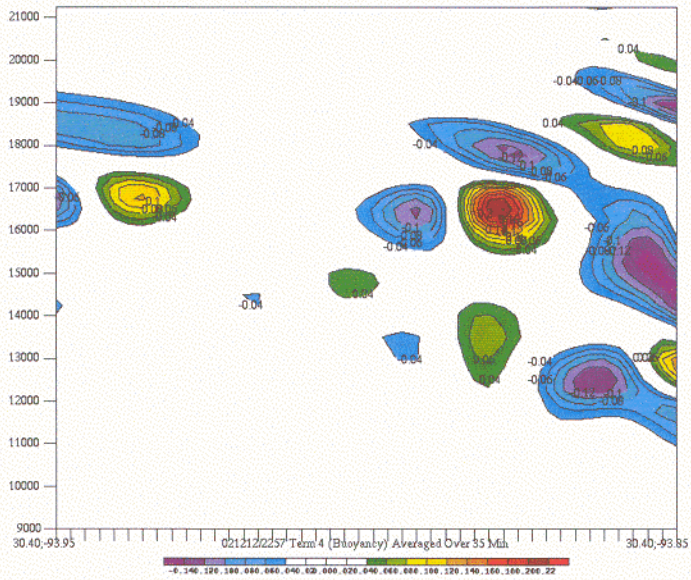


Figure 6. Strato-NHMASS 222m 12 December 2002 1-segment TKE budget showing contribution from Term 4: Buoyant Production (m^2/s^3), averaged over the 35-min model run initialized at 2209 UTC 12 December 2002. The left axis is height in meters. The area of concern is between 16-18 km in the east-central portion of the cross section, where the stratospheric wave breaks. Warm colors correspond to positive contributions, and cool colors correspond to negative contributions.

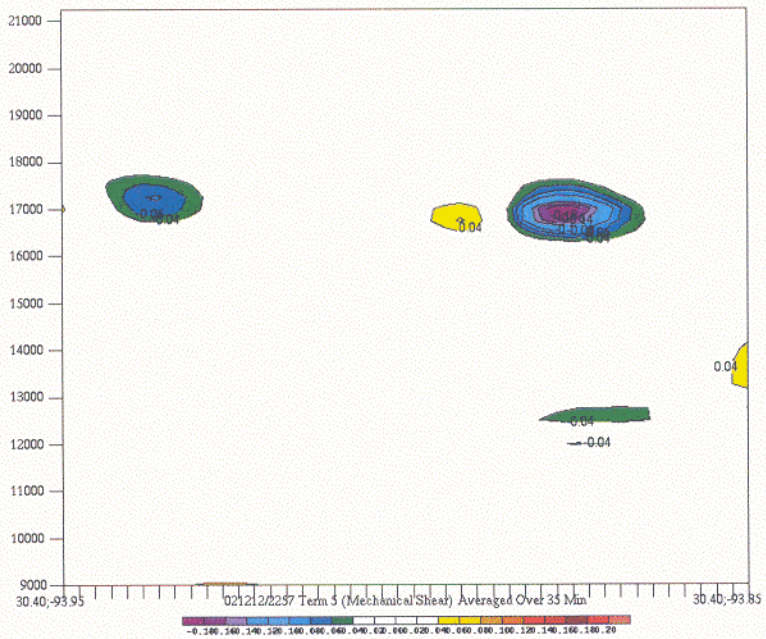


Figure 7. As with Fig. 6, but for Term 5: Mechanical Shear (m^2/s^3).

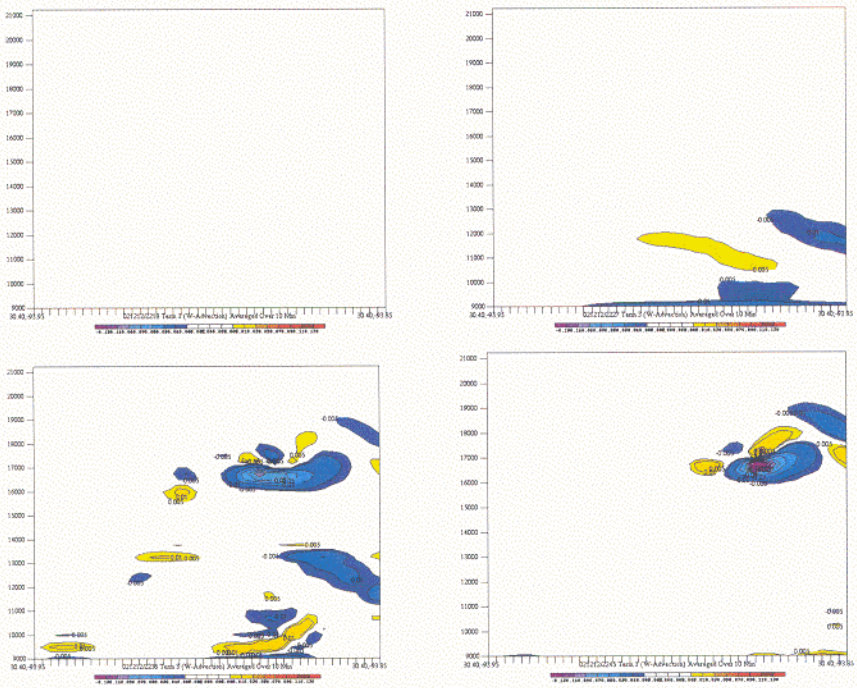

Figure 8. Strato-NHMASS 222m 12 December 2002 4-segment TKE budget showing the evolution of Term 3: W-Advection (m^2/s^3) at approximately (a) 2219 UTC (b) 2224 UTC (c) 2229 UTC (d) 2234 UTC.

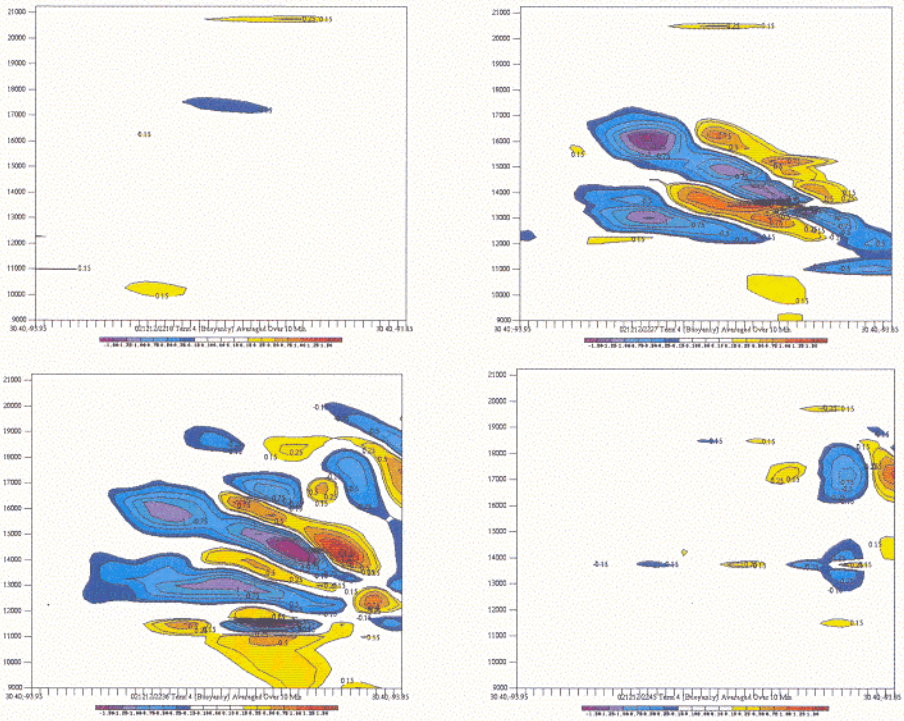

Figure 9. Strato-NHMASS 222m 12 December 2002 4-segment TKE budget showing the evolution of Term 4: Buoyant Production (m^2/s^3) at approximately (a) 2219 UTC (b) 2224 UTC (c) 2229 UTC (d) 2234 UTC.

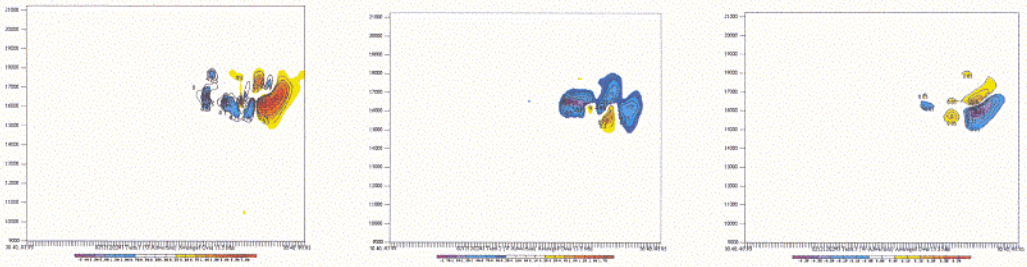

Figure 10. Strato-NHMASS 71m 12 December 2002 1-segment TKE budget showing the evolution of (a) Term 1: U-Advection; (b) Term 2: V-Advection; (c) Term 3: W-Advection. All units are m^2/s^3 and averaged over the 10.5 minute simulation initialized at 2230 UTC 12 December 2002.

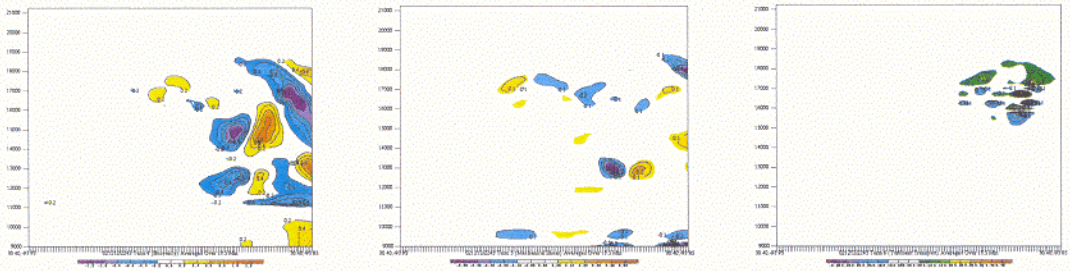

Figure 11. As with Fig. 10, but for (a) Term 4: Buoyant Production; (b) Term 5: Mechanical Shear; (c) Term 6: Turbulent Transport.

## Appendix C

# NUMERICAL SIMULATIONS OF VERTICALLY PROPAGATING GRAVITY WAVES IN THE STRATOSPHERE ABOVE A HYDROSTATIC LARGE AMPLITUDE SURFACE GRAVITY WAVE ON DECEMBER 12$^{TH}$, 2002

Paul Samuel Suffern[1], Yuh-Lang Lin[1], and Michael L. Kaplan[2]
[1]North Carolina State University, Raleigh, North Carolina
[2]Desert Research Institute, Reno, Nevada

## 1. INTRODUCTION

Gravity waves occur frequently throughout the atmosphere, but due to their nature they are hard to find, track, and predict unless we are fortunate enough that a gravity wave forms and moves over our existing data collection sites. Because of this, our understanding of gravity waves still leaves much to be desired. Gravity waves have been shown to redistribute energy and momentum (e.g., Rauber et al. 2001), initiate and propagate along with convection (e.g., Zhang et al. 2003), and be a significant factor leading to clear air turbulence (e.g., Lane et al. 2003). Mesoscale gravity wave generation mechanisms have to shown to be associated with jet streaks (Zhang 2004 and references therein), orography (e.g. Clark et al. 2000), and convection (Lane et al. 2003 and references therein). This paper will be focusing on the environment favorable for stratospheric gravity waves formed above and around moist convection.

On December 12, 2002, a strong upper-level trough dug southward into central Texas and intersected with a strong sub-tropical jet streak over Mexico. The favorable interaction between these two systems allowed for convection to occur along the eastern coast of Texas and the western Gulf of Mexico. As the day progressed the upper-level trough became more negatively tilted, the convection increased in intensity and coverage, and a surface low pressure center formed below the max divergence aloft in the left exit region of the sub-tropical jet. An outflow jet began to form later in the day associated with and downstream of the convection, which had now organized itself into a squall line. However, part of this deep convection had formed north of a warm frontal boundary, above a good duct, and near a jet streak, which is a favorable location for a mesoscale gravity wave to form (Uccellini and Koch 1987). A model based study of the effects this convection has on the downstream environment as it relates to the modeled stratospheric gravity waves above the large amplitude tropospheric gravity wave will be explored in this paper.

## 2. MODEL

The one-way nested stratospheric version of the non-hydrostatic mesoscale atmospheric simulation system (NHMASS) model was used to simulate this mesoscale gravity wave event at horizontal grid spacing of 18 km, 6 km, and 2 km. The 18 km horizontal grid spacing simulation was initialized using NCEP reanalysis at 0000 UTC 12 December 2002. Nested domains of 6 km and 2 km were initialized at 0800 UTC and 1900 UTC 12 December 2002, respectively. All model runs had 90 vertical levels and

are similar to Kiefer (2005) setup of the NHMASS model, except for the 2 km horizontal grid spacing simulation, which was run with the convective parameterization scheme turned off. A sensitivity study was also done with a model simulation using no latent heating, to see the importance that latent heating had on development and environment for the large-amplitude gravity waves. The model lid was extended to 30 km in an effort to focus on vertically propagating stratospheric gravity waves. Only the results from the 6 km and 2 km simulations will be shown in this paper.

## 3. RESULTS AND DISCUSSION

The 6 km model simulation begins to form the convective outflow jet at 300 hPa over north central Texas by 1600 UTC 12 December 2002 (Fig. 1a) in which eastern Texas and the Texas/Louisiana border are in the right entrance region of the outflow jet, a favorable region for upper divergence. While this is occurring a residual component of the strong sub-tropical jet is advecting eastward into southern Texas and another momentum maximum is over Louisiana once again putting eastern Texas into a favorable region of upper divergence at 200 hPa (Fig. 1b). Figure 2 shows the 30-minute output of total precipitation associated with the convection and upper divergence at 1600 UTC and while there is some precipitation located across eastern Texas and the western Gulf of Mexico is not very impressive. With this convection a surface low-pressure center of 1008 hPa has formed at it is located off the coast of southern Texas (not shown). By 2000 UTC on December 12, 2002, the convection has formed into a squall line northeast of Houston, Texas (HOU) (Fig. 3a) and the surface low-pressure center has dropped to 1005 hPa (Fig. 3b) with mesoscale gravity waves becoming evident north of the surface low-pressure center. Also, aloft at 200 hPa a mesoscale outflow jet becomes visible north and northeast of the convection (not shown), while the trough at 300 hPa becomes more negatively tilted (Fig. 4). At 2200 UTC the surface low-pressure center is at the Texas/Louisiana border region with more amplified mesoscale gravity waves to its north (Fig. 5). So it is apparent that a large-amplitude surface gravity wave has formed associated with this jet/front system and convection, which compares favorably to observations (not shown), however, the rest of this paper will focus on the modeled stratospheric gravity waves that form above and around the moist convection associated with the lower tropospheric gravity waves.

At 2200 UTC 12 December 2002, the 2 km NHMASS model simulates the convection very similar to the 6 km simulation with the main part of the squall line in eastern Texas (Fig. 6a) and the surface low-pressure center and mesoscale gravity waves along the border of Texas and Louisiana (Fig. 6b). While the convection continues to propagate to the northeast modeled stratospheric gravity waves are beginning to form above and around the moist convection. Between 2200 UTC and 2300 UTC at 100 hPa these modeled stratospheric gravity waves are clearly visible behind the convection forming a wave packet (Figs. 7a and 7b). Figure 8a shows a vertical cross section taken orthogonal to the modeled stratospheric gravity waves with the main jet streak between 200 hPa and 100 hPa and the waves above 100 hPa at 2200 UTC. As the squall line grows stronger and individual convective tops push higher into the stratosphere (not shown), the convection begins to split the momentum of the once continuous jet streak by 2215 UTC (Fig. 8b). At 2230 UTC the split of in the jet streak momentum between 200

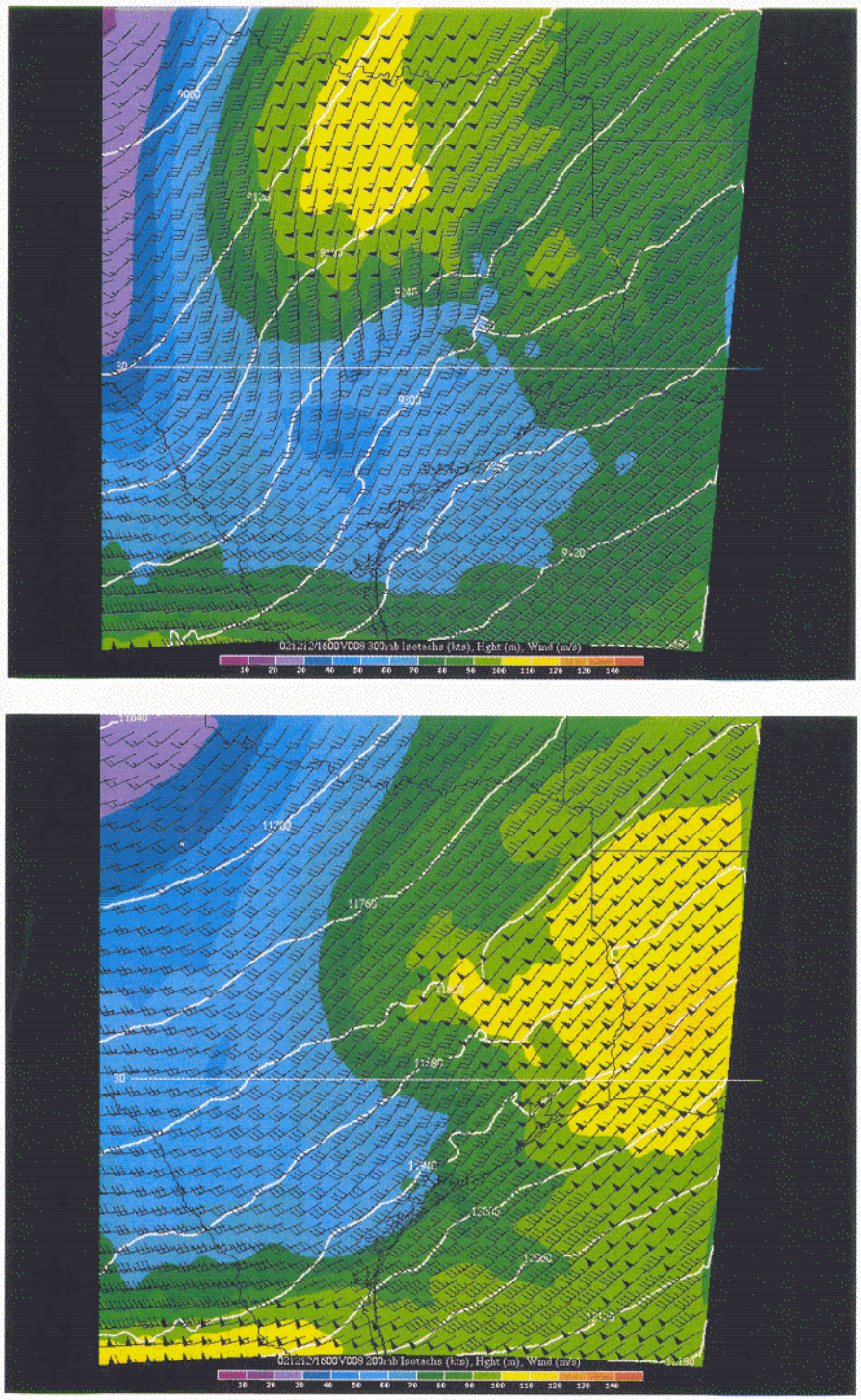


Fig. 1. 6 km NHMASS model 1600 UTC 12 December 2002 isotachs (kts) (colors), geopotential height (m), and wind barbs (m/s) at (a) 300 hPa (b) 200 hPa.

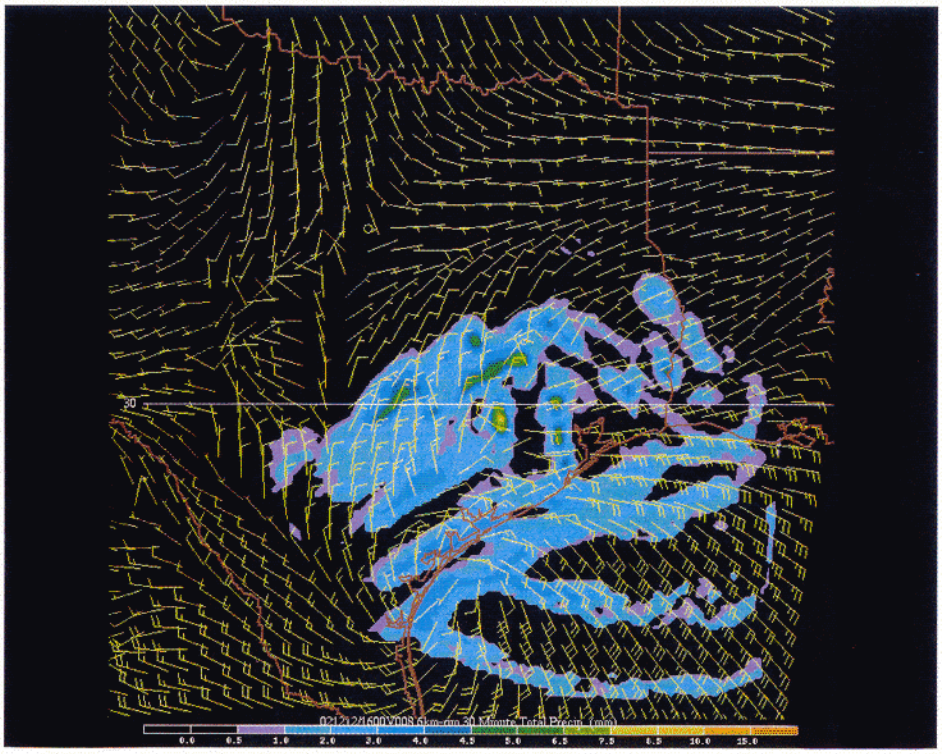


Fig. 2. 6 km NHMASS model 1600 UTC 12 December 2002 total precipitation over the past 30 minutes (mm) and surface winds (kts).

hPa and 100 hPa is even more evident (Fig. 8c), and as a result this momentum is being transferred above the blocking, that is the convective tops, and the momentum is causing the stratosphere to become more perturbed. This perturbation is evident by the growth in amplitude of the modeled stratospheric gravity waves between 2215 UTC (Fig. 8b) and 2230 UTC (Fig. 8c). One of the modeled stratospheric gravity waves has a large increase in amplitude by 2245 UTC (Fig. 8d) as one of the convective tops grows above 200 hPa (not shown) and the momentum from the jet streak blocked by this convective top needs to be dissipated into the surrounding environment. Finally, at 2300 UTC the modeled stratospheric gravity waves vertically propagate all the way to 50 hPa (Fig. 8e) as the momentum from the jet streak moves around and above the convective tops.

Another way to look at how the modeled stratospheric gravity waves propagate vertically away from the convective tops as the momentum from the jet streak is blocked, is by looking at where the Richardson number is below the critical value of 0.25. Where the Richardson number is below critical will provide a corridor where the blocked momentum can be vertical dispersed. At 2200 UTC along the same cross section when the Richardson number is plotted there is no where along the cross section where the number is below critical, therefore we should expect the modeled stratospheric gravity waves to dissipate quickly if they form at all (Fig. 9a)). However, starting at 2215 UTC there begins to be areas where the Richardson number has gone below its critical value

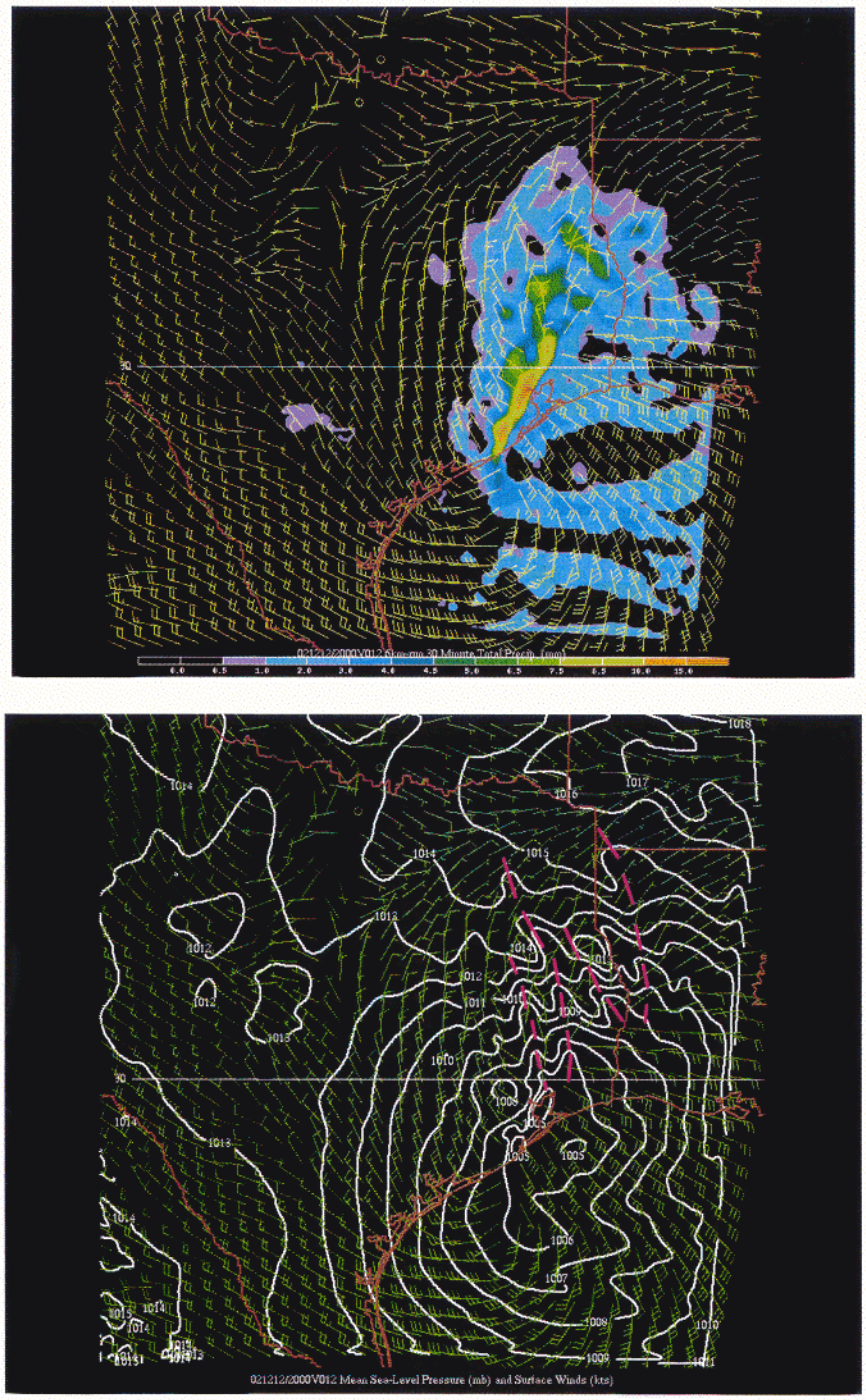


Fig. 3. 6 km NHMASS model 2000 UTC 12 December 2002 (a) total precipitation over the past 30 minutes (mm) and surface winds (kts) and (b) mean sea-level pressure (mb) and surface winds (kts).

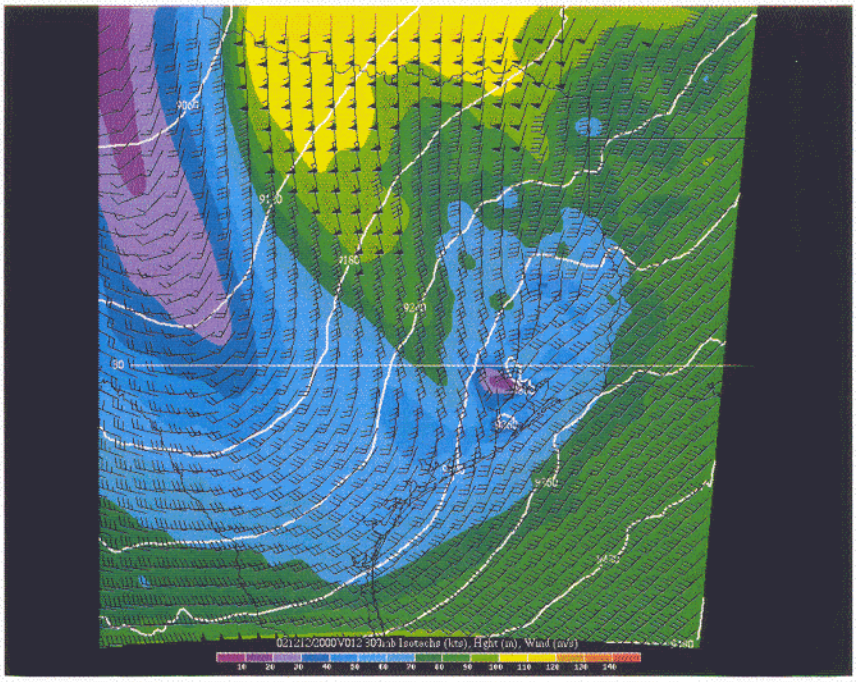

Fig. 4. 6 km NHMASS model 2000 UTC 12 December 2002 isotachs (kts) (colors), geopotential height (m), and wind barbs (m/s) at 300 hPa.

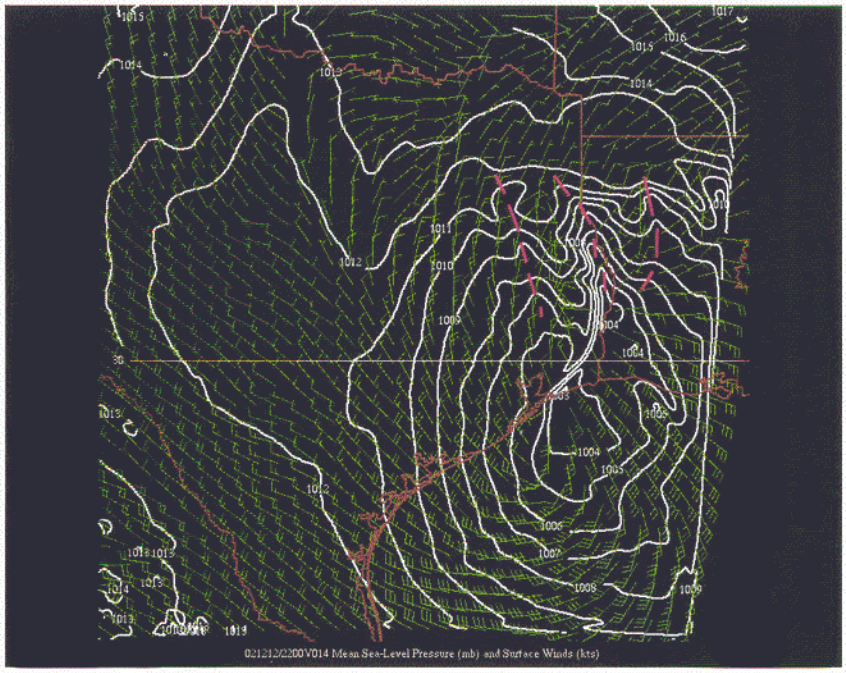


Fig. 5. 6 km NHMASS model 2200 UTC 12 December 2002 mean sea-level pressure (mb) and surface winds (kts).

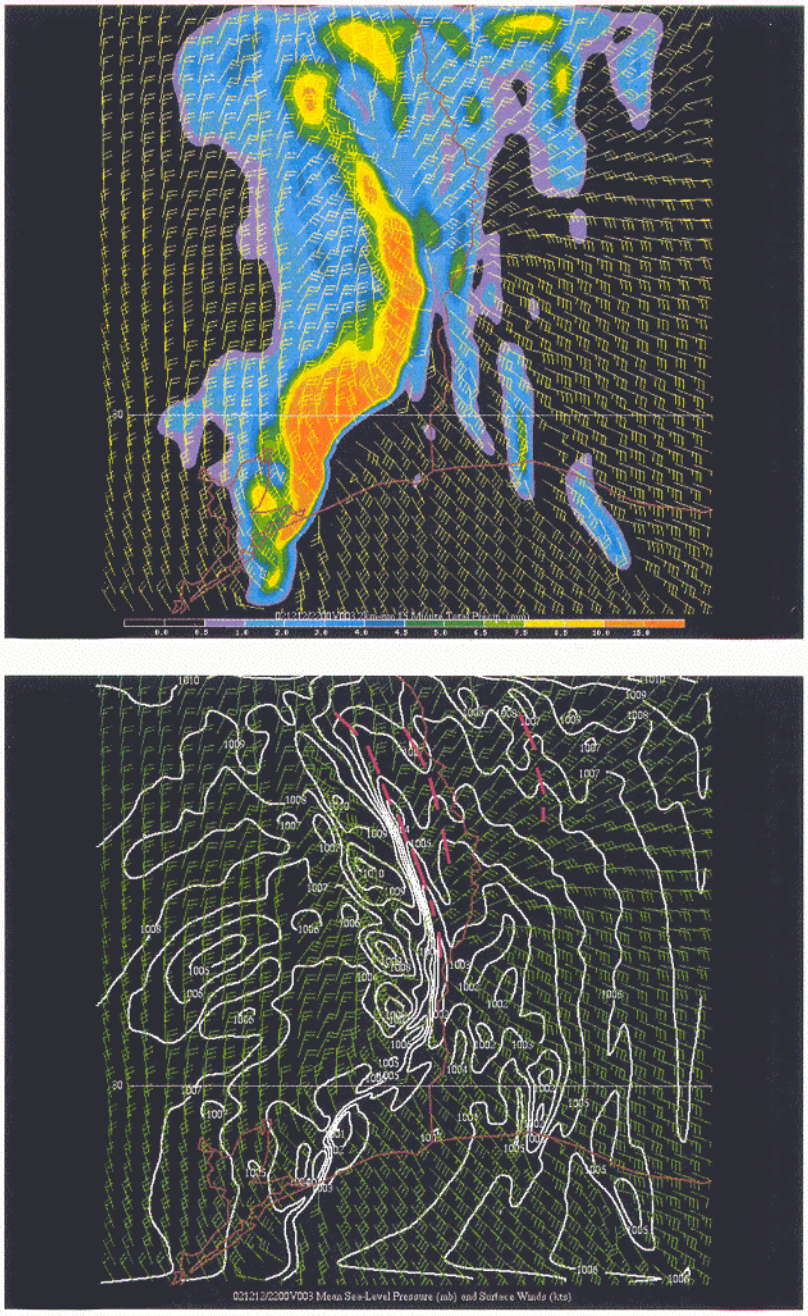


Fig. 6. 2 km NHMASS model 2200 UTC 12 December 2002 (a) total precipitation over the past 15 minutes (mm) and surface winds (kts) and (b) mean sea-level pressure (mb) and surface winds (kts).

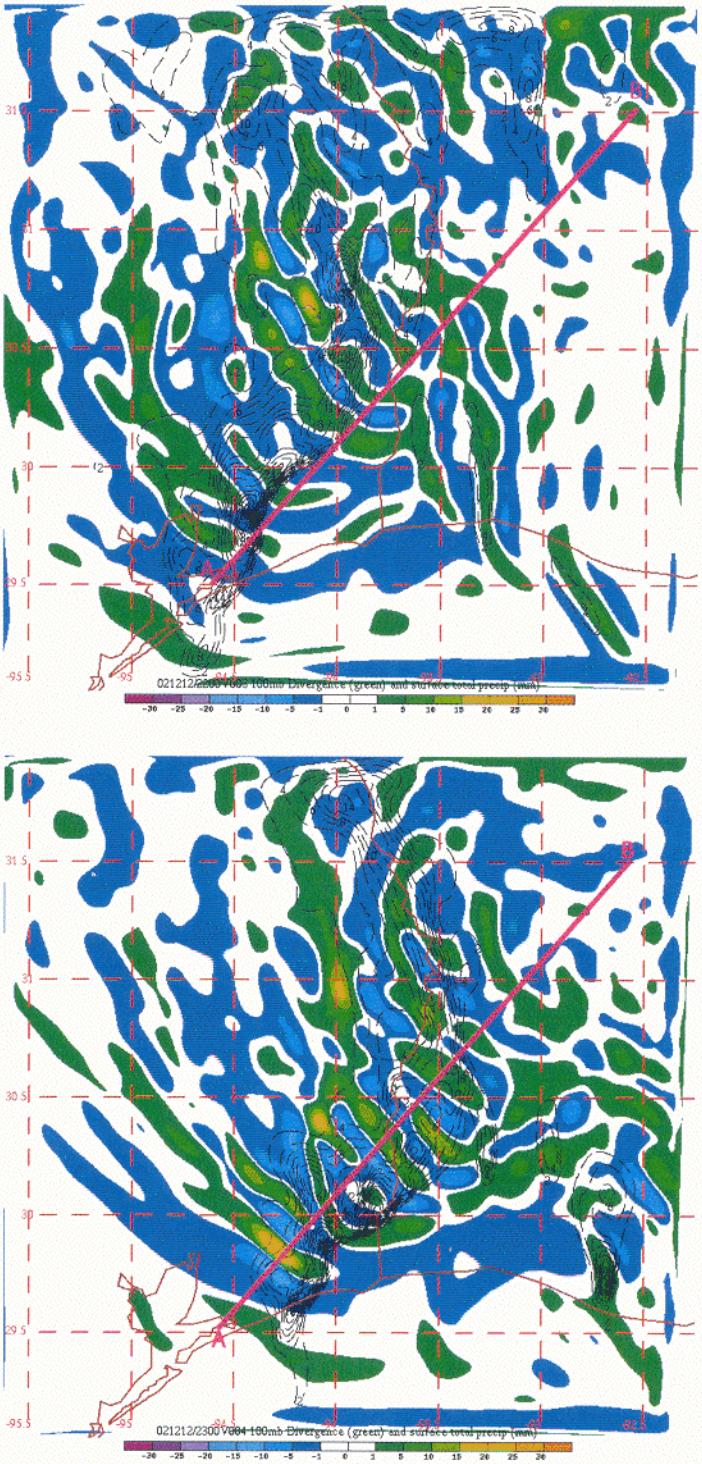


Fig. 7. 2 km NHMASS model 12 December 2002 100 hPa divergence ($1x10^{-4}$ $s^{-1}$) (green), convergence (blue) ($1x10^{-4}$ $s^{-1}$), and total surface precipitation (mm) over the past 15 minutes (dashed) at (a) 2200 UTC and (b) 2300 UTC.

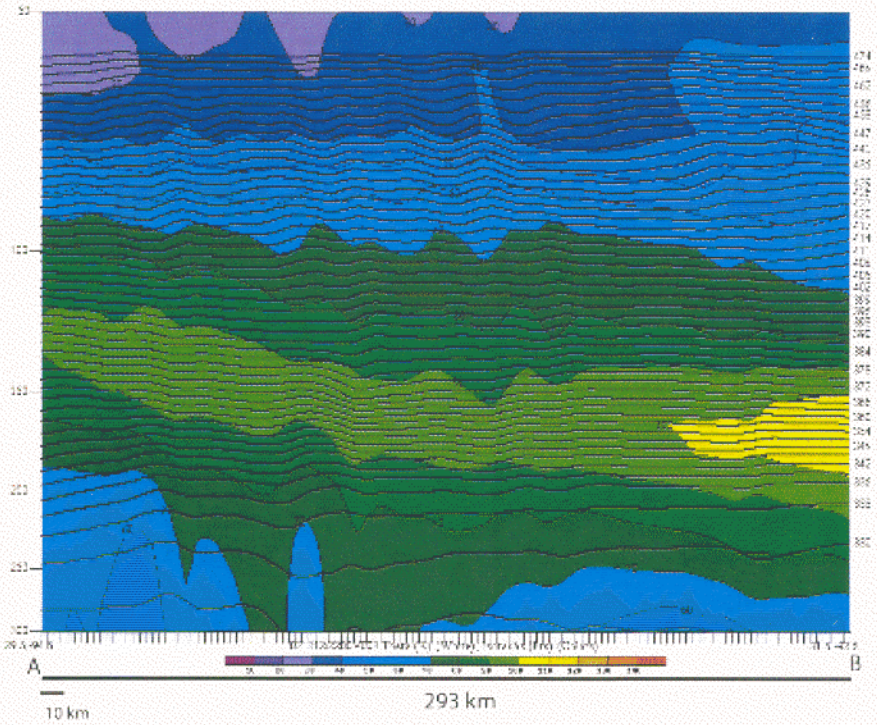


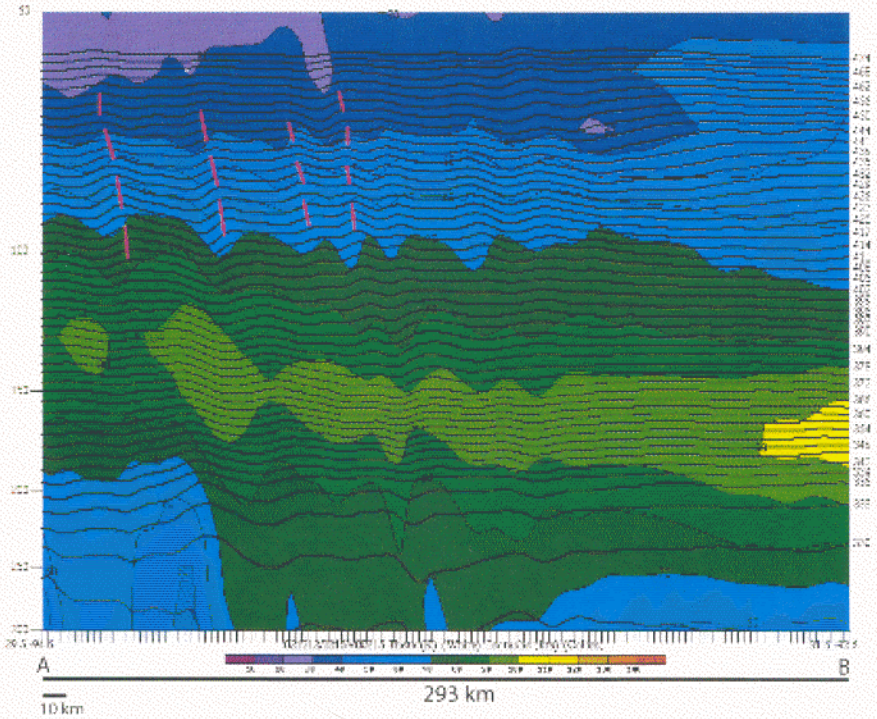


Fig. 8. 2 km NHMASS model 12 December 2002 vertical cross section from 300 hPa to 50 hPa along line A-B (see Figs. 7a and b) of isotachs (kts) (colors) and potential temperature (K) (black lines) at (a) 2200 UTC, (b) 2215 UTC, (c) 2230 UTC, (d) 2245 UTC, and (e) 2300 UTC (Continued next page).

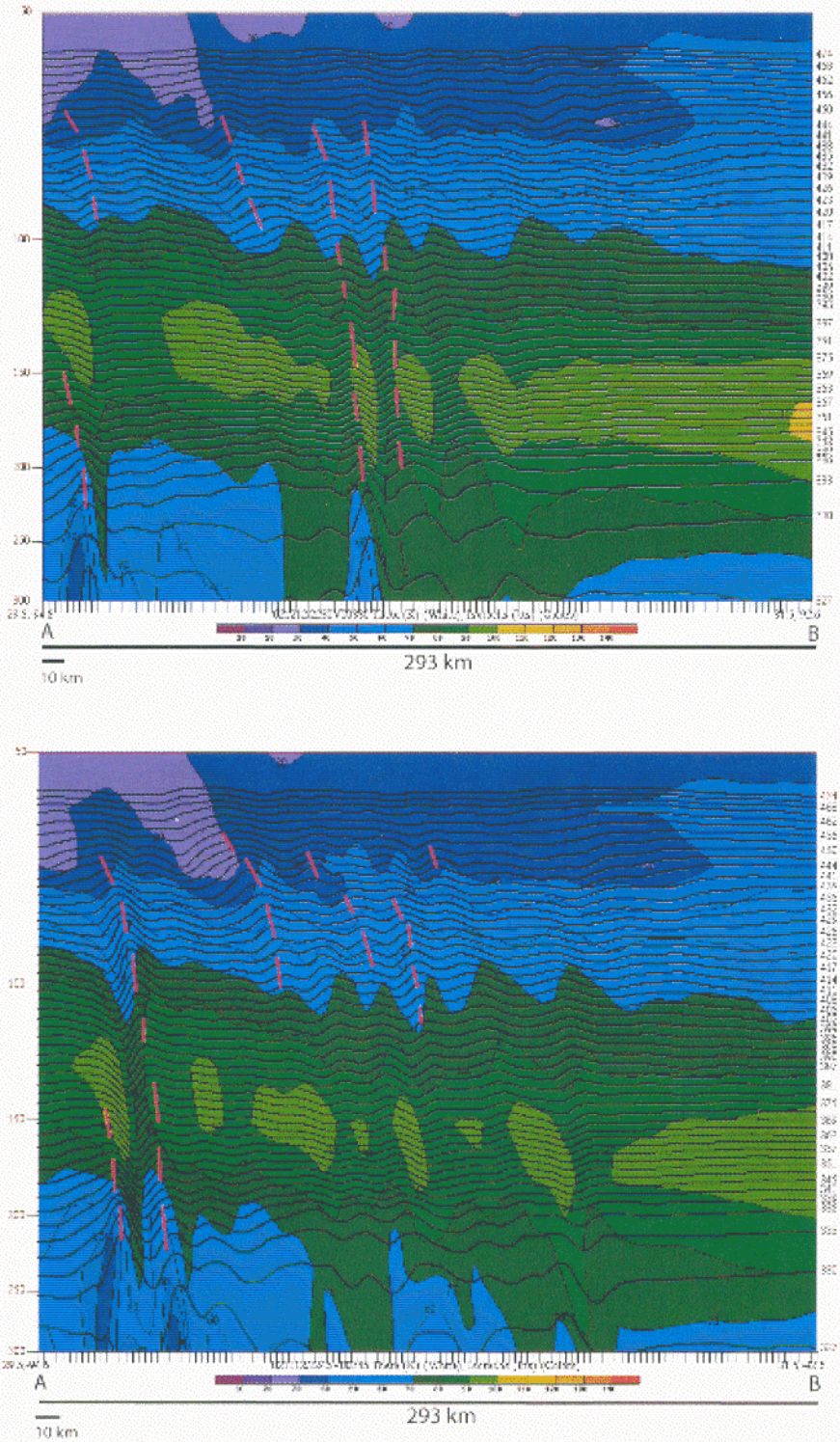


Fig. 8. 2 km NHMASS model 12 December 2002 vertical cross section from 300 hPa to 50 hPa along line A-B (see Figs. 7a and b) of isotachs (kts) (colors) and potential temperature (K) (black lines) at (a) 2200 UTC, (b) 2215 UTC, (c) 2230 UTC, (d) 2245 UTC, and (e) 2300 UTC (Continued next page).

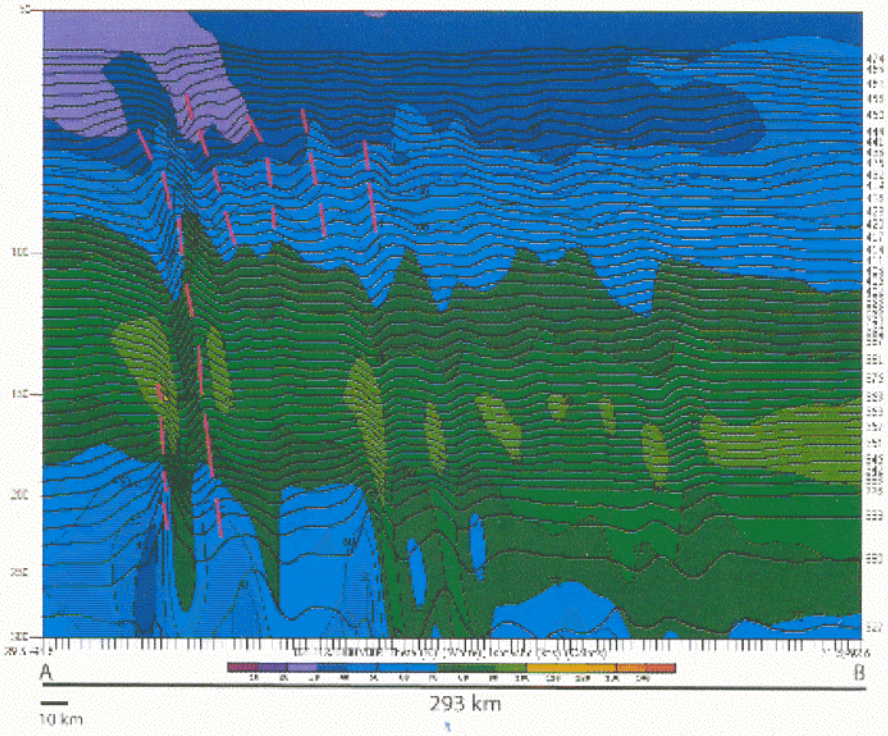


Fig. 8 (Cont'd). 2 km NHMASS model 12 December 2002 vertical cross section from 300 hPa to 50 hPa along line A-B (see Figs. 7a and b) of isotachs (kts) (colors) and potential temperature (K) (black lines) at (a) 2200 UTC, (b) 2215 UTC, (c) 2230 UTC, (d) 2245 UTC, and (e) 2300 UTC).

above and around the convective tops (Fig. 9b). By 2245 UTC (Fig. 9c), Richardson numbers below the critical value of 0.25 are right below the largely amplifying modeled stratospheric gravity wave, and this is indicating the momentum from the blocked jet streak is being vertically propagated and tilted into the lower stratosphere. Consequently, at 2300 UTC the low Richardson number values remain below the large modeled stratospheric gravity wave (Fig. 9d) which allows the modeled stratospheric gravity wave to continue to be reinforced with more momentum and allowing the waves to propagate further, rather than being quickly dissipated into the background environment.

Consistent with these modeled stratospheric gravity waves and the convective outflow jet are several sources of observations. Coarse resolution raob data observed at 0000 UTC 13 December 2005 shows the outflow jet over Oklahoma at 300 hPa (Fig 10a), while at 200 hPa the favorable region for upper divergence is along the Texas/Louisiana border region (Fig 10b). So the large amount of momentum seen between 200 hPa and 100 hPa along the vertical cross section of the modeled atmosphere is consistent with the observations. Observations at 150 hPa (Fig 10c) show stronger momentum over the Louisiana area then at 300 hPa, which is similar to the model results as well. Along with the raob observations are several wind profiler sites, which we are fortunate enough that the gravity waves passes over. At the Ledbetter, Texas wind profiler a strong jet streak is observed pass over the area between 1330 UTC and 1800 UTC on December 12, 2002 (Fig 11a). Notice above 13 km (170 hPa) during this time

the change in vertical wind shear above the jet core is similar to the model vertical cross sections (Figs 8a-8e). Another interesting feature is the momentum mixing vertically after the jet core passes over Ledbetter, TX (Fig 11a). Some of this momentum mixes vertically up to 16km (95 hPa), while another surge mixes down to 6 km (490 hPa), between 1800 UTC and 2200 UTC 12 December 2002 (Fig 11a). The momentum that mixes downward is similar to Rauber et al. (2001). This pattern can again be seen at Winnfield, Louisiana (Fig 11b), when the main jet core passes over, the momentum once is mixed vertically between 2300 UTC on December 12, 2002, and 0300 UTC on December 13, 2002. The Okolona, Mississippi wind profiler also shows this pattern (not shown) of momentum being vertically mixed/displaced. While these wind profiler observations shown have been taken every hour, study and analysis on six-minute wind profiler data is in process.

Sensitivities studies have been run on this large amplitude gravity wave event as well to see the importance of the latent heating on the process and environment for these waves, in both the troposphere and stratosphere. A no-latent heat model simulation was made to compare to the full physics run. Figure 12 shows the sea-level pressure at 2215 UTC for comparison with figure 6b, and the no-latent heat simulation produces no convection, no strong upper-level divergence, and no latent heating, therefore there are no strong pressure falls at the surface. No tropospheric or stratospheric gravity waves occur in the no-latent heat simulation, and the surface-low pressure center passes through Louisiana six to seven slower than the full physics run, while its magnitude is also 9-mb lower (not shown).

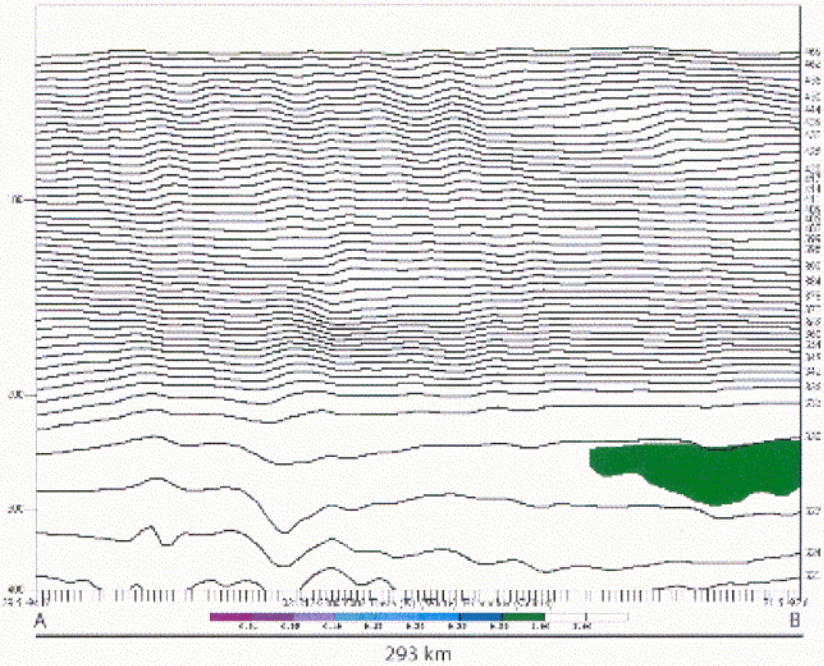


Fig. 9. 2 km NHMASS model 12 December 2002 vertical cross section from 300 hPa to 50 hPa along line A-B (see Figs. 7a and b) of Richardson number (colors) and potential temperature (K) (black lines) at (a) 2200 UTC, (b) 2215 UTC, 2245 UTC, and (d) 2300 UTC (Continued next page).

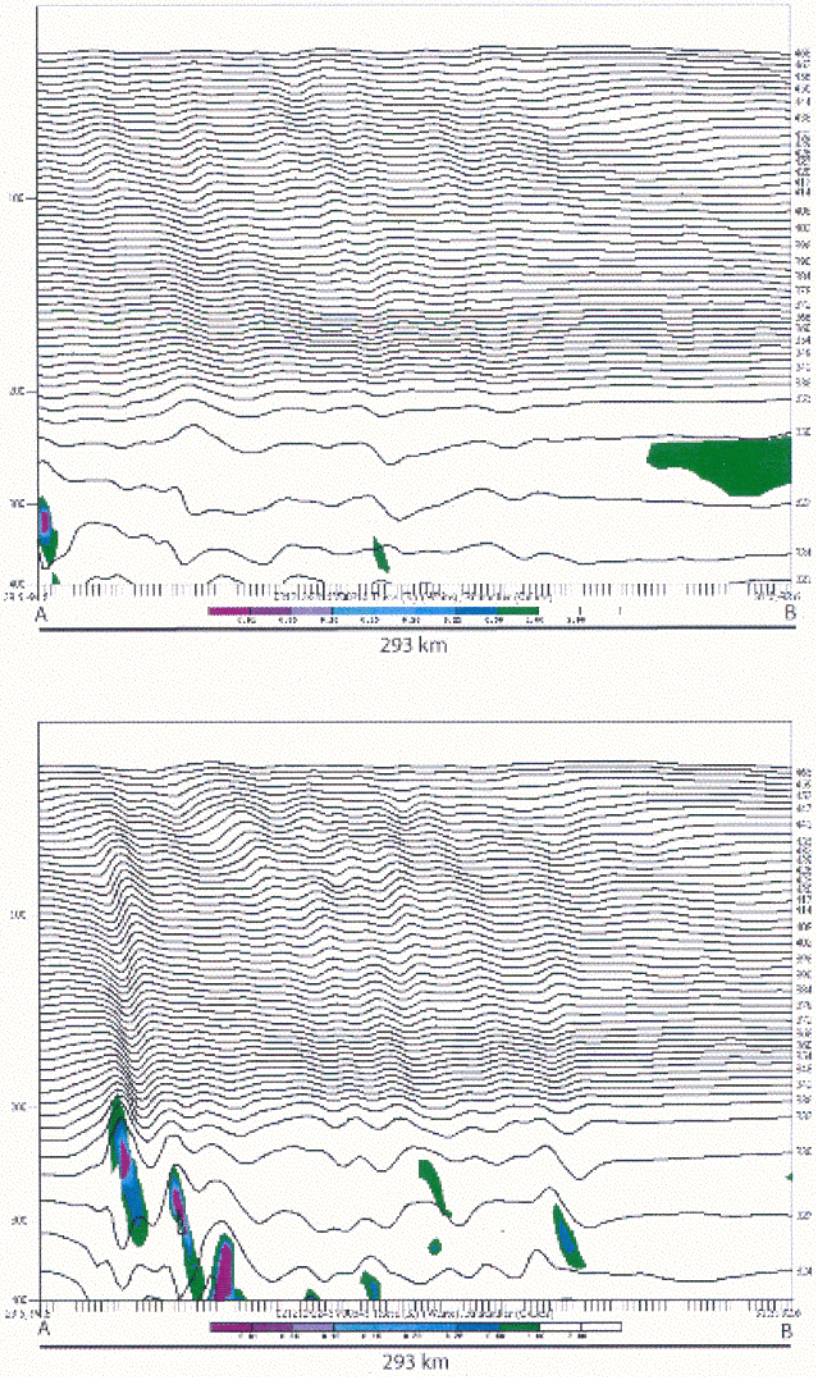


Fig. 9. 2 km NHMASS model 12 December 2002 vertical cross section from 300 hPa to 50 hPa along line A-B (see Figs. 7a and b) of Richardson number (colors) and potential temperature (K) (black lines) at (a) 2200 UTC, (b) 2215 UTC, 2245 UTC, and (d) 2300 UTC (Continued next page).

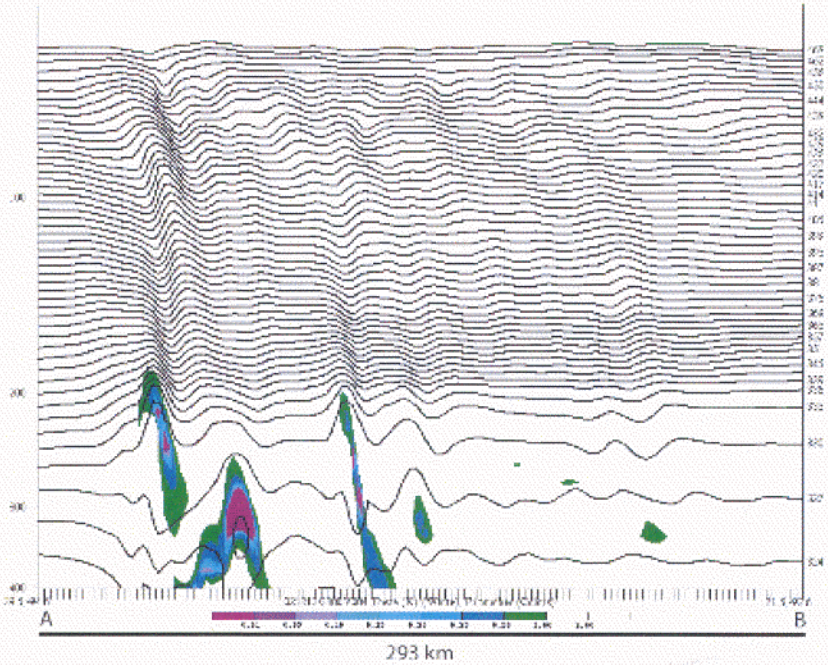


Fig. 9 (Cont'd). 2 km NHMASS model 12 December 2002 vertical cross section from 300 hPa to 50 hPa along line A-B (see Figs. 7a and b) of Richardson number (colors) and potential temperature (K) (black lines) at (a) 2200 UTC, (b) 2215 UTC, 2245 UTC, and (d) 2300 UTC.

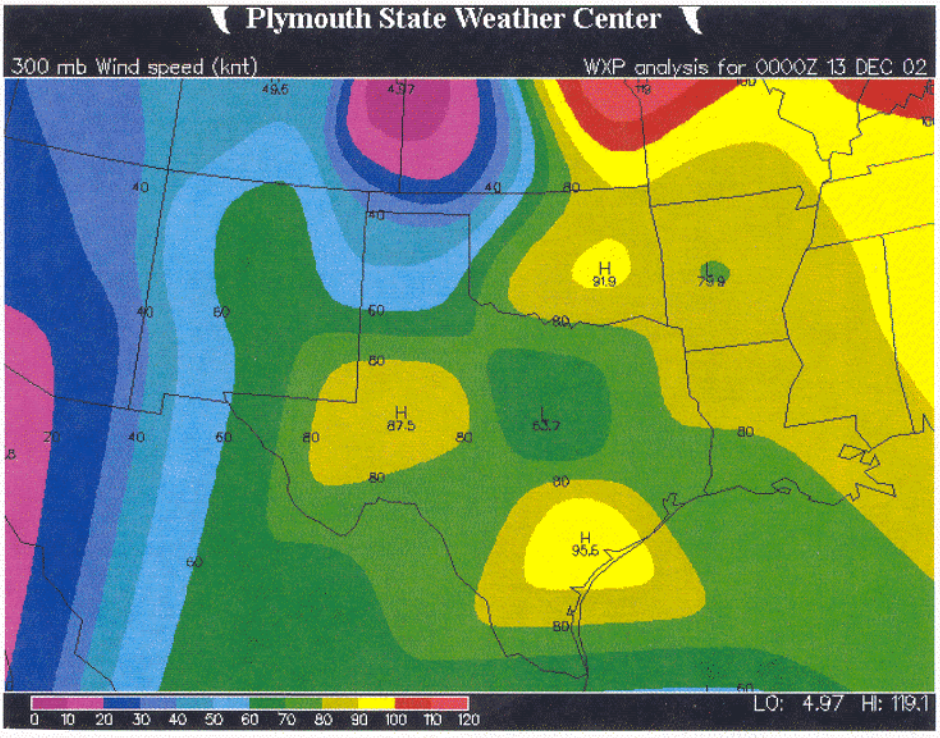


Fig. 10. Wind observation from 0000 UTC 13 December 2002 from <vortex.Plymouth.edu> (a) 300 hPa, (b) 200 hPa, and (c) 150 hPa (Continued next page).

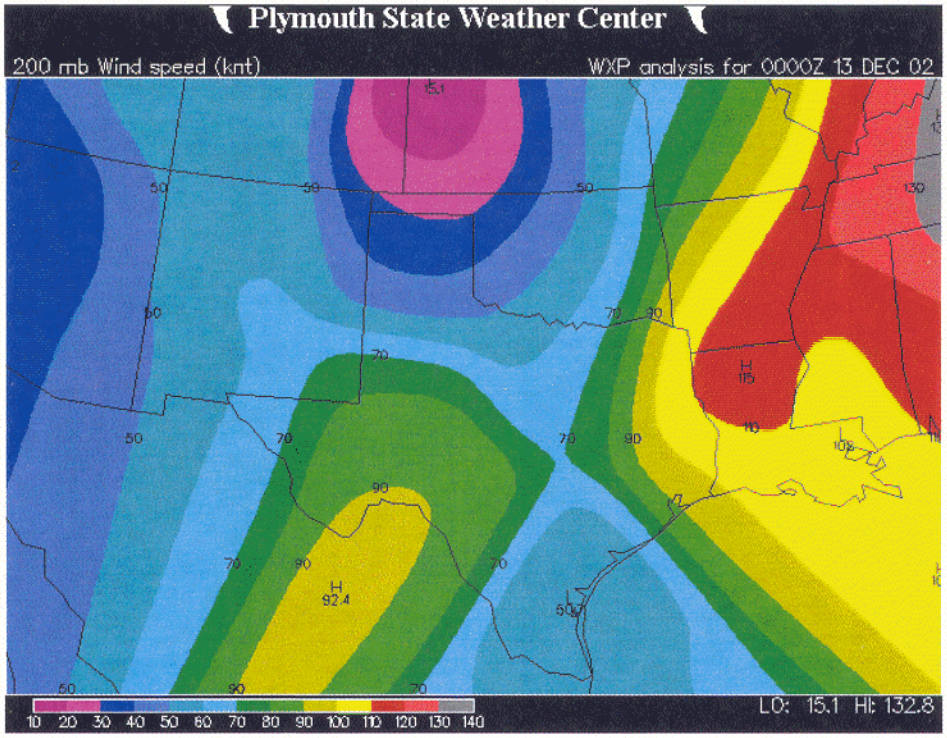


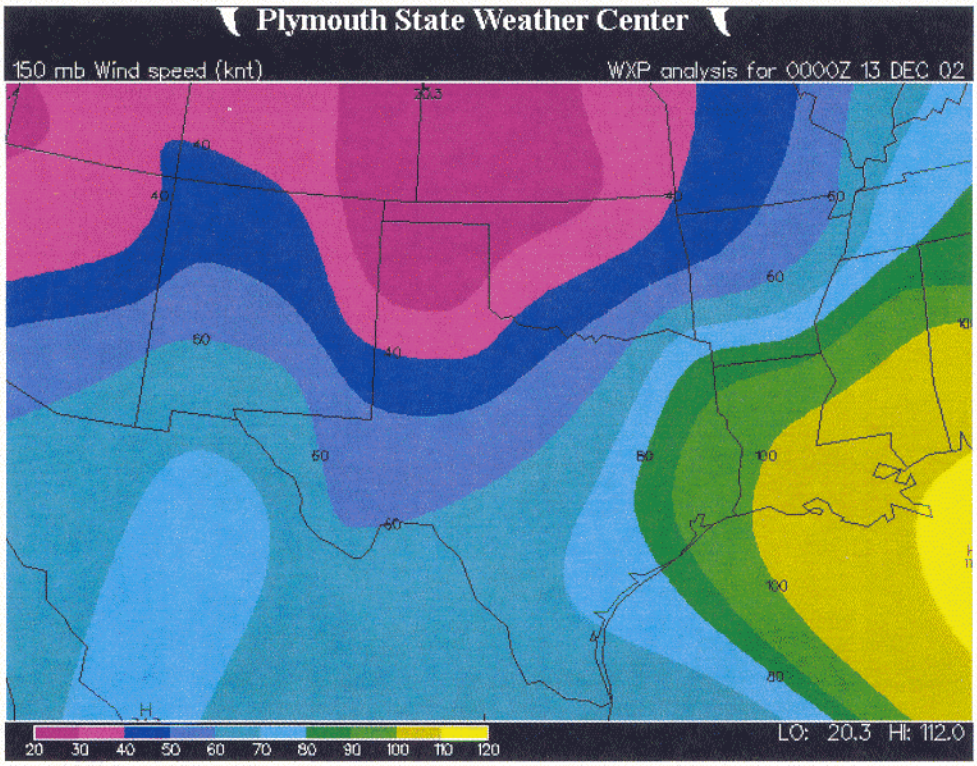


Fig. 10 (Cont'd). Wind observation from 0000 UTC 13 December 2002 from <vortex.Plymouth.edu> (a) 300 hPa, (b) 200 hPa, and (c) 150 hPa.

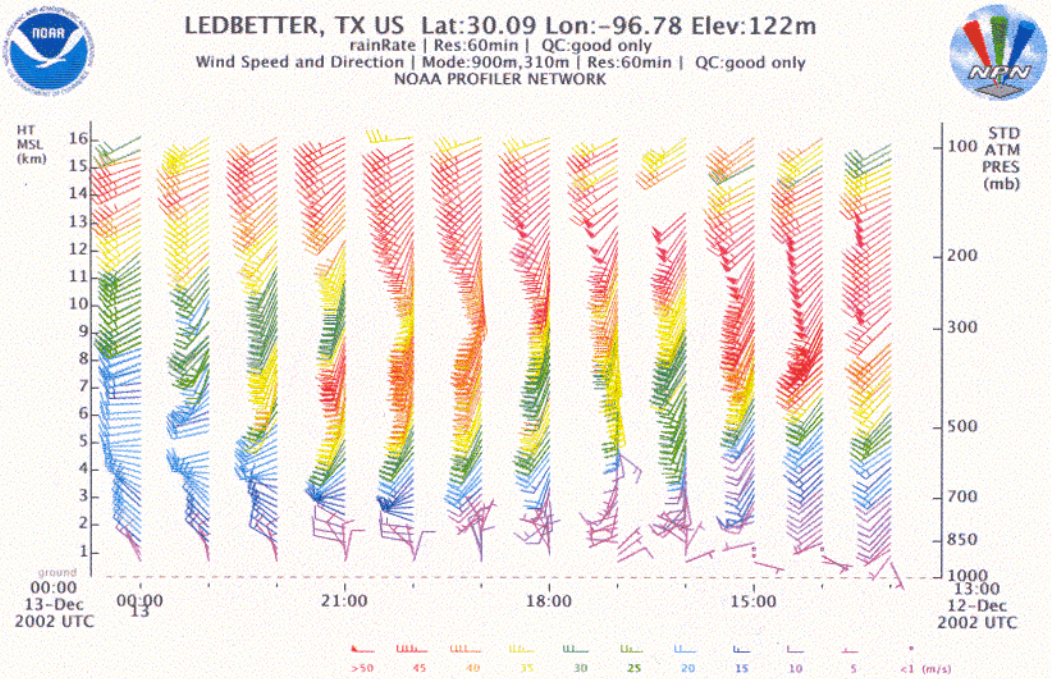


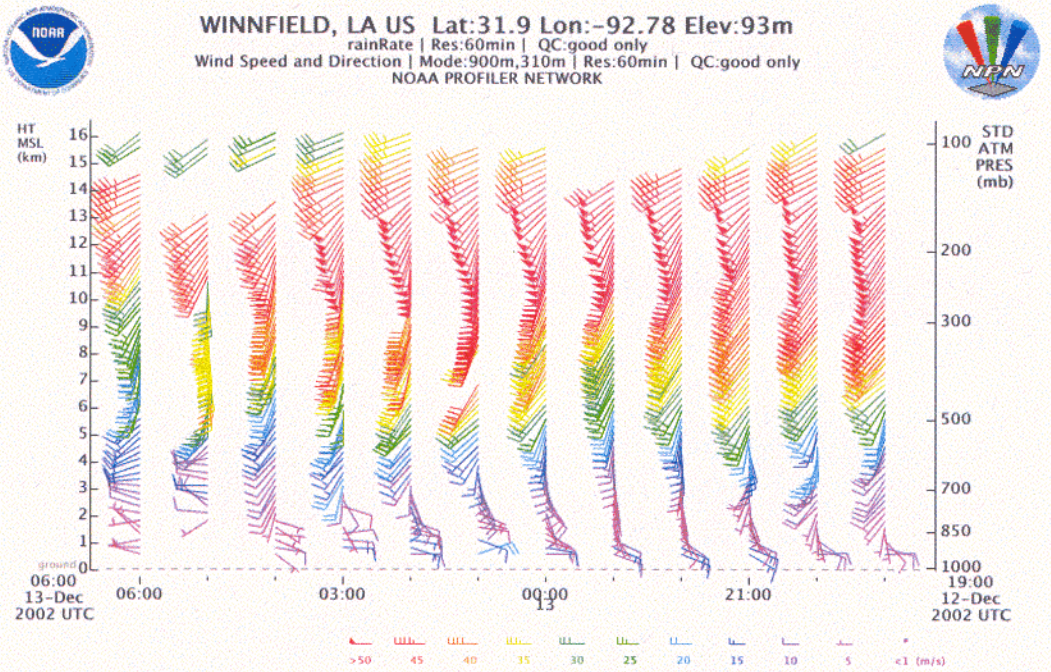


Fig. 11. Wind profilers from 1300 UTC 12 December 2002 to 0000 UTC 13 December 2002 (a) at Ledbetter, Texas, and from 1900 UTC 12 December 2002 to 0600 UTC 13 December 2002 (b) at Winnfield, Louisiana.

Fig. 12. 2 km NHMASS no latent model 2215 UTC 12 December 2002 surface winds (kts) and mean sea-level pressure (mb).

## 4. CONCLUSIONS

The modeled stratospheric gravity waves in this case allow for the redistribution of momentum aloft around and above the blocking convection. Also, the large amounts of vertical wind shear, seen throughout the troposphere and lower stratosphere in the observed wind profilers, raobs, and the modeled atmosphere, are consistent with the vertical momentum being mixed into the lower stratosphere. Verification of these stratospheric gravity waves is currently being pursued using AMSU data, similar to the study by Wu (2004), and it is our hope to have the data available by the conference.

## 5. ACKNOWLEDGEMENTS

The first author wishes to thank Dr. Kenneth T. Waight for his help using and fixing problems with the NHMASS model and Michael T. Kiefer for his valuable input and discussion. This research was supported U.S. Air Force contract No. FA8718-04-C-0011.

## 6. REFERENCES

Clark, T. L., W. D. Hall, R. M. Kerr, D. Middleton, L. Radke, F. M. Ralph, P. J. Neiman, and D. Levinson, 2000: Origins of aircraft-damaging clear-air turbulence during the 9

December 1992 Colorado downslope windstorm: Numerical simulations and comparison with observations. *J. Atmos. Sci.*, **57**, 1105-1131.

Kiefer, M. T., 2005: The impact of superimposed synoptic to meso-gamma scale motions on extreme snowfall over western Maryland and northeastern West Virginia during the 2003 Presidents' Day winter storm. MS thesis, Department of Marine, Earth, and Atmospheric Science, North Carolina State University, 204 pp.

Lane, T. P., R. D. Sharman, T. L. Clark, and H.-M. Hsu, 2003: An investigation of turbulence generation mechanisms above deep convection. *J. Atmos. Sci.*, **60**, 1297-1321.

Rauber, R. M., M. Yang, M. K. Ramamurthy, and B. F. Jewett, 2001: Origin, evolution, and finescale structure of the St. Valentine's Day mesoscale gravity wave observed during STORM-FEST. Part I: origin and evolution. *Mon. Wea. Rev.*, **129**, 198-217.

Uccellini, L. W., and S. E. Koch, 1987: The synoptic setting and possible energy sourcesfor mesoscale wave disturbances. *Mon. Wea. Rev.*, **115**, 721-729.

Wu, D. L., and F. Zhang, 2004: A study of mesoscale gravity waves over the North Atlantic with satellite observations and a mesoscale model. *J. Geophys. Res.*, **109**, D22104.

Zhang, F., S. E. Koch, and M. L. Kaplan, 2003: Numerical simulations of a large-amplitude mesoscale gravity wave event. *Meteorol. Atmos. Phys.,* **84**, 199-216.

_____, 2004: Generation of mesoscale gravity waves in the upper-tropospheric jet-front systems. *J. Atmos. Sci.*, **61**, 440-457.

## Appendix D

# THE IMPACT OF SUPERIMPOSED LOW-LEVEL JETS DURING THE 2003 PRESIDENTS' DAY WINTER STORM

Michael T. Kiefer1, Michael L. Kaplan2, and Yuh-Lang Lin1
1North Carolina State University, Raleigh, North Carolina
[2]Desert Research Institute, Reno, Nevada

## 1. INTRODUCTION

During 15-18 February 2003, almost exactly 24 years after the infamous 1979 Presidents' Day event (18-19 February 1979, hereafter PD79), another winter storm of great intensity impacted the eastern third of the United States. Snowfall amounts of greater than 50 cm were common from Virginia northward to extreme southern New England, with numerous reports of event snowfall exceeding 100 cm over northeastern West Virginia and western Maryland (hereafter, the region of interest). While both events produced excessive amounts of snow and ice over the Metropolitan areas of the mid-Atlantic and northeastern U.S. (See Bosart 1981 for snowfall analysis during the former), the extreme snowfall observed during the 2003 Presidents' Day event (PD03) occurred despite the absence of a rapidly deepening coastal cyclone, a feature noted to be critical to the heavy snowfall reported during PD79 (Uccellini et al. 1985). Within this paper, the development and subsequent interaction of two low-level jets (termed the continental and maritime, see Figure 1 for proposed conceptual model during height of event) will be considered in detail in a numerical modeling analysis of the forcing for heavy snowfall over the mid-Atlantic U.S. and in particular the region of interest.

The primary motivation of this study has been improving the understanding of winter storm dynamics, and subsequently our ability to adequately predict heavy snowfall in such events as PD03. While operational model forecasts of PD03 were generally reasonable, the extreme snowfall amounts observed within the region of interest were poorly forecast. One component present in PD03, the continental low-level jet directed from the Gulf of Mexico toward the region of interest in the 600-800 hPa layer (see Fig. 1), is absent in prior studies of winter storm precipitation. A preliminary assessment of other cases reveals a number of events (e.g. 19-20 January 1978, 4-5 December 2002, etc.) in which similar jets developed, yet little research has been done to understand the implications and origins of such features. It will be shown that the continental and maritime low-level jets just discussed contributed significantly to snowfall over the region of interest primarily through moisture transport and frontogenesis. Dynamical analysis in this study is performed primarily through the use of a mesoscale numerical model, the Non-Hydrostatic Mesoscale Atmospheric Simulation System (NHMASS) version 6.3 (Kaplan et al. 2005).

An observational summary of this event is presented in Section 2. Section 3 provides a brief description of the NHMASS model, while Section 4 describes principal results of this study, and Section 5 presents concluding remarks.

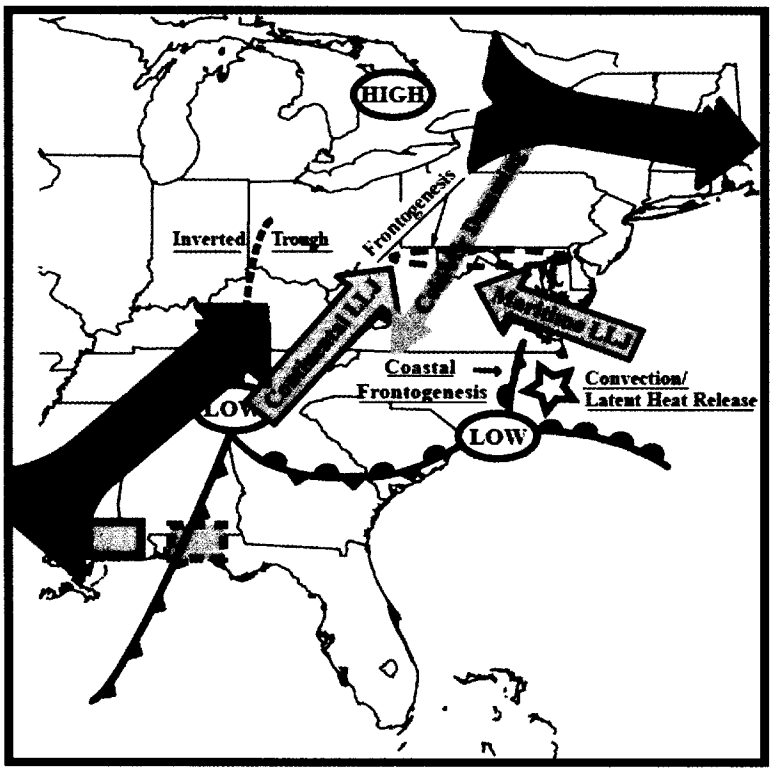


Fig. 1. A conceptual model of Presidents' Day 2003 winter storm. Regions over which moisture calculations in Table 1 are indicated by a solid box [16/0000 and 16/0600 calculations] and dashed box [16/1200 calculation] along the Gulf coast.

## 2. OBSERVATIONAL SUMMARY

The Presidents' Day 2003 winter storm can essentially be traced back in time to the merging of two upper-tropospheric jet streaks over the eastern United States. As early as 1200 UTC 14 February 2003, one can observe two airstreams: the subtropical jet (STJ) directed from the northeast Pacific Ocean across northern Mexico and toward the mid-Atlantic United States, and the polar jet (PJ) oriented from the Canadian plains across the Great Lakes region toward the mid-Atlantic U.S. (c.f. Figs. 1 and 2). A weak trough propagating along the poleward side of a western U.S. mid-level ridge (not shown) contributed to the formation of a lee cyclone seen at 850mb at 1200 UTC 14 February 2003 (Fig. 2b1), which subsequently was located on the Missouri/Kansas border at 1200 UTC 15 February 2003 (not shown), and over western Tennessee by 1200 UTC 16 February 2003 (Fig. 2b2).

At the surface, a low is noted at 1200 UTC 14 February 2003 over southwestern Kansas (Fig. 2c1) with a developing frontal boundary to the east. By 1200 UTC 16 February 2003 (Fig. 2c2), the surface low had moved toward central Alabama, and an anticyclone over northern Saskatchewan had moved to a position near Montreal, Quebec (CYUL) with strong cold-air damming (CAD) present in the lee of the Appalachians, as evidenced by the southward bulge of the isobars. Also seen at the time is a pair of inverted troughs on either side of the CAD region, the eastern one associated with coastal

frontogenesis taking place and the western inverted trough consistent with previous studies of CAD events (Bell and Bosart 1988). A weak cyclone had also formed offshore of the North Carolina coast in the vicinity of the coastal front trough.

The kinked stationary frontal boundary over Tennessee apparent in Figure 2c2 was associated with a tongue of warm air transported northward by the continental low-level jet above 850 hPa (Fig. 3a). Elevated convection was present over northern Kentucky, southern Indiana, and southern Ohio just north of the surface warm air tongue. Also seen at that time is a band of light to moderate precipitation from northern West Virginia to southern New Jersey (Fig. 4). This band is parallel to an intensifying frontal zone aloft in the 600-800 hPa layer (not shown) indicated in Fig. 1 by the dashed ellipse across northern West Virginia and Virginia. It was within this broader band that the intense snowfall was reported across northeastern West Virginia and western Maryland 6-18 hours later.

Figure 5 depicts the observed trends of 24 hour accumulated precipitation between 1200 UTC 14 February 2003 and 1200 UTC 17 February 2003, indicating a dramatic shift of precipitation following 1200 UTC 16 February 2003 from the Tennessee River valley toward the mid-Atlantic U.S. What must be considered is what mechanism(s) are largely responsible for the large precipitation amounts evident in Fig. 5d across the mid-Atlantic U.S. and especially over the region of interest.

## 3. MODEL DESCRIPTION AND VALIDATION

### 3.1. Model Description

A mesoscale numerical model is used in this study to diagnose the multi-scale processes contributing to the excessive precipitation amounts reported in western Maryland. While observational data, for example NCEP/NCAR Reanalysis (Kalnay et al. 1996) and the North American Regional Reanalysis (NARR) (Mesinger 2004) data sets, wind profilers, and 2km NOWRAD Doppler radar data were analyzed when available, the resolution and/or temporal coverage of these sources of data made the use of a mesoscale numerical model essential for this study. The model chosen for this study is the NHMASS version 6.3 (Kaplan et al. 2005). One-way nesting was performed from 18 km horizontal resolution to 222 m resolution, with a separate 36km simulation performed for trajectories and validation of large scale patterns with NARR data. The 18 km and 36 km resolution runs were initialized with NCEP/NCAR Reanalysis data. For a complete summary of simulations performed and physics parametrization options utilized, see Kiefer (2005).

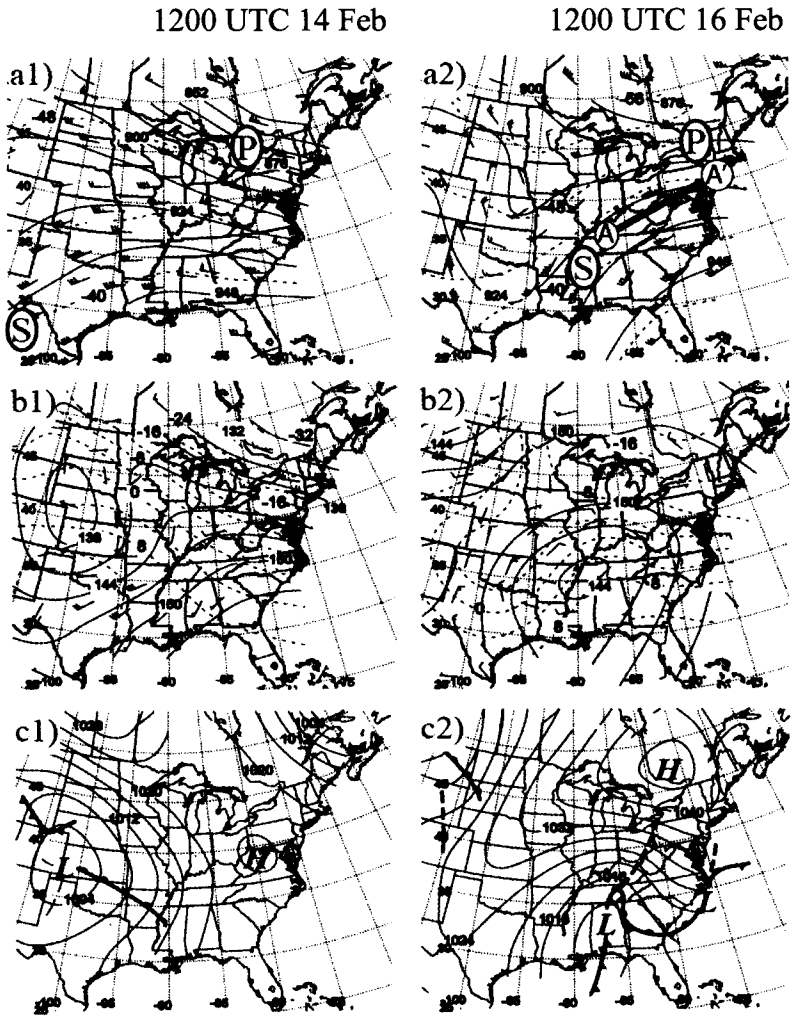


Fig. 2. NCEP/NCAR Reanalysis plots of a) 300 hPa, b) 850 hPa heights (dm), temperature (°C), and winds ($ms^{-1}$), and c) Sea-level pressure (hPa) and surface frontal analysis, valid 1200 UTC 14 Feb 2003 (a1,b1,c1) and 1200 UTC 16 Feb 2003 (a2,b2,c2). Approximate positions of polar jet (P) and subtropical jet (S), determined from 300 hPa geostrophic wind maxima, noted in (a). Labels are omitted every other contour in all figures. Axis A-A' in (a2) for cross-section in Fig. 6.

a)

b)

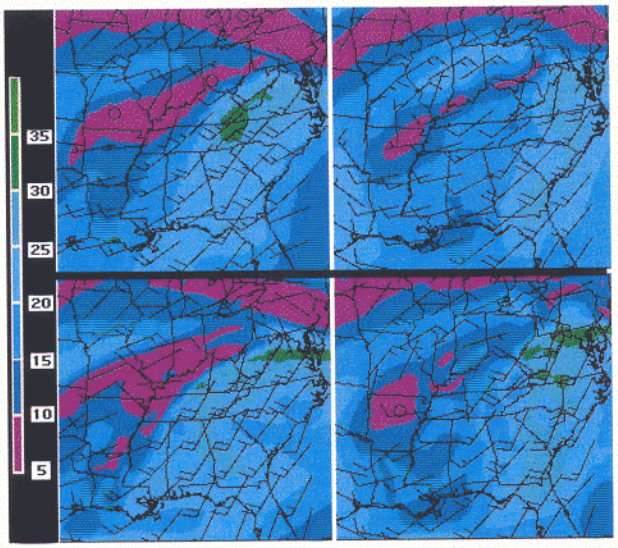


Fig. 3. 750 hPa heights [dm], isotachs [m/s, shaded], wind vectors [m/s] valid 0000 UTC [left two panels] and 1200 UTC [right two panels] 16 Feb 2003 for (a) NARR data and (b) 18 km NHMASS.

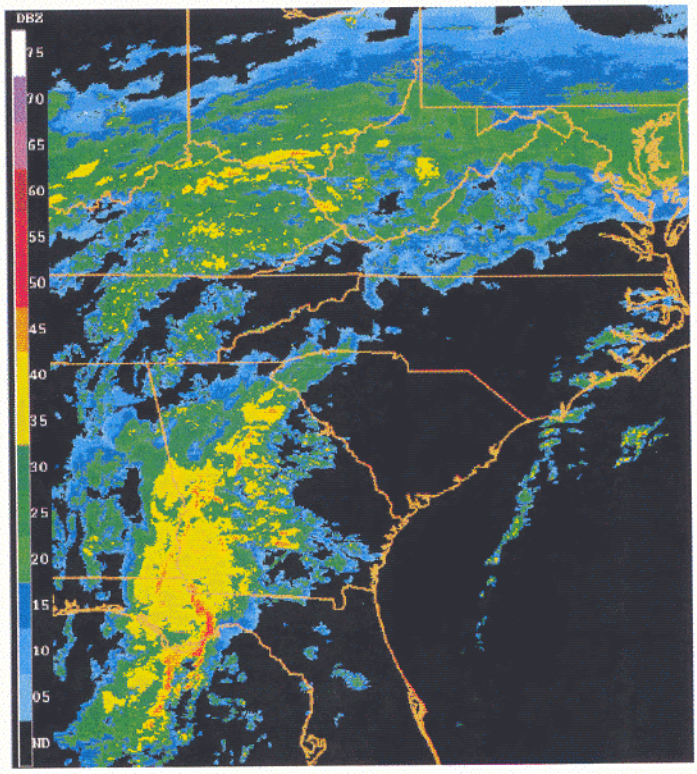


Fig. 4. NOWRAD 2-km base reflectivity valid 1200 UTC 16 Feb 2003.

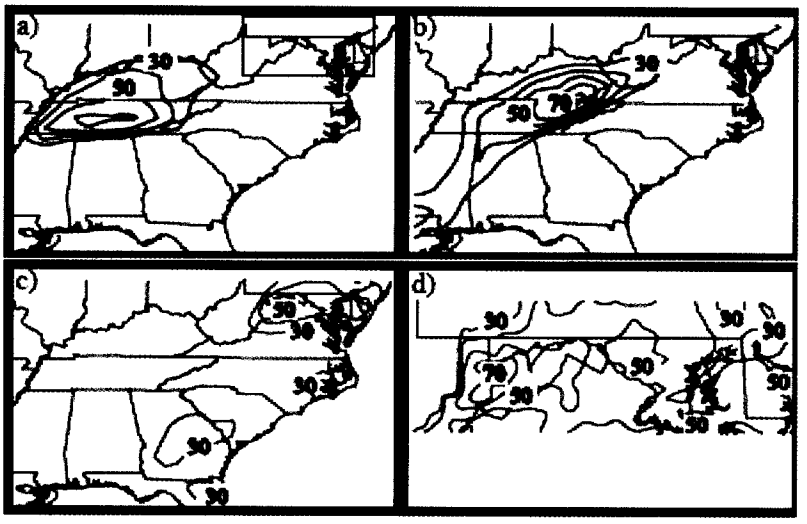


Fig. 5. 24 hour accumulated precipitation [mm, greater than 30 mm plotted, labeled every other contour] from CPC 1/8 degree rain-gauge analysis produced from objectively analyzed rain-gauge dataset (courtesy NCEP), valid a) 1200 UTC 15 Feb 2003, b) 1200 UTC 16 Feb 2003, c) and d) 1200 UTC 17 Feb 2003, with (d) inset image of (c). Inset region for (d) indicated in (a). Labels are omitted every other contour in all figures.

A number of sensitivity experiments were performed in order to isolate the impact of specific processes believed to be important in generating the excessive total precipitation observed across the region of interest, including a smoothed terrain simulation and a dry simulation. The former experiment will briefly be considered in this paper.

### 3.2. Model Validation

In order to lend credibility to the numerical modeling study of the dynamics leading to the generation of extreme amounts of snowfall, validation of the model synoptic fields and verification of the model precipitation was performed. Simulated 300 hPa and 850 hPa isobaric analyses and surface analyses, all from a coarse (36 km NHMASS) simulation valid 1200 UTC 16 February 2003, were compared to the previously discussed NARR datasets. At each of the levels considered, the simulation results compare favorably with the observed data (not shown).

## 4. MODEL RESULTS

### 4.1. LLJ Interaction – Moisture Transport

The juxtapositioning of the two low-level jets, i.e., maritime and continental, is the focus of this and the following section. The impact of these two low-level jet/frontal systems on the precipitation development over the region of interest will now be considered. Both jets act to transport moisture toward the region of interest, evidenced

by moisture transport calculations performed with both NHMASS and NARR data for the continental jet ( $\rho\overline{q}\overline{V}$ ; see Uccellini et al.. 1984 for methodology) in Table 1. The values are comparable to that diagnosed for the PD79 low-level jet and for springtime low-level jets during convective scenarios (Uccellini et al. 1984). Additionally, the two jets transport air of greatly differing thermal characteristics into mutual proximity. The transport of warm air in the approximately 600-850 hPa layer over the dense cold air below 850 hPa associated with the maritime low-level jet will be considered in its implication for frontal lifting and closely-related frontogenesis.

### 4.2. LLJ Interaction - Frontal lifting / Frontogenesis

In order to begin this analysis of the impact of the superpositioning of the two jet/front systems, a southwest-northeast vertical cross-section of potential temperature and wind speed from the 6km NHMASS simulation (Fig. 6) proves invaluable. Immediately noticeable are dual shear zones and frontal inversions present over the northern Mid-Atlantic region, including western Maryland. Also apparent is the slope of isentropes north and east of the highest terrain, a direct result of the strong anticyclone over southern Quebec, wherein the depth of the cold air increases as one approaches the anticyclone (see Fig. 2c2). One result of the superpositioning of the two jets and their representative airmasses was the process wherein the generally 20-30 m $s^{-1}$ continental jet progressed north and east over the dense cold-air damming airmass evident in Figure 6. The impact of the continental jet directed up the strongly sloped isentropes is apparent in a 6 km NHMASS simulated composite reflectivity image overlaid with isobars on the 300 K isentropic surface at 0000 UTC 17 February 2003 (Figure 7). One notices that the greatest composite reflectivity values are poleward of a frontal zone generally located between 690-730 hPa just south of the Pennsylvania-Maryland border. Also apparent is a largely meridional pressure gradient located just southwest of the 45 dBz composite reflectivity maximum. Considering the direction of the continental jet from the southwest (see Fig. 3), and the orientation of the continental jet approximately normal to the strongly sloped isentropic surfaces in the vertical cross-section in Figure 6, it appears that the vigorous frontal lifting of the continental jet is playing a role in producing the zonal band of heavy precipitation in the Mid-Atlantic U.S.

Observing the layer between approximately 750 and 850 hPa in Figure 6, it is apparent that the two low-level jets, the continental and maritime, are directed in a confluent manner in that layer, a critical observation in that such an interaction has great implications for frontogenesis. It should be noted that the following treatment of frontogenesis deviates from the recent work of Novak et al. (2004) in that this study considers a fairly shallow layer of frontogenesis produced through low-level jet interaction, whereas the study of Novak et al. (2004) looked at heavy snow banding resulting from (1) deformation zones northwest of surface cyclones and (2) deep layers of frontogenesis owing to mid- to upper-level confluent flow. Comparing the band of snowfall evident in Fig. 4 to the mid- to upper-level confluent flow across the eastern U.S. in Fig. 2a2, the broad band from southern Ohio to southern New Jersey appears consistent with Novak et al.'s non-banded case (see their Fig. 15b). What is being

considered in this section is the impact of the two low-level jets, the continental and maritime, on frontogenesis across the mid-Atlantic U.S., largely below the level considered in Novak et al. To assess the various contributions to frontogenesis over the mid-Atlantic U.S., this study has utilized a 2-dimensional form of the Miller (1948) frontogenesis equation in height coordinates, defined as:

$$F=\frac{1}{|\nabla_\sigma\theta|}\left\{\begin{array}{l}\frac{\partial\theta}{\partial x}\left[-\left(\frac{\partial u}{\partial x}\frac{\partial\theta}{\partial x}\right)_1-\left(\frac{\partial v}{\partial x}\frac{\partial\theta}{\partial y}\right)_2-\left(\frac{\partial w}{\partial x}\frac{\partial\theta}{\partial z}\right)_3\right]\\ +\frac{\partial\theta}{\partial y}\left[-\left(\frac{\partial u}{\partial y}\frac{\partial\theta}{\partial x}\right)_4-\left(\frac{\partial v}{\partial y}\frac{\partial\theta}{\partial y}\right)_5-\left(\frac{\partial w}{\partial y}\frac{\partial\theta}{\partial z}\right)_6\right]\\ +\frac{1}{C_p}\left(\frac{P_o}{P}\right)^k\left[\left(\frac{\partial\theta}{\partial x}\frac{\partial}{\partial x}\left(\frac{\partial Q}{\partial t}\right)\right)_7+\left(\frac{\partial\theta}{\partial y}\frac{\partial}{\partial y}\left(\frac{\partial Q}{\partial t}\right)\right)_8\right]\end{array}\right\}. \quad (1)$$

Terms 1 and 5 are confluent deformation terms, while terms 2 and 4 represent shearing deformation. Terms 3 and 6 represent tilting effects in the x- and y-directions, respectively, while terms 7 and 8 are diabatic heating terms. Figures 8-9 represent (a) confluent deformation, (b) tilting effects, and (c) diabatic heating effects for 2000 UTC 16 February 2003 (Figure 8) and 2100 UTC 16 February 2003 (Figure 9) during the period of heaviest precipitation over the region of interest.

An analysis of the frontogenesis equation reveals that the result of two streams of air parcels approaching the region of interest from directions varying approximately 30-40 degrees (see wind vectors in Fig. 6 near center of cross-section in 700-800 hPa layer) is a sustained stripe of confluent deformation from western Maryland into northeastern West Virginia (Figs. 8-9a), along the Alleghany mountain range (not shown). Results from a smoothed terrain simulation indicate that the frontogenetical band ceases to exist when the terrain is strongly smoothed (not shown). The other band of confluent deformation, albeit weaker, appears to have been produced through speed convergence, as low-level parcels approaching the mid-Atlantic from the south and southwest, decelerated significantly (see Fig. 3).

In light of the previous discussion on frontal lift, horizontal frontogenesis should imply a greater slope of isentropic surfaces, stronger vertical velocities and, in the presence of a saturated atmosphere, greater quantities of precipitation. Given the fact that the greatest precipitation rates are on the poleward side of the frontal zone, the impact of secondary circulations due to horizontal deformation, opposing frontogenesis and thereby producing descending motion on the poleward side (Keyser and Shapiro 1986), appears negligible. The presence of the highest simulated total precipitation (e.g. Figure 7) east of the meridionally oriented 800 hPa baroclinic zone (with predominately southwesterly 600-800hPa flow) and north of the zonally oriented front (with generally south to southeast low- to mid-level flow), appears to implicate confluent deformation in the production of heavy snowfall over the region of interest.

The tilting and diabatic terms were noted to be important in repositioning the frontal zones, while the primary source of frontogenesis, establishing and maintaining heavy precipitation over the region of interest, was horizontal deformation (primarily confluent deformation). It is this mechanism which produces narrow regions of strongly

sloping isentropes, thereby generating a band of strong vertical velocity and (in a saturated atmosphere) a band of heavy precipitation, with the diabatic heating (and tilting term to a lesser degree) then gaining importance and acting to modulate the fronts locally. The tilting term, while noted here to be important especially in the presence of complex terrain, is likely of greater importance further up into the middle troposphere, as tilting effects there are expected to dominate over horizontal deformation as temperature advections are weaker and vertical motions stronger (Miller 1948). Quite apparent is the tenuous relationship between the low-level jets, their frontal counterparts, and the positioning of mesoscale bands of precipitation across the region of interest, wherein slight variations in the intensity and position of the first two phenomena can have an enormous impact on the intensity and positioning of the heaviest snowfall.

### 4.3. LLJ Interaction - Additional Impacts

Before continuing further, a few additional significant impacts of the atmospheric structure described in Figure 1 will be discussed. First, an unbalanced subtropical jet exit region upstream of a mid-tropospheric ridge and north of a surface frontal boundary is a region of the atmosphere known to be conducive to the generation of inertia-gravity wave activity (Koch and Dorian 1988, among others). Indeed, such a synoptic setup did exist during PD03, and NHMASS simulations do indicate corresponding wave activity, although a limited observational analysis has been performed to verify this. Additionally, the thermal structure and wind-shear profiles resulting from the superpositioning of the two low-level jets produces a lower-atmosphere conducive for low-level wave-ducting (Lindzen and Tung 1976). Finally, vertically-propagating inertia-gravity waves amplifying and breaking in the upper-troposphere and lower-stratosphere are one known source of lower-stratospheric turbulence (Clark et al. 2000; Lane et al. 2003). Currently, work is being performed in order to improve prediction of lower-stratospheric turbulence produced, among other sources, by breaking inertia-gravity waves.

| | | | | |
|---|---|---|---|---|
| 16/0000 | 200 | 16.02 | 6.13 | 95.18 |
| | (200) | (17.39) | (6.63) | (112.30) |
| 16/0600 | 200 | 20.36 | 7.47 | 149.21 |
| 16/1200 | 210 | 16.77 | 8.94 | 145.82 |
| | (210) | (15.07) | (8.18) | (120.11) |

Table 1 Moisture Transport along axis of low-level jet averaged over 750 to 800 hPa layer for 18 km NHMASS simulation and NARR data (latter in parenthesis). Included are mean wind direction (WD, deg), wind speed (WS, $ms^{-1}$), and mixing ratio (q, $gkg^{-1}$). See Fig. 1 for area over which calculation was performed. See text for discussion.

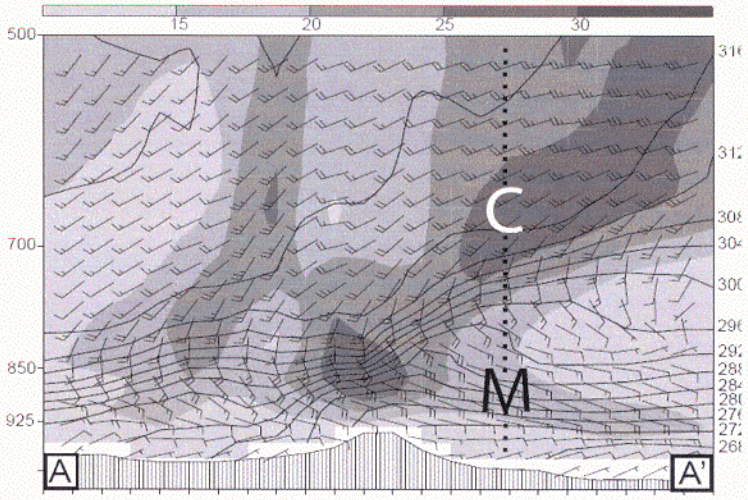


Fig. 6. 6km NHMASS vertical cross section of equivalent potential temperature [solid, K], total wind speed [shaded greater than 10 $ms^{-1}$] and total wind vectors [$ms^{-1}$], valid 0000 UTC 17 Feb 2003. Dashed vertical represents the location of western Maryland. Cross -section axis A-A' shown in Fig. 2a2. Labels "C" and "M" denote approximate positions of the continental and marine low-level jets, respectively, over western Maryland.

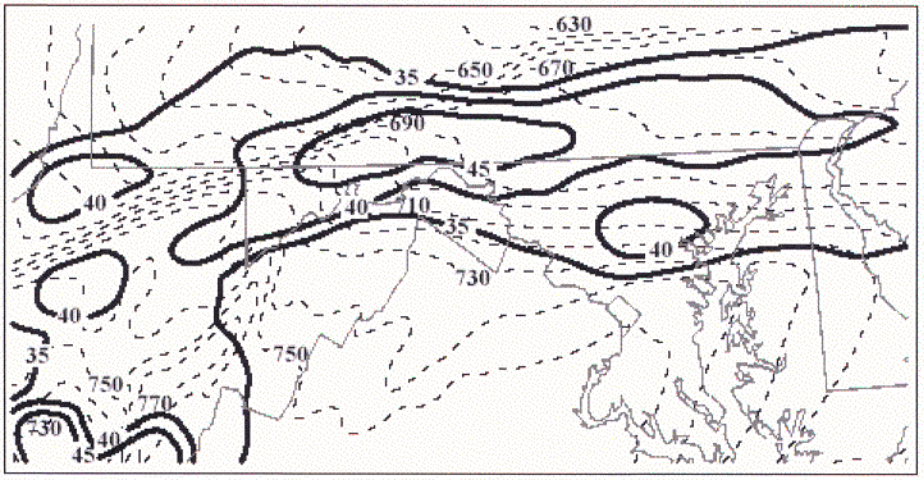


Fig. 7. 6km NHMASS Model Composite Reflectivity [solid, every 5 dBz, 35 dBz and greater] and pressure on the 300 K isentropic surface [hPa, every 10 hPa, alternate contours labeled] ending 0000 UTC 17 Feb 2003.

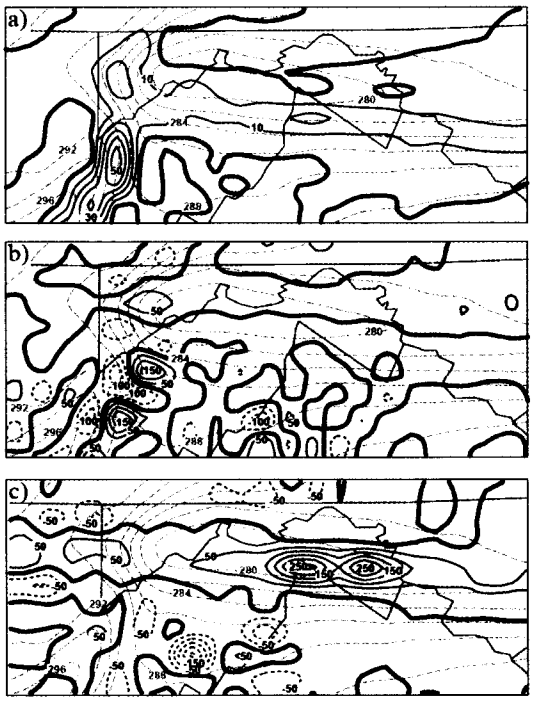


Fig. 8. 6 km NHMASS 800 hPa potential temperature (K, dashed gray lines) and frontogenetical forcing due to a) Confluent deformation (x $10^{-8}$), b) tilting effects (x $10^{-8}$), and c) diabatic heating (x $10^{-4}$) [K/ms, solid-frontogenetical forcing, dashed-frontolytical forcing] all valid 2000 UTC 16 Feb 2003

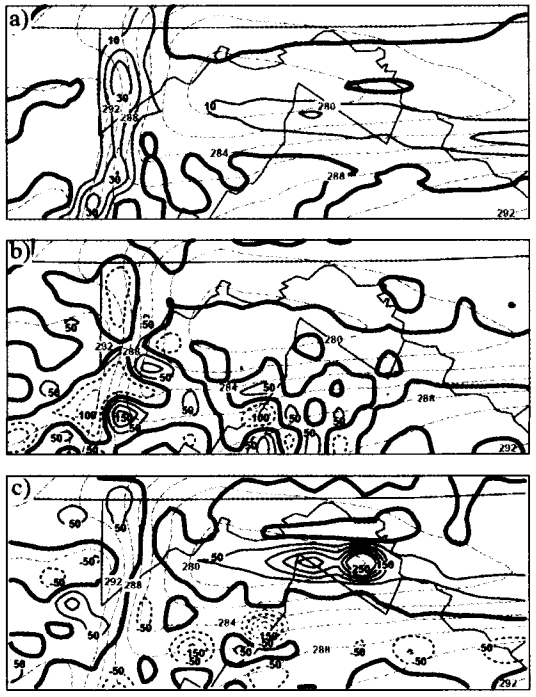


Fig. 9. As in Fig. 8, except valid 2100 UTC 16 Feb 2003.

## 5. SUMMARY AND CONCLUSIONS

This paper considered the impact of interaction of two jet/front systems on frontogenesis and heavy precipitation. It was shown that velocity convergence within the continental jet and confluence between the continental and maritime jets produced two bands of confluent deformation across the region of interest, one aligned with the primary terrain ridge in northeastern West Virginia and the second oriented zonally from near the first band to the Maryland shore. The positioning of a component of the continental jet normal to the two steepening frontal bands contributed to strong lift over the region of interest.

The juxtapositioning of the two low-level jet/front systems impacted not only the primary forcing for heavy precipitation over the region of interest, namely frontogenesis/warm-air advection and upper-level divergence, but also the secondary finer-scale mechanisms (such as terrain effects) that produced locally enhanced snowfall rates in the vicinity of complex terrain. These latter impacts will be considered in a future paper. Further implications of the synoptic and mesoscale atmospheric structure described in this paper were noted, including inertia-gravity wave generation and production of lower-stratospheric turbulence.

The critical point of this study is that the knowledge of the larger scale dynamic and thermodynamic structure of the atmosphere affords one the additional knowledge of the potential for fine-scale mechanisms that may lead to locally higher snowfall totals. Of note is the fact that the operational ETA model 24 hour forecast for 24 hour precipitation ending 1200 UTC 17 February 2003, encompassing the heaviest period of snowfall over the mid-Atlantic U.S., featured a precipitation maximum shifted significantly southeast of the region of interest. A forecasted continental jet weaker than that which was observed, and the coarse nature of the terrain dataset utilized by the ETA model raise questions as to how best an operational forecaster can interpret a model forecast, based on the dynamics considered within this study, and issue more accurate forecasts of snowfall in areas of complex terrain during similar winter storm scenarios. Much future work is required though before a new conceptual model can be utilized by the operational forecasting community. Additional winter storm case studies, particularly those focused in areas of small-scale complex terrain are required to evaluate the commonality of superimposed low-level jets during winter storms. With these additional efforts, the goal of improving operational forecasting of extreme snowfall during winter storms, and thereby improving the well-being of the public-at-large during such events, may be accomplished.

This study began with a number of reports of snowfall totals exceeding 100 cm across western Maryland and northeastern West Virginia during the 2003 Presidents' Day winter storm. It is believed that an assessment of the development and modification of low-level jet/front systems similar to the continental and maritime in this study will improve the timely and accurate prediction of such extreme snowfall, through improved understanding of the anticipated multi-scale processes capable of generating locally enhanced precipitation. While much more work is necessary to achieve the goal of improving operational forecasting of extreme snowfall in complex terrain, the author considers this endeavor as an important intermediate step between the previous studies on winter storm precipitation contributing to the conceptual model presented in Kocin and

Uccellini (1990) and ongoing work toward a new conceptual model of winter storm precipitation incorporating the continental jet discussed here (of which Figure 1 is a prototype).

## 6. ACKNOWLEDGEMENTS

The first author wishes to thank Dr. Gary Lackmann for helpful suggestions on improving the Masters thesis of which this paper is based on, and Dr. Kenneth Waight for his assistance with NHMASS. This research was supported initially by NASA grants NAG1-03013 and NAG1-0343 and later by U.S. Air Force contract No. FA8718-04-C-0011.

## 7. REFERENCES

Bell, G.D., and L.F. Bosart, 1988: Appalachian cold air damming. Mon. Wea. Rev., 116, 137-161

Bosart, L.F., 1981: The Presidents' Day snowstorm of 18-19 February 1979: A subsynoptic-scale event. Mon. Wea. Rev., 109, 1542-1566.

Clark, T. L., W. D. Hall, R. M. Kerr, D. Middleton, L. Radke, F. M. Ralph, P. J. Neiman, and D. Levinson, 2000: Origins of aircraft-damaging clear-air turbulence during the 9 December 1992 Colorado downslope windstorm: Numerical simulations and comparison with observations. J. Atmos. Sci., 57, 1105-1131.

Kalnay, E., and co-authors, 1996: The NMC/NCAR 40-year reanalysis project. Bull. Amer. Meteor. Soc., 77, No. 3, 437-471.

Kaplan, M. L., C. Huang, Y.-L. Lin and J. J. Charney, 2005: A multi-scale paradigm for rapid vertical airmass coupling resulting in high fire weather potential. Part II: Numerical simulations. Submitted, Mon. Wea. Rev.

Keyser, D. A., and M. A. Shapiro, 1986: A review of the structure and dynamics of upper-level frontal zones. Mon. Wea. Rev., 114, 452-499.

Kiefer, M. T., 2005: The impact of superimposed synoptic to meso-gamma scale motions on extreme snowfall over western Maryland and northeastern West Virginia during the 2003 Presidents' Day winter storm. MS thesis, Department of Marine, Earth, and Atmospheric Science, North Carolina State University, 204 pp.

Koch, S. E., and P. B. Dorian, 1988: A mesoscale gravity wave event observed during CCOPE. Part III: Wave environment and probable source mechanisms. Mon. Wea. Rev., 116, 2570-2592.

Kocin, P. J. and L. W. Uccellini, 1990: Snowstorms along the northeastern coast of the United States: 1955 to 1985. Amer. Met. Soc.

Lane, T. P., R. D. Sharman, T. L. Clark, and H.-M. Hsu, 2003: An investigation of turbulence generation mechanisms above deep convection. J. Atmos. Sci., 60, 1297-1321.

Lindzen, R. S., and K. K. Tung, 1976: Banded convective activity and ducted gravity waves. Mon. Wea. Rev., 104, 1602-1617.

Mesinger, F., and co-authors, 2004: North American Regional Reanalysis. Proc., Amer. Met. Soc. Annual Meeting, Seattle, WA, Amer. Met. Soc., CDROM, P1.1.

Miller, J. E., 1948: On the concept of frontogenesis. J. Meteor., 5, 169-171.

Novak, D. R., 2004: An observational study of cold season-banded precipitation in northeast U.S. cyclones. Wea. Forecasting, 19, 993-1010.

Uccellini, L. W., P. J. Kocin, R. A. Petersen, C. H. Wash, K. F. Brill, 1984: The Presidents' Day cyclone of 18-19 February 1979: Synoptic overview and analysis of the subtropical jet streak influencing the pre-cyclogenetic period. Mon. Wea. Rev., 112, 31-55.

_____, D. Keyser, K. F. Brill, and C. H. Wash, 1985: The Presidents' Day cyclone of 18-19 February 1979: Influence of upstream trough amplification and associated tropopause folding on rapid cyclogenesis. Mon. Wea. Rev., 113, 962-988.